

UNIVERSITY OF CALIFORNIA

Santa Barbara

Bio-inspired, subwavelength surface structures to control reflectivity, transmission, and  
scattering in the infrared

A dissertation submitted in partial satisfaction of the  
requirements for the degree Doctor of Philosophy  
in Chemical Engineering

by

Federico Lora Gonzalez

Committee in charge:

Professor Michael J. Gordon, Chair

Professor Daniel E. Morse

Professor Bradley F. Chmelka

Professor Matthew E. Helgeson

March 2015

The dissertation of Federico Lora Gonzalez is approved.

---

Professor Daniel E. Morse

---

Professor Bradley F. Chmelka

---

Professor Matthew E. Helgeson

---

Professor Michael J. Gordon, Committee Chair

January 2015

Bio-inspired, subwavelength surface structures to control reflectivity, transmission, and  
scattering in the infrared

Copyright © 2015

by

Federico Lora Gonzalez

## ACKNOWLEDGEMENTS

I want to acknowledge the entire UCSB community for providing such wonderful place to work and conduct research. In particular, I want to acknowledge my advisor, Professor Mike Gordon, whom I have had the pleasure of working with for the past four years. Mike's enthusiastic and passionate approach to research, science, and life has truly helped in my development and growth as a scientist. Mike is one of the most inspiring teachers and mentors I have ever had.

I would also like to specially acknowledge Professor Dan Morse, who has helped me tremendously with my work, from the very beginning of the project. We have had many, many hours of incredibly motivating discussions that helped guide my project to very interesting areas. I also want to thank Dan for his guidance, his motivation, and his generosity.

The Gordon group has grown and matured over the past four years. I want to thank the original members of the group, Louis Jones, Chris Carach, Travis Koh, and Isaac Riisness, for giving me their support and guidance in my first couple of years as a student. Working with Louis and Mike in the Summer of 2012 showed me what graduate school was all about; late nights, frustration, elation, and friendships. I am glad to have been part of such a tight-knit group of wonderful guys. I also want to thank my great friend and lab mate Alex Heilman, for helping me get through tough times and supporting me in all of my scientific and personal goals. I would not of been able to make it through these last four years without the help of my friends.

Finally, I want to thank the amazing faculty, the great team of staff at the MRL and the Nanofab, and all of the students who have helped me with my research and experiments. I have learned so many skills, experimental techniques, and lab tricks from the great scientific community here at UCSB that have truly helped me in reaching my goals.

*Vita of Federico Lora Gonzalez*  
January 2015

**EDUCATION**

- University of California** Santa Barbara, CA Jan. 2015  
Ph.D., Chemical Engineering; GPA: 3.72
- University of Maryland** College Park, MD May 2011  
B.S., Chemical Engineering; GPA: 3.733

**PUBLICATIONS**

- K. Mackie, F. Lora Gonzalez, A. Pebley and M. J. Gordon. "Microplasma-based synthesis of hierarchical semiconducting metal oxide and silicon micro-arrays," *In preparation*.
- F. Lora Gonzalez, D. E. Morse and M. J. Gordon. "Enhancing near-infrared light absorption in PtSi thin films for Schottky barrier IR detectors using moth-eye surface structures," *Submitted, Optics Letters*, January 2015.
- F. Lora Gonzalez, L. Chan, A. Berry, D. E. Morse and M. J. Gordon. "Simple colloidal lithography method to fabricate large-area moth-eye antireflective structures on Si, Ge, and GaAs for IR applications," *J. Vac. Sci. Technol. B* **32**, 051213 (2014).
- F. Lora Gonzalez and M. J. Gordon. "Bio-inspired, sub-wavelength surface structures for ultra-broadband, omni-directional anti-reflection in the mid and far IR," *Opt. Express* **22**, 12808-12816 (2014). \* \* Highlighted in *Virtual Journal for Biomedical Optics (VJBO)* **9** (2014).
- F. Lora Gonzalez, D. E. Morse and M. J. Gordon. "Importance of diffuse scattering phenomena in moth-eye arrays for broadband infrared applications," *Opt. Lett.* **39**, 13-16 (2014).
- D. Arana-Chavez, E. Toumayan, F. Lora, C. McCaslin, and R. A. Adomaitis. "Modeling the transport and reaction mechanisms of copper oxide CVD," *Chem. Vap. Deposition* **16**, 336-345 (2011).

**PRESENTATIONS**

- F. Lora Gonzalez, "Bio-inspired, quasi-ordered materials for IR-active coatings" UCSB Chemical Engineering First Year Symposium, Sept. 2012.

## ABSTRACT

Bio-inspired, subwavelength surface structures to control reflectivity, transmission, and scattering in the infrared

by

Federico Lora Gonzalez

Controlling the reflection of visible and infrared (IR) light at interfaces is extremely important to increase the power efficiency and performance of optics, electro-optical and (thermo)photovoltaic systems. The eye of the moth has evolved subwavelength protuberances that increase light transmission into the eye tissue and prevent reflection. The subwavelength protuberances effectively grade the refractive index from that of air ( $n=1$ ) to that of the tissue ( $n=1.4$ ), making the interface gradual, suppressing reflection. In theory, the moth-eye (ME) structures can be implemented with any material platform to achieve an antireflectance effect by scaling the pitch and size of protuberances for the wavelength range of interest.

In this work, a bio-inspired, scalable and substrate-independent surface modification protocol was developed to realize broadband antireflective structures based on the moth-eye principle. Quasi-ordered ME arrays were fabricated in IR relevant materials using a colloidal lithography method to achieve highly efficient, omnidirectional transmission of mid and far infrared (IR) radiation.

The effect of structure height and aspect ratio on transmittance and scattering is explored, with discussion on experimental techniques and effective medium theory (EMT). The highest aspect ratio structures (AR = 9.4) achieved peak single-side transmittance of 98%, with >85% transmission for  $\lambda = 7\text{-}30\ \mu\text{m}$ . A detailed photon balance constructed by transmission, forward scattering, specular reflection and diffuse reflection measurements to quantify optical losses due to near-field effects will be discussed. In addition, angle-dependent transmission measurements showed that moth-eye structures provide superior antireflective properties compared to unstructured interfaces over a wide angular range (0-60° incidence).

Finally, subwavelength ME structures are incorporated on a Si substrate to enhance the absorption of near infrared (NIR) light in PtSi films to increase Schottky-barrier detector efficiency. Absorbance enhancement of 70-200% in the  $\lambda=1\text{-}2.5\ \mu\text{m}$  range is demonstrated in crystalline PtSi films grown via electron beam evaporation of Pt and subsequent vacuum annealing. Low total reflectance (<10%) was measured in ME films, demonstrating the efficacy of the moth eye effect. Effective medium theory and transfer matrix calculations show that the large absorption enhancement at short wavelengths is partly due to light trapping, which increases the effective optical path length in PtSi. The demonstrated structures are promising candidates for efficient PtSi/p-Si Schottky barrier diode detectors in the NIR. Results further suggest a general method for relatively low-cost absorption enhancement of backside-illuminated detectors based on a wide variety of infrared absorptive materials.

The methods presented here to fabricate quasi-ordered ME structures provide a general platform for creating antireflective structures in many different materials, devices,



and bandwidths. Furthermore, understanding the relationship between protuberance shape, height, aspect ratio, etc. and performance (antireflection, scattering loss, etc.) can guide the design of antireflective surfaces for different applications (for example, in certain applications, large amounts of forward scattering is desired, e.g. photovoltaics).

## TABLE OF CONTENTS

<b>Chapter 1: Introduction</b> .....	1
1.1. <i>References</i> .....	8
<b>Chapter 2: Background</b> .....	11
2.1. <i>Light on planar surfaces</i> .....	13
2.1.1. <i>Maxwell's equations and complex refractive index</i> .....	13
2.1.2. <i>Infrared materials</i> .....	16
2.1.3. <i>Derivation of the Fresnel equations</i> .....	20
2.1.4. <i>Multiple interfaces: Interference and the transfer matrix                 formulation</i> .....	24
2.1.5. <i>Interference-based anti-reflective coatings</i> .....	27
2.1.6. <i>Anti-reflection limits in single and double-sided                 coated transparent substrates</i> .....	28
2.2. <i>Diffraction and light scattering</i> .....	30
2.3. <i>Effective medium theory</i> .....	34
2.3.1. <i>Effective medium approximations</i> .....	37
2.4. <i>References</i> .....	42
<b>Chapter 3: Experimental Methods and Instrument Development</b> .....	45
3.1. <i>Colloidal lithography</i> .....	46
3.1.1. <i>Synthesis of colloidal silica</i> .....	48
3.1.2. <i>Langmuir Blodgett trough and Wilhelmy plate apparatus</i> .....	52

3.1.3 Reactive ion etching.....	56
3.2. Optical characterization.....	58
3.2.1. Fourier transform infrared spectroscopy (FTIR).....	58
3.3. References.....	62

**Chapter 4: Importance of diffuse scattering phenomena in moth-eye arrays for**

<b>broadband IR applications.....</b>	<b>66</b>
4.1. Chapter summary.....	67
4.2. Introduction.....	67
4.3. Results and discussion.....	69
4.4. Conclusion.....	76
4.5. References.....	77

**Chapter 5: Bio-inspired, sub-wavelength surface structures for ultra-broadband,**

<b>omnidirectional anti-reflection in the mid and far IR.....</b>	<b>80</b>
5.1. Chapter summary.....	81
5.2. Introduction.....	81
5.3. Experimental methods and theoretical calculations.....	84
5.3.1. Moth-eye fabrication.....	84
5.3.2. Optical characterization.....	85
5.3.3. Effective medium calculations.....	87
5.4. Results and analysis.....	88
5.4.1. Effect of structure height and aspect ratio.....	88

5.4.2. <i>Optical characterization</i> .....	90
5.4.3. <i>Angular response of moth-eye structures</i> .....	94
5.5. <i>Conclusions</i> .....	96
5.6. <i>References</i> .....	98

**Chapter 6: A simple colloidal lithography method to fabricate large-area moth-eye anti-reflective structures on Si, Ge, and GaAs for IR applications.....** 100

6.1. <i>Chapter summary</i> .....	101
6.2. <i>Introduction</i> .....	101
6.3. <i>Experimental methods</i> .....	103
6.4. <i>Results and modeling</i> .....	105
6.5. <i>Summary and conclusions</i> .....	110
6.6. <i>References</i> .....	113

**Chapter 7: Enhancing near-infrared light absorption in PtSi thin films for Schottky barrier IR detectors using moth-eye surfaces.....** 116

7.1. <i>Chapter summary</i> .....	117
7.2. <i>Introduction</i> .....	117
7.3. <i>Experimental methods</i> .....	118
7.4. <i>Results and discussion</i> .....	120
7.5. <i>Conclusions</i> .....	125
7.6. <i>References</i> .....	126

## **Chapter 8: Microplasma-based synthesis of hierarchical semiconducting**

<b>metal oxide using Si moth-eye arrays.....</b>	<b>130</b>
<i>8.1. Chapter summary.....</i>	<i>131</i>
<i>8.2. Introduction.....</i>	<i>131</i>
<i>8.3. Experimental methods.....</i>	<i>132</i>
<i>8.4. Preliminary Results.....</i>	<i>135</i>
<i>8.5. Future work.....</i>	<i>138</i>
<i>8.6. References.....</i>	<i>140</i>

## LIST OF FIGURES

### **Chapter 1:**

- Figure 1: SEM micrographs of the eye of the moth.....3
- Figure 2: Schematic of the growth of protuberances on the eye of the moth.....4

### **Chapter 2:**

- Figure 1: Schematic of light incident on an interface.....12
- Figure 2: Refractive index of silicon.....17
- Figure 3: Refractive index of germanium (T~293K).....18
- Figure 4: Refractive index of gallium arsenide.....19
- Figure 5: Planar interface between materials 1 and 2 under normal-incidence  
illumination.....20
- Figure 6: Schematic of the angle-dependent geometry.....23
- Figure 7: Schematic of propagating waves through multi-layer systems.....25
- Figure 8: Total wave intensity for two interfering waves.....25
- Figure 9: SEM and transmission spectrum of a typical broadband AR coating.....27
- Figure 10: Calculated absolute transmission spectra of a bare silicon wafer,  
perfectly anti-reflecting single-sided coating, and a perfectly  
anti-reflecting double-sided coating.....29
- Figure 11: Schematic representation of a diffraction grating.....31
- Figure 12: Schematic representation of different optical regimes  
with respect to  $d/\lambda$ .....33
- Figure 13: One and two-dimensional subwavelength gratings designed as anti-  
reflecting structures.....36

Figure 14: Schematic of the effective medium approximation and transfer matrix algorithm.....	38
Table 1: Summary of simple effective medium approximations.....	39
Table 2: Summary of the geometry used to calculate $f$ for the effective medium approximation.....	41
Figure 15: Calculated refractive index profiles and transmission spectra for four basic shapes.....	41

### **Chapter 3:**

Figure 1: Overview of the colloidal lithography process.....	47
Table 1: Reaction conditions, particle diameters, standard deviations, and polydispersity for typical Stöber syntheses.....	49
Figure 2: Theorized concentrations of TEOS reactive species versus time.....	50
Figure 3: Experimental set-up to grow silica colloids via the modified semi-batch SFB method.....	51
Figure 4: Overview of the Langmuir-Blodgett method for making colloidal masks.....	53
Figure 5: Wilhelmy plate balance.....	53
Figure 6: Langmuir trough schematic and photograph.....	55
Figure 7: Michelson interferometer used in FTIR spectrometers and attachment to measure specular reflectance at $45^\circ$ .....	59
Figure 8: Integrating sphere photographs and schematic.....	60
Figure 9: Photograph and schematic of the $\theta$ - $2\theta$ goniometer	

built for the Bruker FTIR.....	61
--------------------------------	----

**Chapter 4:**

Figure 1: Process flow to fabricate moth-eye arrays in Si.....	70
Figure 2: Optical behavior of low aspect ratio (ar ~ 2) ME structures.....	73
Figure 3: Optical behavior of high aspect ratio (ar ~ 6) ME structures.....	75

**Chapter 5:**

Figure 1: SEM images of a moth eye.....	83
Figure 2: Experimental configuration for transmission, reflection, and diffuse scattering measurements.....	86
Figure 3: Relative transmission spectra of ME arrays with different feature heights (calculated and experimental) .....	89
Figure 4: SEM image of aspect ratio 9.4 moth-eye structure in Si fabricated with a 320nm mask.....	91
Figure 5: As-measured transmission, diffuse reflectance, forward scattering photon balance, and specular reflection for high aspect ratio Si moth-eye structures shown in Figure 3.....	92
Figure 6: Relative transmission of high aspect ratio ME structures compared to a commercial anti-reflective coating on Si.....	93
Figure 7: Experimental angle-dependent direct transmission of high aspect ratio moth-eye structures on Si.....	95

**Chapter 6:**

Figure 1: Large area SiO <sub>2</sub> colloidal crystal deposited on Si using Langmuir-Blodgetty, and process scheme to realize moth-eye	
---	--



structures on various substrates.....	104
Figure 2: Normalized single-side transmittance measured for moth-eye structured Si, Ge, and GaAs.....	107
Figure 3: Effect of shape and height of double-sided moth-eye protuberances on the absolute transmission calculated using effective medium theory.....	109
Figure 4: Absolute transmittance for double-sided moth-eye structured Si and Ge.....	111

**Chapter 7:**

Figure 1: Glancing angle XRD spectra and XPS spectra for as-deposited Pt films and annealed PtSi films.....	119
Figure 2: Experimentally measured absorption of PtSi films.....	120
Figure 3: Schematic representation of the effective medium approximation calculation, SEM of the moth eye films, and reflection and transmission spectra for different PtSi films.....	123
Figure 4: Calculated absorption, reflection, and transmission as a function of angle in the Si/PtSi/air stack at $\lambda=1.5\mu\text{m}$ .....	125

**Chapter 8:**

Figure 1: Schematic of the microplasma deposition system.....	133
Figure 2: Schematic of the process to produce hierarchical micro-arrays.....	135
Figure 3: SEM images and XRD patterns of NiO, CuO, and Fe <sub>2</sub> O <sub>3</sub> .....	136
Figure 4: CuO grown on different patterned Si Substrates.....	137

Figure 4: CuO grown on closed-packed frusta array, with  
increasing precursor flux.....138

# **Chapter 1**

---

## **Introduction**

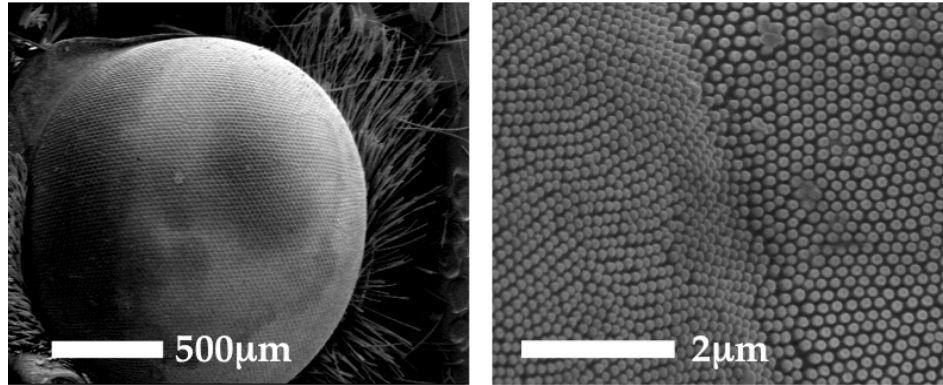
---

Interaction of electromagnetic waves with matter is a basic phenomenon that has been studied extensively for hundreds of years. Transmission and reflection of light at an interface is a fundamental process that is well understood, but inherently difficult to control. As such, scientists have been looking for ways to improve light transmission and control reflective properties of materials for decades. Reflection occurs because the electric and magnetic fields of light must obey Maxwell's equations at an interface (i.e., they must be continuous across the interface). If there is a difference between the refractive indices of the materials on either side of the interface, some portion of the wave will be reflected.

Traditionally, the problem of reflection from a surface has been circumvented by taking advantage of the wave properties of light and utilizing standing waves to obtain destructive interference between thin stacks of dielectric materials, reducing reflection at certain predictable wavelengths. Using this method, anti-reflective coatings can achieve very high transmission (>99%), but have a very narrow bandwidth and can be costly to manufacture [1,2]. Recently, however, a lot of attention has been garnered by how natural evolution has solved this problem. Biology offers a breadth of interesting ways to manipulate light, from the iridescent structural color of peacock feathers and blue butterflies to the broadband silvery tissue surrounding the squid eye [3]. The eye of the moth has also evolved to have sub-wavelength protuberances (Fig. 1), which effectively act as an anti-reflective surface, increasing light transmission to the light-sensitive cells within the eye, as well as decreasing reflection and diffraction [4,5]. This serves two functions for the moth; first, it increases the light reaching the photoreceptors of the moth eye in low light (at night), and second, it provides effective camouflage from predators by reducing glint from the eye. Protuberances smaller than the wavelength essentially create a smooth spatial variation in

refractive index, making the interface between the eye tissue ( $n=1.4$ ) and air ( $n = 1$ ) disappear, suppressing reflection [4].

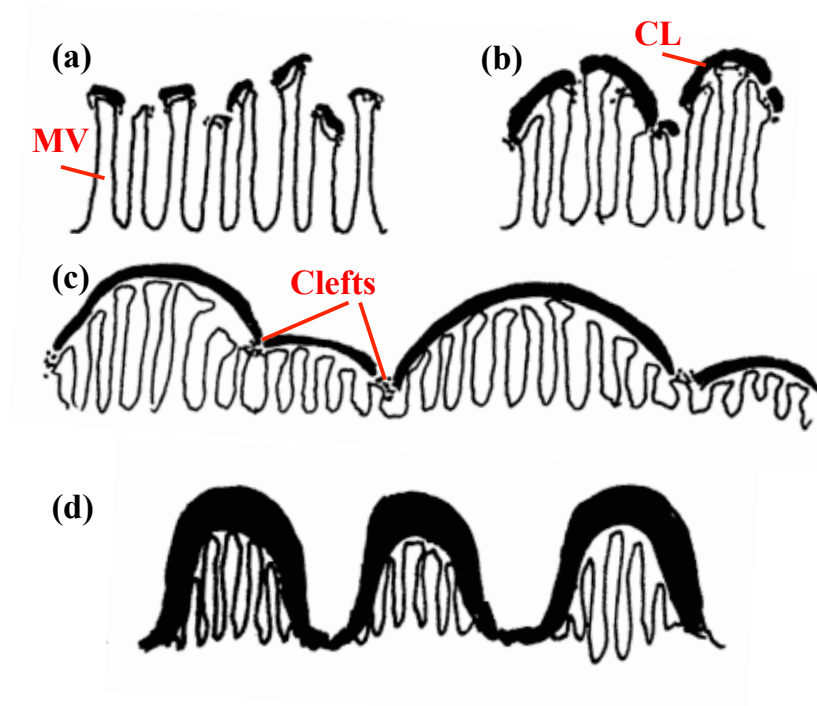
**Figure 1:** SEM micrographs of the eye of the moth, showing the subwavelength protuberances that comprise the anti-reflective layer



C. Behrard *et al.* [9] looked at the topography of the corneal surface in over three hundred insects and classified the protuberances on the surface in three categories: no significant height, low ( $\sim 50\text{nm}$ ), and large protuberance height ( $\sim 200\text{nm}$ ). They observed that larger full-sized protuberances only occurred in the genetically highest orders, Trichoptera and Lepidoptera (moths and butterflies), and hypothesized that the protuberances had evolved through modification of the formation of the cuticulin layer [10]. The cuticulin layer forms the outermost layer of the epicuticle of most insects, and is formed by secretions during either the molting or larvae stage of the insects' life [11]. Briefly, in the case of Lepidoptera, deposition of the cuticulin layer happens by secretions on the ends of microvilli, which are present in the corneogeneous cells in a hexagonally ordered fashion, in the first 4-5 days after pupation (Fig. 2a). As the cuticulin layer grows, it forms patches on top of the microvilli (Fig. 2b), then subsequently completely covers the surface, forming narrow clefts between patches (Fig. 2c). As it continues to grow, the layer begins to bulge outwards, forming individual protuberances (Fig. 2d). The subsequent growth and bulging

of the individual protuberances dictates the height of the final growths, but it is thought that the number of microvilli per protuberance is usually about equal [9-12].

**Figure 2:** Schematic of the growth of protuberances on the eye of the moth: (a) Secretions begin to form patches (b) on the end of the microvilli (MV) on the corneogeneous cells. (c) As the cuticulin layer (CL) begins to grow, filaments between the microvilli form to prevent buckling, and clefts form between cuticulin patches. (d) Continued growth forms bulges, which eventually fill and become individual protuberances. Adapted from [10,11].



The bulk of the research in the area of bio-mimicry with regards to anti-reflective moth-eye arrays has been focused primarily on suppressing visible and near-infrared (NIR) light reflection for both solar energy conversion and optics applications [2,6-8]. The bandwidth of these applications is relatively small, anywhere from 300-1500nm (visible light is 400-700nm). However, there are many applications which require the use of much broader wavelength ranges, especially extending into the near, mid, and far-infrared (NIR, MIR,

FIR). The amount of research on moth-eye arrays as a viable antireflecting treatment for infrared (IR) is very sparse, especially for wavelengths longer than those used for telecommunications ( $\sim 1.6\mu\text{m}$ ). The bandwidth spanning NIR ( $1\text{-}5\mu\text{m}$ ) to FIR ( $>50\mu\text{m}$ ) is considerably larger than for visible light; as a result, the design considerations and challenges for making antireflecting structured arrays are different.

Broadband anti-reflection, specifically in the IR, is important for IR signature management, IR optics, high index (thermo)photovoltaics [13], and IR detection for applications such as thermal imaging and hyper-spectral imaging [14], as well as low temperature IR astronomy [15,16]. Most MIR and FIR optics in astronomy utilize mirrors because lens optics have significant reflection losses [15]. Current state-of-the-art graded index anti-reflection coatings are produced by spin-coating porous organic layers [17], co-evaporation of mixed materials [18], interference lithography, electron-beam lithography [19] and sol-gel methods. Other methods of making anti-reflective coatings include multilayer stacks (as mentioned earlier), metamaterial “perfect” absorbers [20], and photonic crystals [1,2].

The goal of this work is to develop a facile, scalable, and defect-tolerant surface structuring method to produce moth-eye arrays to control IR reflectance over large bandwidths. The general approach to produce moth-eye arrays is to use a combination of colloidal lithography and reactive ion etching (RIE) to pattern silicon and other IR-relevant materials. This process platform enables independent control of mask size and pitch, as well as control of the profile of the resulting structures. Additionally, RIE etching of silicon is important to the electronics industry, so the existing infrastructure for pattern transfer

already exists. RIE also allows pattern transfer onto curved and complex surfaces without the need for multi-step processes.

In progress of the overall goal, the work will address several *questions* and *hypotheses*:

- (1) How do the size, pitch, and vertical profile change the optical behavior (e.g., transmission, scattering, reflectance, angle-dependent optical properties, absorbance, diffraction), of moth eye structures and how well does effective medium theory predict their behavior?
- (2) Can patterning disordered or quasi-ordered structures, as opposed to perfect arrays, be used to create a desired change in optical response (bandwidth,  $\theta$ -response, diffraction)? Can trading narrow-band fidelity (>99% transmission for a small  $\lambda$  window) be used to create broadband response which suppresses  $\theta$ -dependence and diffraction?
- (3) Can the scattering behavior of moth-eye surfaces be predicted using scalar diffraction theory? i.e., how do aspect ratio, height, pitch, shape, order/disorder and etch uniformity affect scattering and diffraction at low  $\lambda$ ?
- (4) Can the onset diffraction and diffuse scattering be engineered to be useful for application areas such as light trapping in detectors and solar cells?

In addition, this project aims to accomplish several key demonstrators of the capabilities of the moth eye approach, namely,

- anti-reflection by increasing (direct) transmission
- angle-independence of moth-eye structures by measuring  $\theta$ -dependent transmission
- control of optical response with process parameters (mask size, etch length, etc.)
- an adaptable process platform capable of patterning different materials



- scalability and process uniformity
- double-sided structures
- incorporation into relevant technology.

To understand the optical behavior of the structured films, as well as fully understand the fundamental scientific reasons behind anti-reflectance, diffraction suppression and improved transmission, it is crucial to rigorously characterize the materials produced. A full photon balance (e.g., absolute radiometric measurements), as well as angle-dependent measurements (i.e., both  $\theta$ - $2\theta$  and diffuse reflectance) are needed to fully characterize a sample. To achieve this in the NIR, MIR, and FIR, several custom systems were developed, including a Fourier transform infrared spectrometer (FTIR) with an integrating sphere and a  $\theta$ - $2\theta$  system. Also, theoretical models and transfer matrix calculations that can be correlated with experimental results were developed to intelligently design moth-eye structures.

## 1.1 References

- [1] S. Chattopadhyay, Y. F. Huang, Y. J. Jen, A. Ganguly, K. H. Chen, and L. C. Chen, “Anti-reflecting and photonic nanostructures,” *Mater. Sci. Eng. R* **69**, 1 (2010).
- [2] H. K. Raut, V. A. Ganesh, A. S. Nair, and S. Ramakrishna, “Anti-reflective coatings: A critical, in-depth review,” *Energy Environ. Sci.* **4**, 3779 (2011).
- [3] A. R. Parker and H. E. Townley, “Biomimetics of photonic nanostructures,” *Nat. Nanotechnol.* **2**, 347 (2007).
- [4] P. Clapham and M. C. Hutley, “Reduction of Lens Reflexion by the ‘Moth Eye’ Principle,” *Nature* **244**, 281 (1973).
- [5] P. I. Stavroulakis, S. A. Boden, T. Johnson, and D. M. Bagnall, “Suppression of backscattered diffraction from sub-wavelength ‘moth-eye’ arrays,” *Opt. Express* **21**, 1 (2013).
- [6] M. Phillips, P. Jiang, and B. Jiang, “Biomimetic broadband antireflection gratings on solar-grade multicrystalline silicon wafers,” *Appl. Phys. Lett.* **99**, 191103 (2011).
- [7] T. Kondo, T. Kitano, A. Suzuki, M. Mori, K. Naniwae, S. Kamiyama, M. Iwaya, T. Takeuchi, and I. Akasaki, “Advantages of the moth-eye patterned sapphire substrate for the high performance nitride based LEDs,” *Phys. Status Solidi* **11**, 771 (2014).
- [8] R. Brunner, B. Keil, C. Morhard, D. Lehr, J. Draheim, U. Wallrabe, and J. Spatz, “Antireflective ‘moth-eye’ structures on tunable optical silicone membranes,” *Appl. Opt.* **51**, 4370 (2012).
- [9] C. Bernhard, G. Gemne, and J. Sallstrom, “Comparative ultrastructure of corneal surface topography in insects with aspects on phylogenesis and function,” *Z. vergl. Physiologie* **67**, 1 (1970).

- [10] M. Locke, "The structures and formation of the cuticulin layer in the epicuticle of an insect, *Calpodes ethlius* (Lepidoptera, Hesperidae)," *J. Morph.* **118**, 461 (1966).
- [11] G. Gemne, "Ontogenesis of corneal surface ultrastructure in nocturnal Lepidoptera," *Phil. Trans. Roy. Soc. Lond. B* **252**, 343 (1971).
- [12] D. Stavenga, S. Foletti, G. Palasantzas and K. Arikawa, "Light on the moth-eye corneal nipple array of butterflies," *Proc. R. Soc. B*, **273**, 661 (2005).
- [13] C. Ferrari, F. Melino, M. Pinelli, P. R. Spina, and M. Venturini, "Overview and Status of Thermophotovoltaic Systems," *Energy Procedia* **45**, 160 (2014).
- [14] A. Rogalski, "Infrared detectors: an overview," *Infrared Phys. Technol.* **43**, 187 (2002).
- [15] T. Kamizuka, T. Miyata, S. Sako, H. Imada, T. Nakamura, K. Asano, M. Uchiyama, K. Okada, T. Wada, T. Nakagawa, T. Onaka, and I. Sakon, "Development of high-throughput silicon lens and grism with moth-eye antireflection structure for mid-infrared astronomy," *Proc. of SPIE* **8450**, 845051-3 (2012).
- [16] J. Lau, J. Fowler, T. Marriage, L. Page, J. Leong, E. Wishnow, R. Henry, E. Wollack, M. Halpern, D. Marsden, and G. Marsden, "Millimeter-wave antireflection coating for cryogenic silicon lenses," *Appl. Opt* **45**, 3746 (2006).
- [17] M. S. Park, Y. Lee, and J. K. Kim, "One-Step Preparation of Antireflection Film by Spin-Coating of Polymer/Solvent/Nonsolvent Ternary System," *Chem. Mater* **17**, 3944 (2005).
- [18] A. Ghosh and P. K. Bandyopadhyay, "Broad band antireflection coating on silicon from 1.5 to 6 $\mu$ m spectral band," *Infrared Phys. Technol.* **46**, 408 (2005).

- [19] C.-F. J. Kuo, H.-M. Tu, and T.-L. Su, "Optimization of the electron-beam-lithography parameters for the moth-eye effects of an antireflection matrix structure," *J. Appl. Polym. Sci.* **102**, 5303 (2006).
- [20] K. Wang, Z. Yu, S. Sandhu, V. Liu, and S. Fan, "Condition for perfect antireflection by optical resonance at material interface," *Optica* **1**, 388 (2014).

## **Chapter 2**

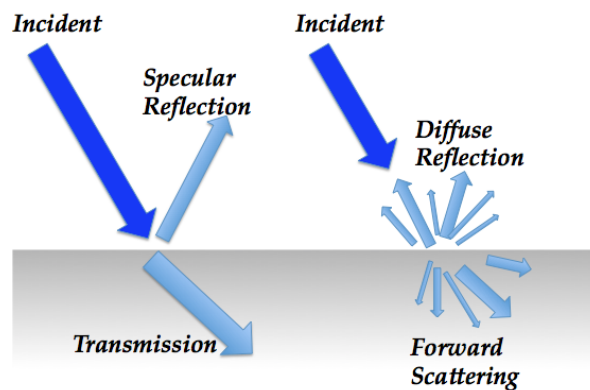
---

### **Background**

---

Electromagnetic radiation (light) incident on an interface can undergo several processes whereby the incoming photons are transmitted, absorbed or reflected (Fig 1). Specifically, light incident on a surface can be directly transmitted, forward scattered (transmitted via scattering), specularly reflected, diffusely scattered or absorbed. Diffraction, which is caused by wave interference due to wavelength-sized structures, can be regarded as forward and reverse “coherent” scattering. Specular reflection and direct transmission (0<sup>th</sup> order diffractive reflection and transmission) is described by a simple formalism known as the Fresnel equations.

**Figure 1:** Schematic of light incident on an interface.



In the following sections, a basic derivation of the Fresnel equations is outlined, and interference, the transfer matrix method to calculate wave propagation through layered media, and effective medium theory will be briefly explained. In addition, a brief overview of the current state of the literature with focus on moth eye structures is presented.

## 2.1. Light on planar surfaces

Reflection at an interface arises due to the necessary condition that electromagnetic waves must satisfy Maxwell's equations (i.e., continuity of field components) at the interface. In the simple case of planar interfaces between isotropic, homogenous media, this phenomenon is described by the Fresnel equations, which are derived below.

### 2.1.1. Maxwell's equations and complex refractive index

Maxwell's equations describe the propagation of EM waves through any medium:

$$\nabla \cdot \bar{E} = \frac{\rho}{\epsilon_0}, \quad (1)$$

$$\nabla \cdot \bar{B} = 0, \quad (2)$$

$$\nabla \times \bar{E} = -\frac{\partial \bar{B}}{\partial t}, \quad (3)$$

$$\nabla \times \bar{B} = \mu_0 \bar{J} + \mu_0 \epsilon_0 \frac{\partial \bar{E}}{\partial t}, \quad (4)$$

where  $\rho$  is the free charge density ( $\rho = 0$  in free space),  $\mu_0$  is the free space permeability, and  $\epsilon_0$  is the free space permittivity.  $\bar{E}$  and  $\bar{B}$  are the electric and magnetic fields, and  $\bar{J}$  is the current density. In a medium where there are no moving charges (e.g., a dielectric),  $\bar{J} = 0$  and (4) becomes:

$$\nabla \times \bar{B} = \mu_0 \epsilon_0 \frac{\partial \bar{E}}{\partial t}. \quad (4a)$$

These equations (1-4) give rise to the famous wave equation in free space (5), with plane wave solutions of the form (6):

$$\nabla^2 \bar{E} = \epsilon_0 \mu_0 \frac{\partial^2 \bar{E}}{\partial t^2}, \quad (5)$$

$$E = E_0 e^{i(\bar{k} \cdot \bar{r} - \omega t)}, \quad (6)$$

where  $\bar{k}$  is the wave vector,  $\bar{r}$  is the propagation direction and  $\omega$  is the frequency. From (6), it is clear that the propagation velocity of the moving wave is equal to  $(1/\epsilon_0 \mu_0)^{0.5}$ , which is defined as the speed of light in a vacuum,  $c$  ( $3.0 \times 10^8$  m/s). In a dielectric, the propagation velocity of the wave is related to the relative permittivity and permeability of the medium, such that

$$\frac{1}{v^2} = \mu_0 \mu_r \epsilon_0 \epsilon_r \quad \text{and} \quad (7)$$

$$v = \frac{1}{\sqrt{\mu_r \epsilon_r}} c. \quad (8)$$

The refractive index  $n$  of a material is defined as the ratio of the speed of light in vacuum to the group velocity of a wave in the medium (9), which, for plane waves, can also be expressed in terms of the wavevector and frequency (10):

$$n = \frac{c}{v} = \frac{1}{\sqrt{\epsilon_r \mu_r}}, \quad (9)$$

$$k = \frac{2\pi}{\lambda} = \frac{\omega}{v} = \frac{n\omega}{c}. \quad (10)$$

For a conductor, where  $\bar{J} = \sigma \bar{E} \neq 0$  in (4), the wave equation changes to include the effect of free moving charges:



$$\nabla^2 \bar{E} = \sigma \mu_0 \mu_r \frac{\partial \bar{E}}{\partial t} + \epsilon_0 \epsilon_r \mu_0 \mu_r \frac{\partial^2 \bar{E}}{\partial t^2}, \quad (11)$$

where  $\sigma$  is the electrical conductivity.

For a plane wave solution (6), the refractive index  $\tilde{n}$  must be complex to satisfy the definitions given by (9) and (10):

$$k = \tilde{n} \frac{\omega}{c}, \quad (13)$$

$$\tilde{n}^2 = \mu_r \epsilon_r + \frac{\mu_r \sigma}{\epsilon_0 \omega} i, \quad (14)$$

$$\tilde{n} = n + i\kappa, \quad (15)$$

where  $n$  and  $\kappa$  are the real and imaginary parts of the refractive index, respectively.  $\kappa$  is also known as the extinction coefficient, and is related to the absorption of light by a medium. For materials that are transmissive,  $\kappa = 0$ . It is important to note that, generally, both  $n$  and  $\kappa$  are strongly dependent on  $\lambda$  as

$$\tilde{n}(\lambda) = n(\lambda) + i\kappa(\lambda). \quad (16)$$

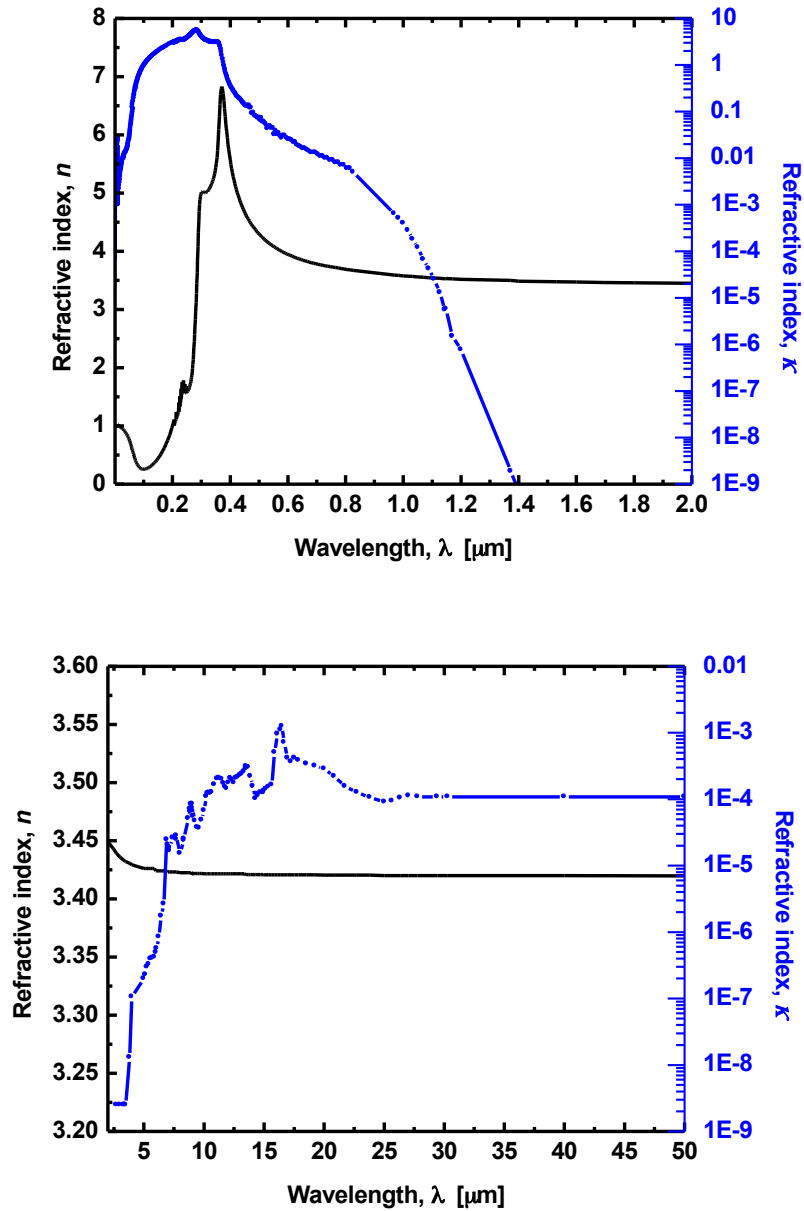
For typical materials,  $n$  and  $\kappa$  are positive, due to the fact that  $\mu \approx 1$  at optical frequencies. For typical dielectrics  $\kappa \rightarrow 0$ . However, certain engineered materials, such as metamaterials, can have effective refractive indices  $n < 0$ . For the purpose of this research, however, we will consider semiconductors and dielectrics which have a (mostly) real refractive index such that  $n > 0$  and  $\kappa \approx 0$ . For accuracy, however, all absorption and wavelength effects are taken into account in calculations via the wavelength-dependent refractive index of each material (e.g., Si, Ge, GaAs).

### 2.1.2. Infrared materials

In this work, the three main materials of interest for infrared applications are silicon (Si), germanium (Ge), and gallium arsenide (GaAs). All three materials are extensively used in the semiconductor industry, and have applications in photovoltaics, detectors, light emitting diodes (LEDs), and optics (lenses, windows, etc.) in the near, mid, and far IR (to THZ waves).

Silicon is an indirect gap (1.11eV) semiconductor that is commonly used in near IR optical systems, with high transmittance (low absorption) between 1.2-9 $\mu\text{m}$  and 20-300+ $\mu\text{m}$ . It is commonly used in applications where weight is a constraint, since it has very low density compared to other IR transmitting materials. Si has very good corrosion resistance, and it is not as brittle as Ge, yet it is harder, so it is a good option for harsh environments. In addition, it can easily be shaped with standard diamond polishing techniques. Typically, most broadband AR coatings for Si are made for the 3-5 $\mu\text{m}$  wavelength range. The refractive index of Si as a function of wavelength is shown in Figure 2. The real component of the refractive index,  $n$ , is  $\sim 3.42$  for most of the transmitting range. The absorption coefficient ( $\kappa$ ) is large below 1.2 $\mu\text{m}$ , which corresponds to the indirect gap of the material. The absorption peaks between 9-20 $\mu\text{m}$  are due to phonon dispersion (collective lattice oscillations) in the Si crystal. These peaks are weakly absorbing ( $\kappa < 10^{-3}$ ); for sample thicknesses of  $< 1\text{mm}$ , which are typical for this work, Si can be considered mostly transparent from 1.2 $\mu\text{m}$ -300 $\mu\text{m}$ .

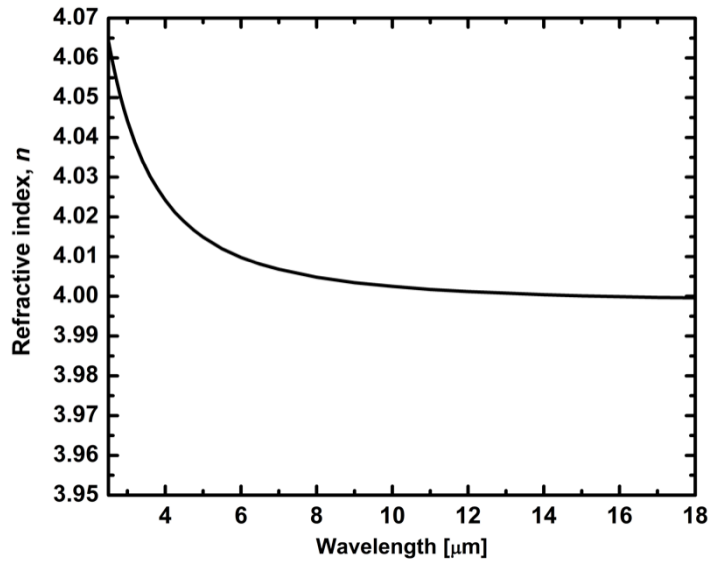
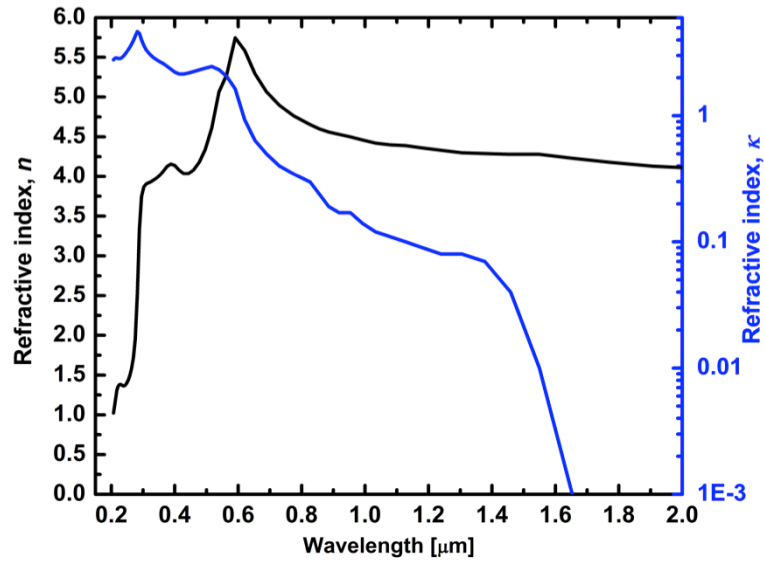
Figure 2: Refractive index of silicon [1-3].



Germanium is a semiconductor with an indirect bandgap of 0.67eV. It is used in infrared optical systems, as well as NIR detectors and thermal imaging systems, usually in the 3-5 $\mu\text{m}$  and 8-12 $\mu\text{m}$  spectral bands. It has the highest density and highest refractive index of any IR transmitting material (Fig. 3,  $n \sim 4.02$ ), which makes it desirable for lenses and optics. It is

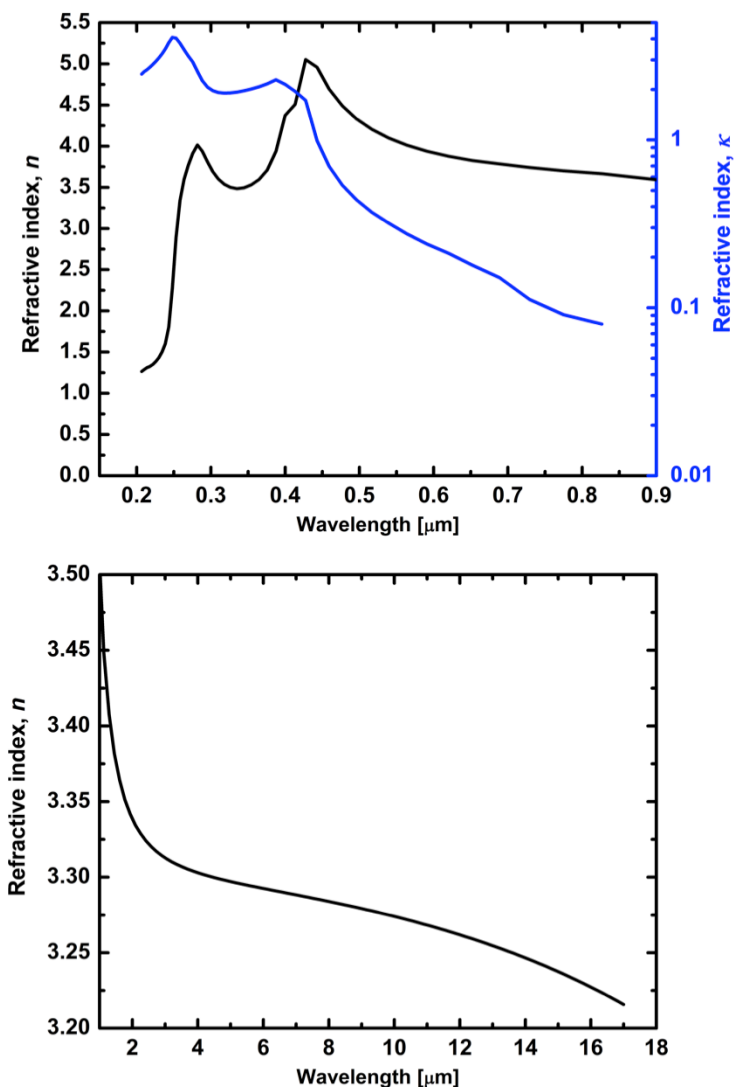
transparent from 2-14 $\mu\text{m}$  at low temperatures, but exhibits large increases in absorption with increasing temperature. Above 100°C, there is significant reduction in transmission, which can lead to runaway thermal absorption in high power systems. As such, active cooling is sometimes common in high-power applications or applications that require low loss.

**Figure 3:** Refractive index of germanium ( $T\sim 293\text{K}$ ) [1,2].



GaAs is a compound semiconductor with a direct bandgap of 1.43eV. It is widely used in high efficiency LEDs, multi-junction solar cells, and as a substrate for infrared detectors. It is also used in CO<sub>2</sub> laser systems and thermal imaging applications. Its refractive index (Fig. 4), is similar to that of Si. It is also very similar to Ge in terms of mechanical robustness, but has lower absorption in the 2-15μm range. Typical AR coatings for GaAs are made in the 3-5μm and 8-12μm spectral bands.

**Figure 4:** Refractive index of gallium arsenide [1,4,5].

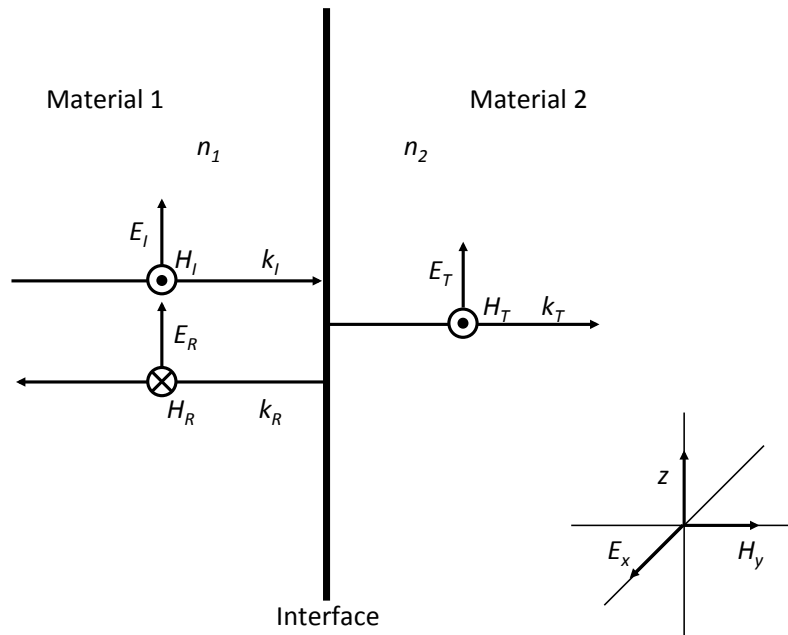


Other infrared-relevant materials include: HgCdTe (MCT), used for detectors [6], CdZnTe (CZT), a substrate material for detectors [6], ZnSe, GaN, CdTe, CaF<sub>2</sub>, CsBr, CsI, ZnS, quartz (SiO<sub>2</sub>), MgF<sub>2</sub>, KBr, KRS-5 (thallium bromiodide), and SiN.

### 2.1.3. Derivation of the Fresnel Equations

The basic description of the geometry is shown in Figure 5: a planar interface between different, homogenous, isotropic media. The simple case is where the incident light is normal to the plane of the interface. In this normal incidence case, it is not necessary to treat transverse electric (TE) and transverse magnetic (TM) polarization separately, because both the  $E$  and  $H$  fields are parallel to the interface. Otherwise, the boundary conditions given by (17) and (18) would change.

**Figure 5:** Planar interface between materials 1 and 2 under normal-incidence illumination. The light rays are described by the electric and magnetic fields ( $E$  and  $H$ ) and the wavevector  $k$ . The subscripts  $I$ ,  $T$  and  $R$  denote incident, transmitted, and reflected, respectively. The refractive indices of the materials are  $n_1$  and  $n_2$ . The inset shows the sign convention used for this geometry.



As stated earlier, at the interface, Maxwell's equations must hold. This gives rise to boundary conditions that the E and H fields parallel to the surface must be continuous at the interface. Also, E and H fields must be conserved across the boundary (notice the sign difference comes from the direction convention):

$$E_I + E_R = E_T, \quad (17)$$

$$H_I - H_R = H_T. \quad (18)$$

Taking the incident waves as plane waves of form (6), applying the boundary condition (18), and using the definition for refractive index (10), gives the condition:

$$\frac{\tilde{n}_1}{\mu_1}(E_I - E_R) = \frac{\tilde{n}_2}{\mu_2}E_T. \quad (19)$$

By combining (17) and (19), assuming  $\mu_1 = \mu_2 = 1$  (not a bad assumption at optical frequencies), and solving for reflected power (intensity  $I$  is equal to square of the amplitude of the E field) and transmitted power, one arrives at the simple case Fresnel equations:

$$R = |r|^2 = \left| \frac{E_R}{E_I} \right|^2 = \left| \frac{\tilde{n}_2 - \tilde{n}_1}{\tilde{n}_1 + \tilde{n}_2} \right|^2, \quad (20)$$

$$T = |t|^2 = \left| \frac{E_T}{E_I} \right|^2 = \frac{\tilde{n}_2}{\tilde{n}_1} \left| \frac{2\tilde{n}_1}{\tilde{n}_1 + \tilde{n}_2} \right|^2, \quad (21)$$

where  $r$  and  $t$  are the Fresnel coefficients, which can be complex values. It is important to note here that measurable quantities are the real parts of the E and H fields, and that any detector will measure energy density, or  $I$ , which is given by the time averaged energy density of the field (i.e.,  $\langle \mathbf{E}(\mathbf{r},t) \cdot \mathbf{E}(\mathbf{r},t) \rangle$ ). The Fresnel coefficients  $r$  and  $t$  are important later, as they are needed in the transfer matrix formulation to compute the reflectance and transmission of multi-layer stacks. The reflected power at an interface is directly related to

the square of the difference of the refractive indices of the two materials. For materials with high refractive indices like silicon or germanium, the power reflected at an air/semiconductor interface is high (~30-40%). For other high-RI materials used in thermophotovoltaics, such as GaSb, InGaAsSb, InGaAs, InPAsSb, PbTe, PbSnTe, PbSnSe, single-interface reflection can be >50%.

The same derivation can be done for light at any incident angle, which leads to slightly more complicated boundary conditions (i.e., components of the E and H fields that are parallel to the plane of incidence must be conserved across the interface). The result is reflected and transmitted powers that include an incident and transmission angle, which are related by Snell's law. The angle dependent versions of the Fresnel equations (22-25) are polarization dependent due to the introduction of geometry-dependent boundary conditions:

$$R_{TE} = r_{TE}^2 = \left| \frac{E_r}{E_i} \right|^2 = \left| \frac{(\tilde{n}_1 \cos(\theta) - \tilde{n}_2 \cos(\theta_t))}{(\tilde{n}_1 \cos(\theta) + \tilde{n}_2 \cos(\theta_t))} \right|^2, \quad (22)$$

$$R_{TM} = r_{TM}^2 = \left| \frac{E_r}{E_i} \right|^2 = \left| \frac{(\tilde{n}_1 \cos(\theta_t) - \tilde{n}_2 \cos(\theta))}{(\tilde{n}_1 \cos(\theta_t) + \tilde{n}_2 \cos(\theta))} \right|^2, \quad (23)$$

$$T_{TE} = t_{TE}^2 = \frac{\tilde{n}_2 \cos(\theta_t)}{\tilde{n}_1 \cos(\theta)} \left| \frac{2\tilde{n}_1 \cos(\theta)}{(\tilde{n}_1 \cos(\theta) + \tilde{n}_2 \cos(\theta_t))} \right|^2, \quad (24)$$

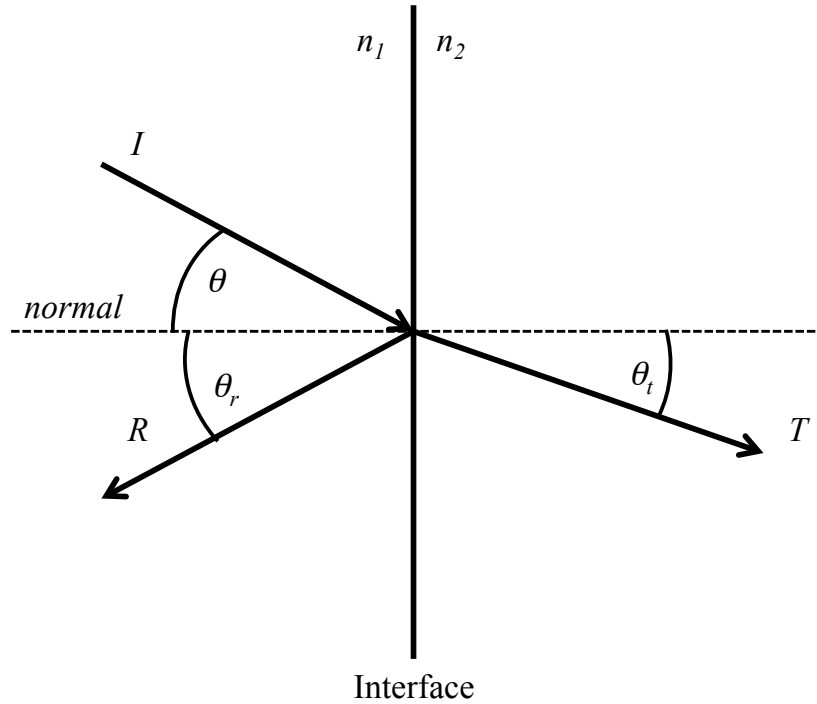
$$T_{TM} = t_{TM}^2 = \frac{\tilde{n}_2 \cos(\theta_t)}{\tilde{n}_1 \cos(\theta)} \left| \frac{2\tilde{n}_1 \cos(\theta)}{(\tilde{n}_1 \cos(\theta_t) + \tilde{n}_2 \cos(\theta))} \right|^2, \quad (25)$$

where  $\theta$  is the angle of incidence, and  $\theta_t$  is the transmission angle (Fig ). Snell's law gives the relationship between incident and transmitted angle:

$$n_1 \sin(\theta) = n_2 \sin(\theta_t). \quad (26)$$



**Figure 6:** Schematic of the angle-dependent geometry.  $I, R,$  and  $T$  represent the incident, reflected, and transmitted rays, respectively.  $\theta$  is the angle of incidence, and  $\theta_r$  and  $\theta_t$  are the reflected and transmitted angles.

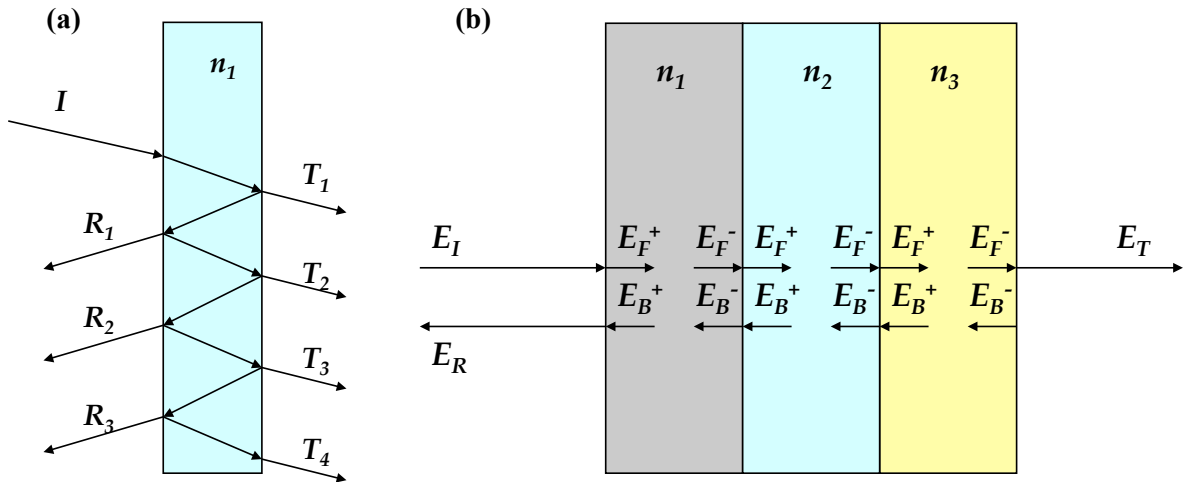


The Fresnel equations (22-25) are derived purely from Maxwell's equations essentially providing a balance on the EM wave, and explain interference, phase shifts, Brewster's angle, and evanescent waves. A similar derivation can be extended to multiple interfaces, which gives a simple transfer matrix method to calculate reflectance and transmission properties of multi-layer stacks. Furthermore, when coupled to an effective medium theory to model the refractive index of the moth-eye structures (discussed in section 2.4.), the transfer matrix method can be used as a model to predict the optical response of a moth-eye system.

### 2.1.4. Multiple interfaces: Interference and the transfer matrix formulation

Reflection and transmission at a single interface is described by the Fresnel equations (22-25). However, if there are multiple interfaces, the problem becomes slightly more complicated. The transmitted and reflected waves at each interface are a superposition of forward and backward travelling waves (Fig. 7a). As a result, there are waves that travel different path lengths, creating interference phenomena in the layers. Nevertheless, the system can be solved simultaneously via a transfer matrix that relates input and output waves at each interface.

**Figure 7:** (a) Schematic of a propagating wave through a single layer, double interface system. The total reflectance and transmission are a superposition of individual transmitted and reflected wave at each interface. (b) In multilayer stack, the transmitted and reflected waves at each interface are a superposition of the forward and backward traveling waves at the each side of the interface (+ or -). This gives rise to the transfer matrix formulation.



Interference can be explained briefly by examining the intensity of a total field,  $I$ , which can be written in terms of individual fields  $E_1$  and  $E_2$  of differing frequency, amplitude, and/or wavevector,  $\mathbf{k}$ . Like in (22-25), it is the intensity,  $I$ , of the field that is a measurable quantity [7]:

$$I = I(\vec{r}, t) = \langle (E_1(\vec{r}, t) + E_2(\vec{r}, t)) \cdot (E_1(\vec{r}, t) + E_2(\vec{r}, t)) \rangle , \quad (27)$$

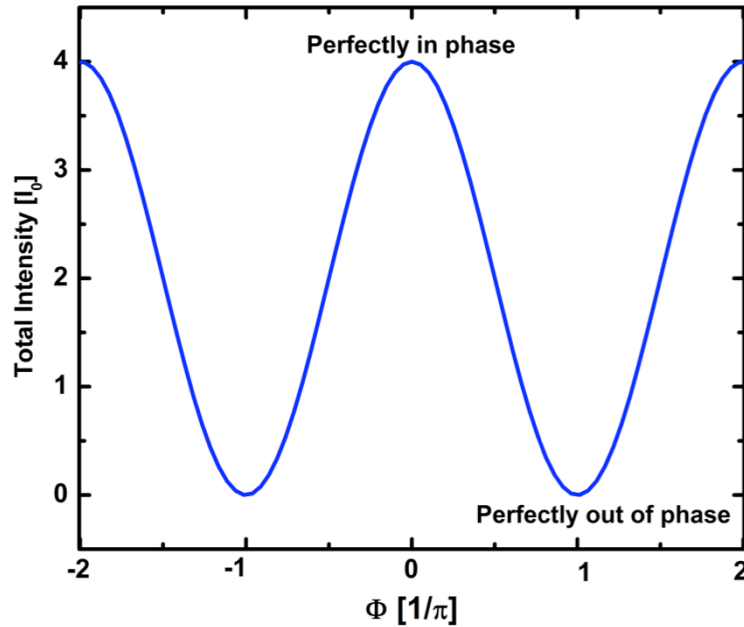
$$I = I_1 + I_2 + 2I_{12}, \quad (28)$$

where  $\bar{r}$  is the propagation direction and  $t$  is time. The first two terms of (27) and (28) are equal to the individual field intensities ( $I_1$  and  $I_2$ ) of the two waves, and the third term is the cross term ( $I_{12}$ ) that gives rise to interference. For two plane waves of the same amplitude and frequency, the phase difference of the two fields is  $(\mathbf{k}_2 - \mathbf{k}_1) \cdot \mathbf{r} + \delta(t)$ , where  $\delta(t) = \phi_1(t) - \phi_2(t)$  ( $\phi$  is the phase of the wave). The intensity of the resulting superposition of the two waves is [7]:

$$I = 4I_0 \cos^2\left(\frac{\Phi}{2}\right), \quad (29)$$

where  $I_0$  is the intensity of each of the individual waves, and  $\Phi = (\mathbf{k}_2 - \mathbf{k}_1) \cdot \mathbf{r} + \delta(t)$ . Depending on the phase difference and the wavevectors, the intensity of the total wave varies from 0 to  $4I_0$  (Fig. 8).

**Figure 8:** Total wave intensity for two interfering waves.



The derivation of the transfer matrix formulation is beyond the scope of this overview [8]; however, the basic idea is quite simple. The description of the problem is given in Figure 7(b): wave propagation through multilayer stack.

The transfer matrix  $\mathbf{T}_{ij}$  for the propagation of a wave *between* two layers  $i$  and  $j$  is given by

$$\mathbf{T}_{ij} = \frac{1}{t_{ij}} \begin{bmatrix} 1 & r_{ij} \\ r_{ij} & 1 \end{bmatrix}, \quad (30)$$

where  $r_{ij}$  and  $t_{ij}$  are the complex Fresnel coefficients (22-25) between layers  $i$  and  $j$ . The wave propagation *through* layer  $i$  is given by

$$\mathbf{T}_i = \begin{bmatrix} e^{i\delta_i} & 0 \\ 0 & e^{-i\delta_i} \end{bmatrix}, \quad (31)$$

where the sign of the exponential corresponds to forward and backward travelling waves and the phase difference in layer  $i$ ,  $\delta_i$ , is defined by

$$\delta_i = \frac{2\pi d_i}{\lambda} n_i \cos(\theta_i), \quad (32)$$

where  $d_i$  is the thickness of layer  $i$ . The complete transfer matrix formulation for the stack is found by multiplying all of the individual transfer matrices for each layer and interface:

$$\mathbf{T}_{0N} = \prod_{i=1}^N \mathbf{T}_{(i-1)i} \mathbf{T}_i, \quad (32)$$

where  $N$  is the total number of layers. Using this formulation, the transmission and reflection of any stack can be easily calculated.

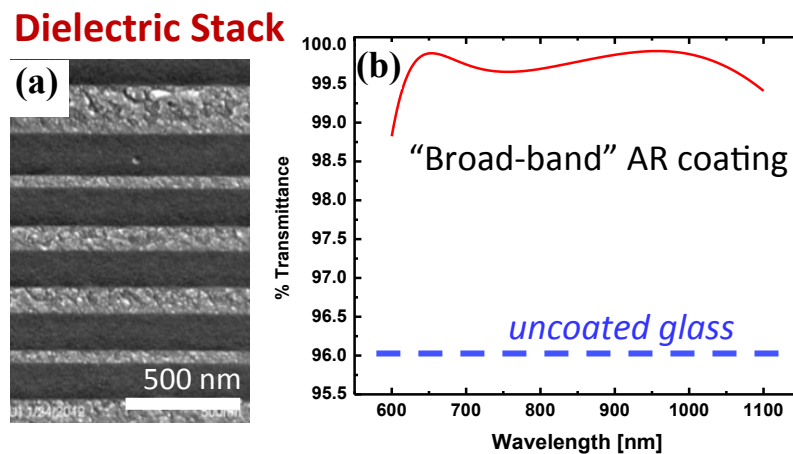
### 2.1.5. Interference-based anti-reflective coatings

The most common commercially available anti-reflectance coatings are interference-based. By designing a layered stack of varying thicknesses  $d_i$  and refractive indices  $n_i$ , the path length difference of the reflected wave can be tailored such that  $I_R$  approaches zero. This usually occurs when the thickness of the layer is equal to one quarter of the wavelength. Using the transfer matrix formalism, one finds that the refractive index of the coating,  $n_{AR}$ , must be

$$n_{AR} = \sqrt{n_0 n} \quad (33)$$

where  $n$  is the refractive index of the substrate and  $n_0$  is the refractive index of the surrounding medium. Commercial coatings use multiple layers ordered to achieve a broadband response and larger acceptance angle than a single layer (Fig. 9) [9].

**Figure 9:** (a) SEM of a multilayer dielectric stack used as a commercial anti-reflectance coating. (b) Transmission spectrum of a typical broadband anti-reflectance coating on glass. Adapted from Thorlabs.com.



For example, one type of infrared antireflective coating for HgCdTe (MCT) detectors uses five layers: ZnS/Ge/Zns/Ge/ZnS/CdZnTe (substrate) [10]. Unfortunately, interference-based coatings have several downsides: (1) Processing of multi-layer films on optical

components is costly and involved, because the film thickness and roughness has to be carefully controlled, (2) thin-film coatings are fabricated with several different materials, so they tend to be prone to fracture and thermal stresses due to different thermal expansion coefficients, as well as heating from standing waves (this can be an issue in high-power applications, such as CO<sub>2</sub> lasers), and (3), there are very few materials that can satisfy criteria (33) in the MIR and FIR [9,11,12]. Finally, when the substrate material is changed, the coating has to be re-engineered to take into account the refractive index of the substrate, which is fundamentally important in (33).

#### 2.1.6. Anti-reflection limits in single and double-sided coated transparent substrates

When comparing the anti-reflectance characteristics of any AR coating, one must take into account all of the interfaces in an optical geometry. For example, in an optical window or lens, there are two interfaces that contribute to the reflectance loss. Taking a 500μm Si window, if one calculates the reflectance and transmission from *each* interface using (20):

$$R_{Si/air} = \left| \frac{(\tilde{n}_{Si} - \tilde{n}_{air})}{(\tilde{n}_{Si} + \tilde{n}_{air})} \right|^2 = \left| \frac{(3.42 - 1)}{(3.42 + 1)} \right|^2 \approx 30\% \quad , \quad (34)$$

$$T_{Si/air} = 1 - R_{Si/air} = 70\% \quad . \quad (35)$$

However, from (32), we know that we must account for the total superposition of all of the waves from all interfaces (Fig.10, black), so the actual reflectance is 47% (a close approximation can be found by summing the reflectance from each interface sequentially:

$$R_{air/Si/air} \approx 0.3 + 0.3(1 - 0.3)^2 + 0.3(1 - 0.3)^2 + \dots \approx 47\% \quad . \quad (36)$$

This approximation only works because the thickness of the sample is much larger than the coherence length of the waves, so one does not need to worry about superposition, only field

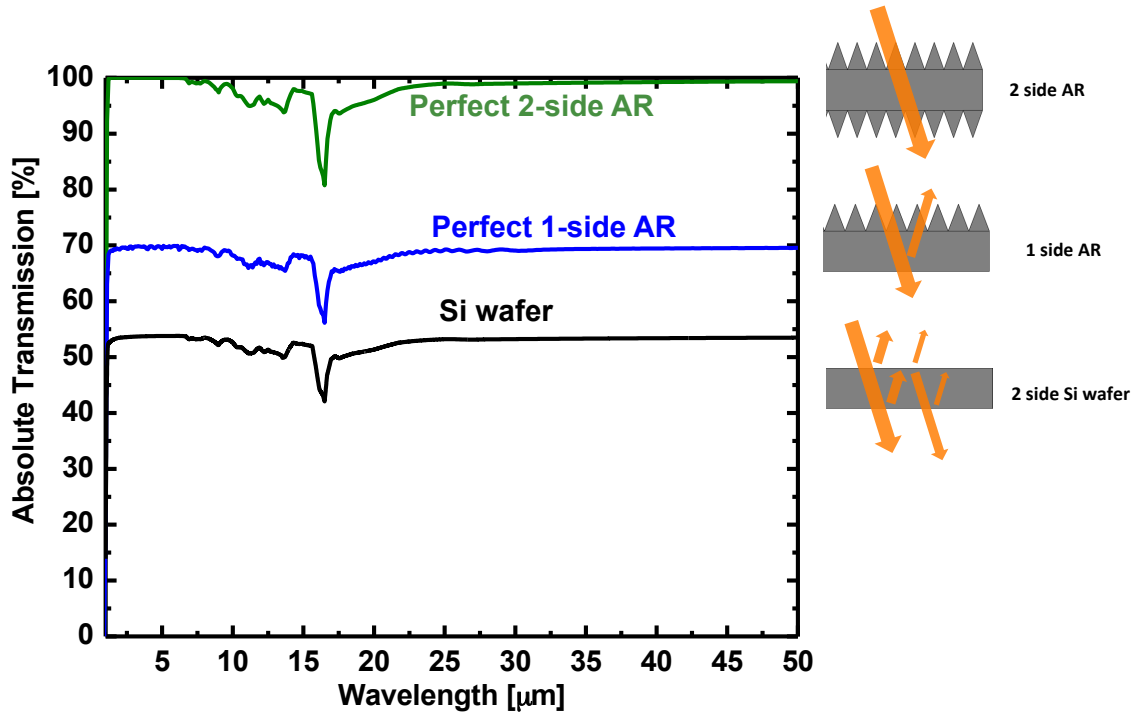
amplitudes. Given these considerations, if one side of the window is perfectly transmissive (anti-reflective), the total reflectance and transmission would then be (Fig 10, blue curve):

$$R_{air/AR/Si/air} \approx R_{Si/air} \approx 30\% \quad (37)$$

$$T_{air/AR/Si/air} \approx T_{Si/air} \approx 70\% \quad (38)$$

Finally, if both sides were perfectly transmissive, then the reflectance would be nonexistent, and transmission  $\rightarrow 100\%$  (Fig. 10, green curve).

**Figure 10:** Calculated absolute transmission spectra of a bare silicon wafer (black), a perfectly anti-reflecting single-side coating (blue), and a perfectly anti-reflecting double-sided coating (green). The dip in transmission around 16 $\mu\text{m}$  is due to absorption.



If, on the other hand, one has device geometry where there is a perfectly absorbing layer on the backside of a substrate (e.g., in an ideal detector), only one interface contributes to reflection losses.

## 2.2. Diffraction and light scattering

The previous discussion about light interaction with surfaces has only considered homogenous, planar surfaces. When surfaces are structured, the underlying physics (Maxwell's equations) do not change, but the interaction between the wave behavior of light and the surface structures make the solutions to these problems more involved. The interaction of light waves with periodic structures can be described in terms of different optical regimes, as described by the period of the structures normalized to the wavelength ( $d/\lambda$ ).

Diffraction, or dispersion, is described by the Huygens-Fresnel principle, whereby the superposition of waves originating from different point sources in space causes interference (as explained in section 2.14). Constructive interference occurs when the path length between waves is an integer multiple. In the case of a grating, for example, (Fig 11), the path length difference (red) depends on the angle of incidence ( $\theta$ ), wavelength ( $\lambda$ ), and pitch of the grating ( $d$ ). This is described by the generalized grating equation [13]:

$$d(n_2 \sin(\theta_m) - n_1 \sin(\theta_i)) = m\lambda, \quad (39)$$

where  $m = 0, \pm 1, \pm 2, \dots$  and is known as the diffraction order,  $\theta_m$  is the diffracted angle, and  $\theta_i$  is the incident angle.



**Figure 11:** Schematic representation of a diffraction grating. The path length difference between the two light rays is indicated in red.

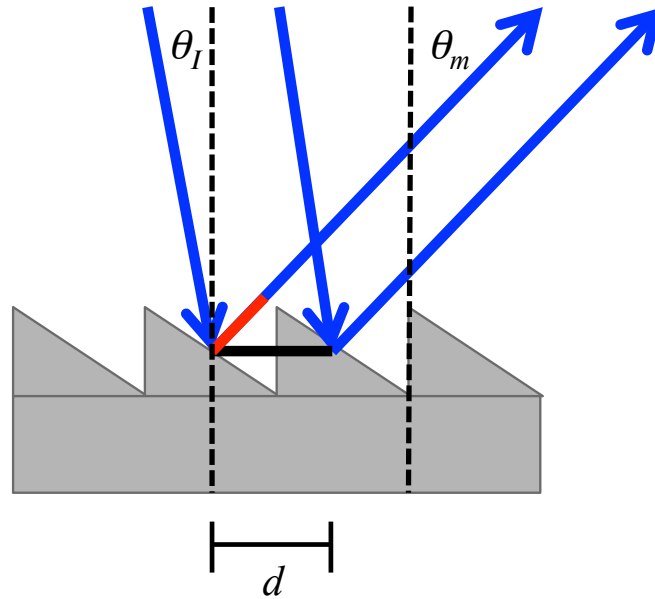
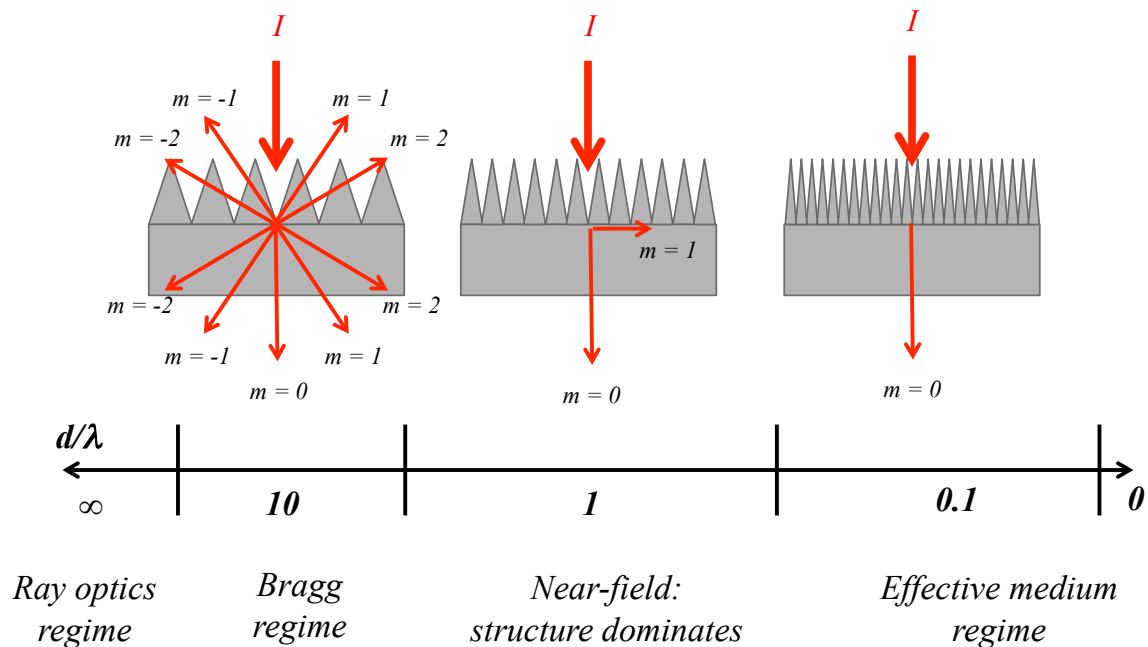


Figure 12 shows the general optics regimes with  $\lambda$  versus structure size. When the size of the structures is “infinitely” large compared to the wavelength, the interaction of light at interfaces is purely described by ray optics. In this regime, the Fresnel equations are perfectly quantitative, and predict the reflectance, transmission, and absorption at interfaces. As the size of the structures become comparable ( $d/\lambda \sim 10$ ) to the size of the wavelength, interference becomes important, and diffraction is the most accurate way of describing the interaction of light with these surfaces (Bragg regime, [14]). The phase behavior of the waves becomes crucially important, and dispersion (as in equation 33), is due to geometric effects. In this regime, more than one diffraction order can be present in both transmission and reflection, leading to significant “coherent” scattering. From equation (33), is it clear that nonzero diffraction orders will disappear when

$$d < \lambda/n_2 \quad (40)$$

for normal incidence. Around  $d/\lambda = 1$ , interesting optical phenomena occur, which is dominated by near-field evanescent waves. Optical metamaterials are designed in this regime, where cavities, resonators, rings, gratings, antenna, etc. are made to support modes where  $d = \lambda$ . For  $d/\lambda < 1$ , optical phenomena within periodic structures can be described by effective medium theory (discussed in depth in 2.3), where the light wave is significantly larger than the period of the structuration (infinite wavelength regime), and acts as if each layer in the film is a homogeneous surface. However, near-field effects must be taken into account to rigorously calculate the radiometric properties of a sub-wavelength structured surfaces. As such, finite difference time domain (FDTD), finite element (FEM) numerical methods, rigorously coupled wave analysis (RCWA), and Fourier modal expansion methods are typically used to model these surfaces [15]. However, effective medium theory gives a good approximation to calculate the response of moth-eye structures in the subwavelength regime [15].

**Figure 12:** Schematic representation of different optical regimes with respect to  $d/\lambda$ . The  $m$  index indicates the diffracted order.



### 2.3. Effective medium theory

Effective medium theory (EMT) aims to describe the propagation of electromagnetic radiation, as described by Maxwell's equations, through complicated media by treating inhomogeneous periodic structures as homogeneous media. In this way, calculations of the optical characteristics of the structure can be obtained using thin film methods. The basic idea is to describe the overall structure with an effective refractive index,  $n_{eff}$ , which is defined by the wave number of a propagation eigenmode,  $\beta$ , in the structure [16]:

$$n_{eff} = \frac{\beta}{k} = \frac{c}{\omega / \beta} . \quad (41)$$

When the period of the structure is small enough compared to the wavelength, per the diffraction equation,

$$d < \frac{\lambda}{(n_2 - n_1 \sin(\theta_1))} , \quad (42)$$

only the 0<sup>th</sup> order diffracted orders propagate in the structure (see section 2.2), and effective medium theory holds. However, when nonzero diffracted orders propagate through the structure ( $d/\lambda \sim 1$ ), effective medium theory is not valid, and the structure cannot be considered to be a homogeneous medium. It is generally accepted that EMT gives a good approximation of the effective refractive index of a material if  $d/\lambda < 0.1$ , provided the structure is periodic or quasi-periodic [15,17,18].

EMT was first developed to describe the propagation of light through one-dimensional diffraction gratings in the long-wavelength limit. In 1956, Rytov described the effective refractive index for one-dimensional lamellar structures [19]. In the field of diffraction optics and optical metamaterials, effective medium theories have been developed to describe one and two-dimensional periodic structures in the long-wavelength and quasi-static limit

[15,20-22]. In the case of one-dimensional and two-dimensional gratings, the polarization of EM waves gives rise to two effective refractive indices, depending on the orientation of the wavevector with respect to the grating vector (the grating vector,  $\mathbf{K}$ , is just a description of the direction and spacing of the grating planes) [23]. In general, however, as described by Lalanne and Lemercier-Lalanne [17,20,24], the effective refractive index can be described as a power series with respect to the  $d/\lambda$  parameter:

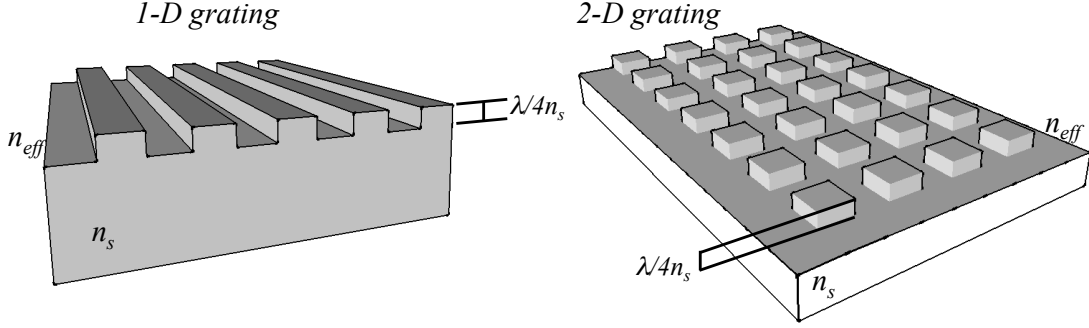
$$n_{eff} = n^{(0)} + n^{(2)}(d/\lambda)^2 + n^{(4)}(d/\lambda)^4 + \dots \quad (43)$$

where  $n^{(0)}$  is the effective refractive index in the static limit, and  $n^{(n)}$  are dimensionless coefficients based on the geometry of the structures. Some closed-form higher-order expressions for the effective refractive index of one-dimensional lamellar gratings and other simple periodic structures have been developed. Lalanne and Lemercier-Lalanne rigorously derived  $n_{eff}$  using a Fourier expansion method on the permittivity of the gratings.

In general, however, when the wavelength of interest is much larger than the period of the structure, the 0<sup>th</sup> order case gives a decent approximation of the effective optical constants of the structure. It should be noted that this treatment of effective refractive index does not take into account absorption, and has only been demonstrated for dielectric materials. In practice, no closed-form expressions for  $n_{eff}$  have been found for more complex two and three-dimensional structures.

Indeed, simple one and two-dimensional diffraction gratings have been fabricated and designed using rigorous EMT to behave as quarter-wave anti-reflective layers as described in section 2.2.3. Figure 13 shows the geometry of a typical one and two-dimensional subwavelength grating designed using EMT.

**Figure 13:** One and two-dimensional subwavelength gratings designed as anti-reflecting structures. Adapted from [21,23,25].



From Motamedi *et al*, the effective refractive index of these structures is given by [25]:

$$n_{eff} = \left| \frac{(1-f + fn_s^2)(1 + (1-f)n_s^2 + n_s^2)^{1/2}}{2(f + (1+f)n_s^2)} \right| \quad (44)$$

which is an average of the polarization-dependent effective refractive indices of the one-dimensional grating case [23]:

$$n_{eff}^{\perp} = (1-f + fn_s^2)^{1/2}, \quad (45)$$

$$n_{eff}^{\parallel} = (1-f + \frac{f}{n_s^2})^{-1/2}, \quad (46)$$

where  $f$  is the volume fraction of the structures in air, and  $n_s$  is the refractive index of the substrates, and  $\perp$  and  $\parallel$  correspond to perpendicular and parallel orientation of the E field with respect to the grating vector, respectively. The height of the grating is

$$h = \frac{\lambda}{4n_s}, \quad (47)$$

with the volume fraction  $f$  chosen so that equation (33) is satisfied. The use of subwavelength gratings to make  $\lambda/4$  thin films gives much finer control of the refractive index of the layer to match (33) by changing the filling factor,  $f$ . Motamendi *et al* reported a peak transmission of 92% at  $\sim 15\mu\text{m}$  using this method [25].

### 2.3.1 Effective medium approximations

In the case of graded refractive index (GRIN) structures, like the moth-eye structures, the effective refractive index of the structure as a function of height can be approximated in layers, with each layer acting as a lamellar grating in the infinite wavelength regime (see Fig. 14). Then, the total transmission, reflection, and phase retardation in the stack can be calculated using the transfer matrix method outlined above [15,18]. The number of layers must be large enough so that infinite-wavelength condition holds within each layer:

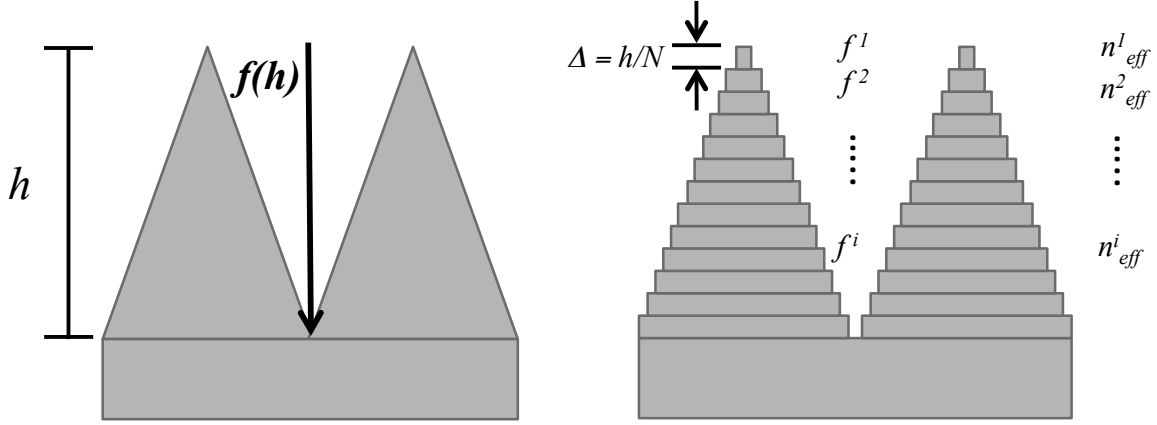
$$\Delta = \frac{h}{N} \ll \frac{\lambda}{n_s}, \quad (48)$$

where  $\Delta$  is the layer thickness,  $N$  is the total number of layers and  $h$  is the total height of the ME structure. When  $N$  is large and condition (48) is true, only the 0<sup>th</sup> order approximation from equation (43) is used, and is accurate with respect to  $h$ ; the other requirement is that  $d$ , the pitch of the structures also fulfills the infinite-wavelength criteria:

$$d \ll \frac{\lambda}{n_s}, \quad (49)$$

where  $n_s$  is the refractive index of the substrate. If both of these conditions are met, then  $n_{eff}^i$  (the effective refractive index in layer  $i$ ) can be calculated using one of a few basic effective medium approximations (EMA), including the Maxwell-Garnett, Bruggeman, and Lorentz-Lorentz models [9,11,15,22].

**Figure 14:** Schematic of the effective medium approximation and transfer matrix algorithm. The continuous structure, left, is treated as a stack of lamellar gratings with effective refractive indices  $n_{eff}^i$ , filling fraction  $f_i$ , and thickness  $\Delta$  (right). The optical characteristics are calculated using the transfer matrix formalism.



The first two models assume spherical, homogenous subwavelength inclusions of one material in another. The Maxwell-Garnett model is the original EMA for calculating an effective refractive index, and assumes small volume fractions of material 1 in material 2, with fill factors  $f$  and  $(1-f)$ . Bruggeman expanded the model to include mixtures of more than two materials, with fill factor  $f_k$  for the  $k^{\text{th}}$  component. The Lorentz-Lorentz model is based on molecular polarizability of two materials in a homogenous mixture. Table 1 outlines the three approximations. These methods are not rigorous for moth-eye systems, but allow a simple calculation of the  $0^{\text{th}}$  order effective refractive index in equation (43).



**Table 1:** Summary of simple effective medium approximations

<b>Model</b>	<b>Equation</b>	
<b>Maxwell-Garnett</b> [22,26]	$\frac{(n_{eff}^2 - n_1^2)}{(n_{eff}^2 + 2n_1^2)} = (1 - f) \frac{(n_2^2 - n_1^2)}{(n_2^2 + 2n_1^2)}$	Homogeneous mixture of subwavelength spherical inclusions of material 2 in material 1
<b>Bruggeman</b> [22,27]	$\sum_{i=1}^k f_i \frac{(n_i^2 - n_{eff}^2)}{(n_i^2 + 2n_{eff}^2)} = 0$	Extends the Maxwell-Garnett model to a mixture of $k$ materials
<b>Lorentz-Lorentz</b> [15]	$\frac{(n_{eff}^2 - 1)}{(n_{eff}^2 + 2)} = f \frac{(n_1^2 - 1)}{(n_1^2 + 2)} + (1 - f) \frac{(n_2^2 - 1)}{(n_2^2 + 2)}$	Based on the Clausius-Mossotti equation using the molecular polarizability of the components

The fill factor,  $f$ , is either calculated from a known shape, or experimentally measured by means of SEM image analysis. There are a lot of reported shapes and gradient index profiles found in the literature. Of these, so-called ‘‘Klopfenstein structures’’ (quintic index profiles) [28], tend to be regarded as the best shapes for broadband, omnidirectional, and high transmission [9,11,15]:

$$n_{eff}(z) = 1 + (n_s - 1)(10z^3 - 15z^4 + 6z^5) , \quad (50)$$

where  $z$  is the normalized distance from the substrate. Other structures with simple geometries are the basis of the EMA studies in this work. They include conical frusta and cones, parabolic and sinusoidal shapes. Table 2 summarizes the shapes, expressions to calculate the fill factors,  $f$ , and their geometry.

**Table 2:** Summary of the geometries used to calculate  $f$  for the effective medium approximation.

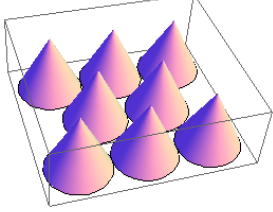
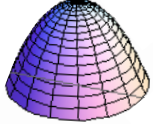
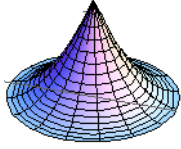
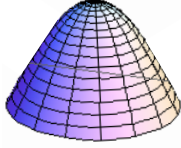
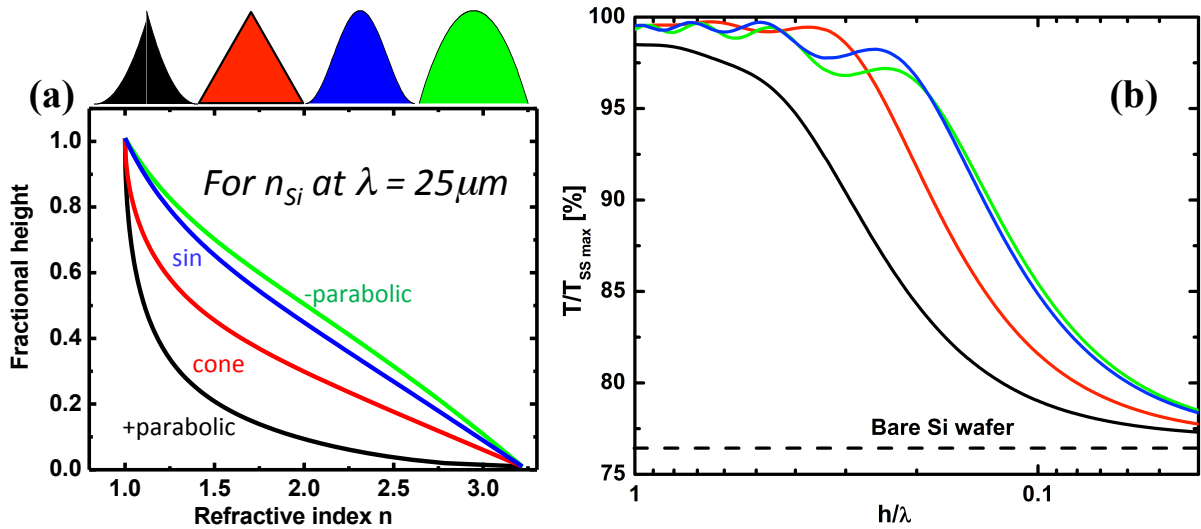
<i>Shape</i>	<i>Fill factor expression*</i>	<i>Geometry</i>
Cone or conical frustum	$f(z) = PF(1 - (1 - a)z)^2$ where $a$ is top-to-base diameter ratio ( $a = 0$ for cone)	
Convex Parabola	$f(z) = PF(z - 2\sqrt{z} + 1)$	
Concave parabola	$f(z) = PF(1 - z)$	
Sinusoidal	$f(z) = PF\left(\frac{2}{\pi} \cos^{-1}[z]\right)^2$	
* $z$ is normalized distance from substrate and $PF$ is the packing fraction on the substrate surface		

Figure 15(a) shows the calculated refractive index profiles for the shapes outlined in Table 2. The refractive index was calculated using the Bruggeman EMA, with  $PF = 0.907$ , corresponding to hexagonally closed-packed circles on a surface. 100 layers were used in the calculation, ensuring that condition (48) was met. The sinusoidal and convex parabolic shapes have the smoothest transitions from  $n_{si}$  to  $n_{air}$ , with the cone and concave parabolic shapes having more “steep” transitions. Figure 15(b) shows the calculated transmission spectra plotted against the  $h/\lambda$  parameter for these structures using the EMA and transfer

matrix formulation outlined above. From the EMA calculation, it is clear that the total height of the structures as well as the shape are crucial parameters to the performance of the moth eye layer. The total height must be comparable to the wavelength ( $h/\lambda > 0.1$ ) for reasonable anti-reflective behavior. In addition, concave shapes that produce “sharp” refractive index profiles do not achieve good anti-reflective properties.

In the results section, a more thorough analysis of shape effects and onset of scattering will be discussed.

**Figure 15:** (a) Calculated refractive index profiles for four basic shapes (inset) using the Bruggeman model. (b) Calculated  $T/T_{\text{Single Side Max}}$  versus  $h/\lambda$  for the four shapes. The sinusoidal and convex parabolic shapes have the most broadband properties.



#### 2.4. References

- [1] E. D. Palik, *Handbook of Optical Constants of Solids* (Academic Press, Boston, 1997).
- [2] H. H. Li, “Refractive index of silicon and germanium and its wavelength and temperature derivatives,” *J. Phys. Chem. Ref. Data* **9**, 561 (1980).
- [3] B. J. Frey, D. B. Leviton, and T. J. Madison, “Temperature dependent refractive index of silicon and germanium,” *Proc. SPIE* **6273**, 62732J (2006).
- [4] V. G. Plotnichenko, V. O. Nazaryants, E. B. Kryukova, and E. M. Dianov, “Spectral dependence of the refractive index of single-crystalline GaAs for optical applications,” *J. Phys. D. Appl. Phys.* **43**, 105402 (2010).
- [5] T. Skauli, P. S. Kuo, K. L. Vodopyanov, T. J. Pinguet, O. Levi, L. a. Eyres, J. S. Harris, M. M. Fejer, B. Gerard, L. Becouarn, and E. Lallier, “Improved dispersion relations for GaAs and applications to nonlinear optics,” *J. Appl. Phys* **94**, 6447 (2003).
- [6] A. Rogalski, *Infrared Detectors*, 2<sup>nd</sup> Edition, (CRC Press, Boca Ranton, 2011).
- [7] R. Baets, “Thin Films.” Universiteit Gent, (Gent, 2006).
- [8] C. Katsidis and D. Siapkas, “General transfer-matrix method for optical multilayer systems with coherent, partially coherent, and incoherent interference,” *Appl. Opt.* **41**, 3978 (2002).
- [9] H. K. Raut, V. A. Ganesh, a. S. Nair, and S. Ramakrishna, “Anti-reflective coatings: A critical, in-depth review,” *Energy Environ. Sci.* **4**, 3779 (2011).
- [10] B. D. MacLeod and D. S. Hobbs, “Long life, high performance anti-reflection treatment for HgCdTe infrared focal plane arrays,” *Proc. of SPIE* **6940**, 69400Y-12 (2008).
- [11] S. Chattopadhyay, Y. F. Huang, Y. J. Jen, A. Ganguly, K. H. Chen, and L. C. Chen, “Anti-reflecting and photonic nanostructures,” *Mater. Sci. Eng. R* **69**, 1 (2010).

- [12] J. Cai and L. Qi, "Recent advances in antireflective surfaces based on nanostructure arrays," *Mater. Horiz.* **2**, 37 (2014).
- [13] H. Ichikawa, "Numerical analysis of microretroreflectors: transition from reflection to diffraction," *J. Opt. A Pure Appl. Opt.* **6**, S121 (2004).
- [14] M. Moharam, T. Gaylord, and R. Magnusson, "Criteria for Bragg regime diffraction by phase gratings," *Opt. Commun.* **32**, 14 (1980).
- [15] K. Han and C.-H. Chang, "Numerical Modeling of Sub-Wavelength Anti-Reflective Structures for Solar Module Applications," *Nanomaterials*, **4**, 87 (2014).
- [16] H. Kikuta, H. Toyota, and W. Yu, "Optical Elements with Subwavelength Structured Surfaces," *Opt. Rev.* **10**, 63 (2003).
- [17] P. Lalanne and M. Hutley, "The optical properties of artificial media structured at a subwavelength scale," *Encycl. Opt. Eng.*, 1–11 (2003).
- [18] E. B. Grann and M. G. Moharam, "Comparison between continuous and discrete subwavelength grating structures for antireflection surfaces," *J. Opt. Soc. Am. A* **13**, 988 (1996).
- [19] S. M. Rytov, "Electromagnetic properties of a finely stratified medium," *Sov. Phys. JETP* **2**, 466 (1956).
- [20] P. Lalanne and D. Lemerrier-Lalanne, "Depth dependence of the effective properties of subwavelength gratings," *JOSA A*, **14**, 450 (1997).
- [21] H. Kikuta, Y. Ohira, H. Kubo, and K. Iwata, "Effective medium theory of two-dimensional subwavelength gratings in the non-quasi-static limit," *J. Opt. Soc. Am. A* **15**, 1577 (1998).

- [22] G. A. Niklasson, C. G. Granqvist, and O. Hunderi, "Effective medium models for the optical properties of inhomogeneous materials," *Appl. Opt.* **20**, 26 (1981).
- [23] T. K. Gaylord, W. E. Baird, and M. G. Moharam, "Zero-reflectivity high spatial-frequency rectangular-groove dielectric surface-relief gratings," *Applied Optics* **25**, 4562 (1986).
- [24] P. Lalanne and J. Hugonin, "High-order effective-medium theory of subwavelength gratings in classical mounting : application to volume holograms," *J. Opt. Soc. Am. A*, **15**, 1843 (1998).
- [25] M. E. Motamedi, W. H. Southwell, and W. J. Gunning, "Antireflection surfaces in silicon using binary optics technology," *Appl. Opt.* **31**, 4371 (1992).
- [26] J. C. Garnett, *Philos. Trans. R. Soc. London* **203**, 385 (1904).
- [27] D. A. Bruggeman, *Ann. Phys. Leipzig*. **24**, 636 (1935).
- [28] R. Klopfenstein, "A Transmission Line Taper of Improved design," *Proc. IRE* **38**, 31 (1956).

## **Chapter 3**

---

### **Experimental Methods and Instrument Development**

---

### 3.1. Colloidal lithography

Moth-eye arrays and random graded refractive index (GRIN) structures have been fabricated in different materials (Si, glass, polymers) by different methods over the years, including interference, deep-UV, nano-imprint, and e-beam lithography; self-masking (black Si), dewetted metal masking, wet etching, laser-assisted etching, and colloidal lithography. Each of these methods provides different benefits, and must balance a few restrictions: ease of fabrication, cost, scalability, resolution, substrate-dependence, and introduction of imperfections. Typically, top-down methods like electron-beam lithography provide very good resolution, and have very good reproducibility and fidelity, but are prohibitively expensive. They offer a great deal of control in terms of order, structure packing density, pitch size ( $d$ ), and selectivity, but can only be applied to small areas ( $\sim 1\text{ cm}^2$  at most). On the other hand, bottom-up methods like self-masking and wet etching methods are very inexpensive and easy to implement, but offer little to no control of design parameters such as height, pitch, and structure profile. In addition, GRIN structures made from bottom up methods are completely random, which introduces a significant amount of scattering. However, these bottom-up methods can be applied to very large area substrates without much specialized equipment.

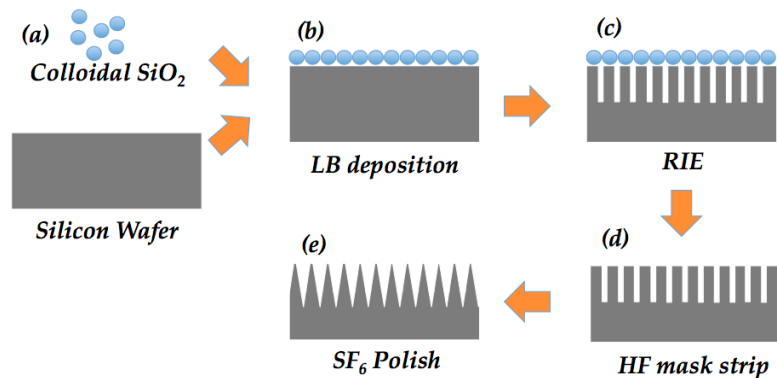
Colloidal lithography offers a compromise between top-down and fully bottom-up methods, giving a moderate amount of control of tunable parameters such as feature pitch, height, packing density, and profile. The idea of colloidal lithography was introduced and developed by the pioneering work of Fischer and Zingsheim [1], Van Duyne [2], Deckman and Dunsmuir [3], and Zhang and Wang [4], who produced a breadth of two and three dimensional structures using colloidal templates.



Moth-eye structures in this work were fabricated using a colloidal lithography method outlined in Figure 1. Using simple silane chemistry and Langmuir-Blodgett methods, large area (wafer size) 2D colloidal crystals can be formed on any substrate relatively quickly. In addition, by using well-established dry etching techniques such as reactive ion etching, high-aspect ratio structures were realized.

Monodisperse silica colloids of the desired size (100nm-5 $\mu$ m) were synthesized via a modified Stöber process and functionalized via silane chemistry to tune the hydrophobicity of the particle surface. The particles were deposited on the substrate material via a Langmuir-Blodgett (LB) process to achieve an ordered, close-packed or disordered monolayer on the surface. The colloidal monolayer was used as a mask for pattern transfer using dry etching (RIE). This method is capable of producing high aspect ratio structures in Si, and is extendable to many other materials. The resulting structures were cleaned and polished in an HF/HNO<sub>3</sub> bath and/or an SF<sub>6</sub> plasma to remove any silicon dioxide mask or oxide formed in the plasma as well as taper the structures. Each step in the process, along with descriptions of the instruments, will be discussed in the following sections.

**Figure 1:** Overview of the colloidal lithography process used to produce moth-eye structures on Si: (a) First, the colloidal silica was synthesized by a modified Stöber process. (b) Monolayers were then deposited on a Si wafer by LB deposition. (c) The mask pattern was transferred to the substrate directionally by RIE. (d) Last, the mask was removed by an HF dip, and the structures polished with an SF<sub>6</sub> plasma.



### 3.1.1. Synthesis of colloidal silica

Nano and microscopic silica colloids are used today in a range of application areas including biology, photonics, microfluidics, as well as in industrial applications such as adhesives and food additives [5]. Silica is widely used for colloidal lithography methods due to its flexible surface chemistry, robustness, and compatibility with Si and high vacuum processes. SiO<sub>2</sub>, for example, exhibits relatively good selectivity in dry etching chemistries for semiconductors, so it can be used directly as an etch mask. In addition, a lot of research has been done in the controlled synthesis and surface modification of colloidal suspensions, which can be leveraged for the Langmuir-Blodgett approach [6].

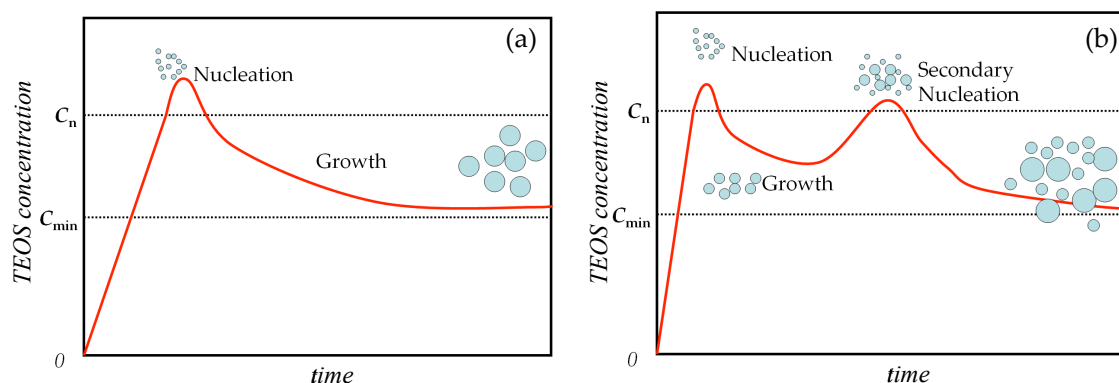
Silica was the first inorganic type of monodisperse colloid to be synthesized by solution methods. In 1968, Stöber, Fink and Bohn [7] published a synthesis procedure using ammonia as a catalyst for the hydration and condensation reaction of different organo-silane precursors, notably tetraethyl orthosilicate (TEOS), under different reactant conditions. Stöber *et al.* meticulously outlined reaction conditions, including water concentration, ammonia concentration, TEOS concentrations, and temperature, to catalog particle sizes from 5nm to several hundred nanometers. In 1987, Bogush *et al.* [8] published a series of papers extending Stöber's work to growth of larger particles, control of monodispersity, and electrolyte effects. Many other authors contributed to the field; now, the Stöber Fink and Bohn (SFB) process for making silica colloids is considered the easiest and most widely used method. In the early 1990's, several authors (notably Van Blaaderen *et al.* [9], and Giesche *et al.* [10,11]) published work outlining a seeded regrowth method to grow larger particles of low polydispersity.

In this work, silica particles with <10% polydispersity were synthesized using a modified semi-batch Stöber-Fink-Bohn method (Table 1): a silica precursor (tetraethyl orthosilicate, TEOS, Alfa Aesar) was hydrolyzed in the presence of an ammonia catalyst (NH<sub>4</sub>OH) in an ethanolic medium[7,8,12,13]. Particles were washed six times (Milli-Q H<sub>2</sub>O, 18.3 MΩ·cm) to achieve a neutral solution pH and remove unreacted TEOS. The concentration of the reactive species was carefully controlled to prevent secondary nucleation of particles (Fig. 2).

**Table 1:** Reaction conditions and final particle diameter, standard deviations, and polydispersity (measured by SEM) for four typical modified Stöber syntheses.

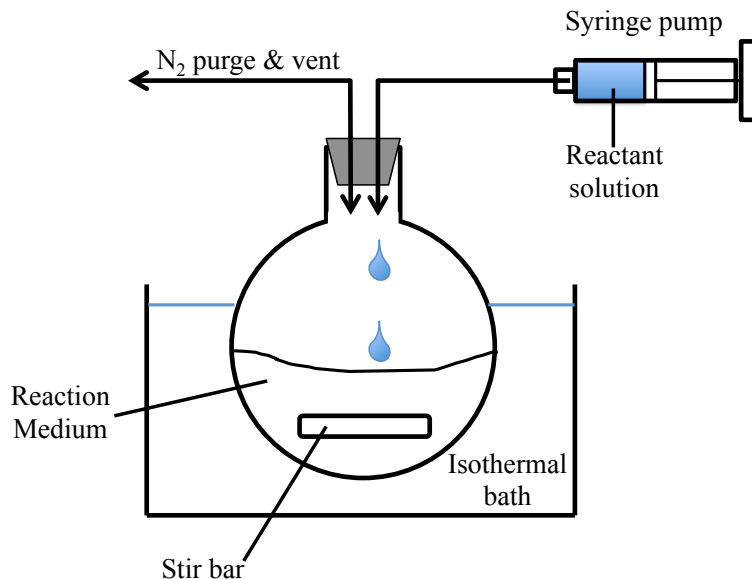
Reaction Type	Reaction Medium	Reactant Solution	D <sub>final</sub> [μm]	σ [μm]	Polydispersity
Semi-Batch	200mL EtOH 20mL 30% NH <sub>4</sub> OH	25mL EtOH 25mL TEOS @8mL/hr	1.02	0.09	0.09
Semi-Batch	200mL EtOH 30mL 30% NH <sub>4</sub> OH	30mL EtOH 30mL TEOS @8mL/hr	1.23	0.10	0.08
Semi-Batch	200mL EtOH 30mL 30% NH <sub>4</sub> OH 5mL H <sub>2</sub> O	30mL EtOH 30mL TEOS @8mL/hr	1.19	0.13	0.11
Semi-Batch	200mL EtOH 22mL 30% NH <sub>4</sub> OH	40mL EtOH 10mL TEOS @8mL/hr	0.376	0.046	0.12

**Figure 2:** Theorized concentration of TEOS reactive species versus time. (a) At a high enough concentration,  $C_n$ , particles nucleate from solution. Above a minimum concentration,  $C_{min}$ , the particles will grow. (b) If the concentration reaches  $C_n$  during the reaction, secondary nucleation can occur, spoiling the monodispersity of the colloidal suspension. The feed flowrate of the reactant solution is optimized to keep the concentration of TEOS between  $C_{min}$  and  $C_n$ .



It was hypothesized by Kim *et al.* [14] that the polydispersity and size of the resulting colloids are directly related to the rate of hydrolysis of TEOS. Therefore, the optimum conditions are those which limit the reaction rate. A semi-batch reaction scheme [11] was used to maintain the concentration of TEOS as constant as possible to promote growth of particles and prevent secondary nucleation (Fig. 2). The reaction medium (EtOH, H<sub>2</sub>O, and NH<sub>4</sub>OH) was stirred vigorously in an isothermal bath while the reactant solution (TEOS in EtOH) was added dropwise by a syringe pump (Fig. 3). Changing the molar ratio of H<sub>2</sub>O/TEOS, concentration of NH<sub>4</sub>OH, reactant solution feed flowrate, and the temperature controls the rate of hydrolysis and therefore the final particle size and polydispersity. Typical synthesis conditions are given in Table 1.

**Figure 3:** Experimental set-up to grow silica colloids via the modified semi-batch SFB method.



To maximize the size of the resulting silica, slow, cold ( $\sim 273\text{K}$ ), dilute conditions were used. Reactions for large ( $>1\mu\text{m}$ ) particles lasted for several days.

Silica particles were rendered hydrophobic by functionalization with allyltrimethoxysilane (ATMS) [6,15–21]. The aqueous suspension of silica particles was dried under vacuum at  $423\text{K}$  for two hours to remove as much adsorbed water as possible[22], then the particles were re-suspended in ethanol (EtOH) under sonication for one hour to approximately 1% by volume concentration. The suspension was made acidic (pH 5.5) by addition of acetic acid. Enough water was added to make the solution 10% water by volume, which aids in the hydrolysis of the functional group.

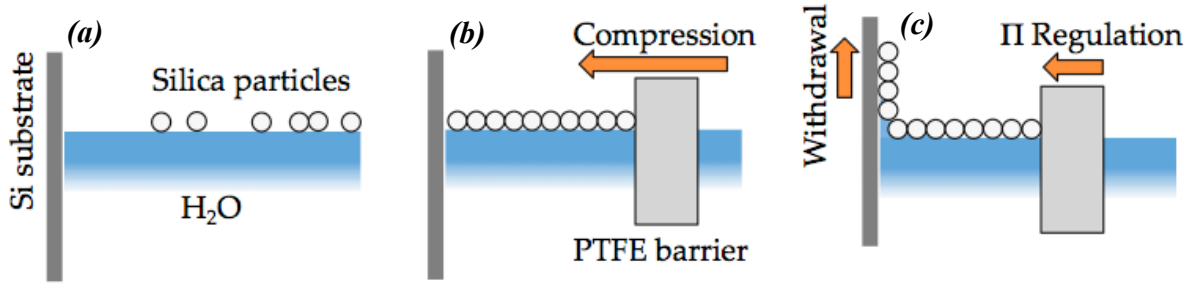
To ensure coupling of the functional group, excess ( $>30\mu\text{L}$ ) of ATMS was used per 10mL of suspension. The mixture was heated to  $353\text{K}$  for several hours to promote covalent bonding to the silica surface. The particles were then washed twice via centrifugation and re-dispersal in EtOH, and then dried in a vacuum oven overnight at  $423\text{K}$ .

Dried particles were then re-dispersed in EtOH/chloroform (0.5% particles by volume) for use in the Langmuir trough. The functional group on the trimethoxysilane renders the silica particles hydrophobic. The choice of functional group (allyltrimethoxysilane, methyltrimethoxysilane, isobutyltrimethoxysilane, tert-butyltrimethoxysilane, n-octyltrimethoxysilane, or benzytrimethoxysilane) had very little impact on the quality of the formed monolayers. However, it has been previously shown that a vinyl (ATMS) group allows better quality monolayers to be formed than other coupling agents (such as  $\text{NH}_2$ ) [6,16,18–20].

### *3.1.2. Langmuir Blodgett trough and Wilhelmy plate apparatus*

The Langmuir-Blodgett (LB) technique allows fabrication of wafer-sized monolayers of silica particles that can be rapidly deposited on many types of substrates. In addition, the packing density of the silica particles can be controlled. An LB system consists of a trough, Wilhelmy plate to measure surface pressure, and a dip coater. A monolayer is made by suspending functionalized, hydrophobic silica colloids on the interface between water and air via a chloroform/ethanol solution (Fig. 4a). The surface is then compressed by means of a movable barrier, inducing the particles to self-assemble into a hexagonally packed monolayer (Fig. 4b). The monolayer is then transferred to a substrate via a vertical dip coating step, while holding the surface pressure constant (Fig. 4c).

**Figure 4:** Overview of the Langmuir-Blodgett method for making colloidal masks: (a) Silica particles are suspended on a water subphase using a mixture of ethanol and chloroform, (b) compressed using a PTFE barrier until close-packed, and (c) deposited on the substrate while regulating the surface pressure,  $\Pi$ .



During the compression and dip coating, the surface pressure,  $\Pi$  (mN/m), is measured using a Wilhelmy plate. The surface pressure is defined as:

$$\Pi = \gamma_0 - \gamma \quad (1)$$

where  $\gamma_0$  is the surface tension of water ( $\sim 70$  mN/m) and  $\gamma$  is the surface tension of the monolayer. To measure the surface pressure, the deflection of a small leaf spring connected to a paper Wilhelmy plate is measured (Fig 5). A force balance on the Wilhelmy plate gives the force ( $F$ ) exerted on the spring:

$$F = mg + 2w_p\gamma \cos(\theta) - \rho V_p g, \quad (2)$$

where  $mg$  is the gravitational force,  $\rho V_p g$  is the buoyancy force of the paper ( $V_p$  is the volume of the paper,  $\rho$  is the density) and  $2w_p\gamma \cos(\theta)$  is the force due to the surface tension ( $\theta$  is the wetting angle, and  $w_p$  is the width of the paper). If the wetting is assumed to be perfect ( $\cos(\theta) = 1$ ), and small changes in the buoyancy force are ignored, the change in the force due to changes in surface tension applied to the spring can be approximated as:

$$\Delta F = 2w_p \Delta\gamma. \quad (3)$$

In addition, from Hooke's law, the deflection of the spring is linear with respect to the force applied to the spring:

$$\Delta F = k\Delta x . \tag{4}$$

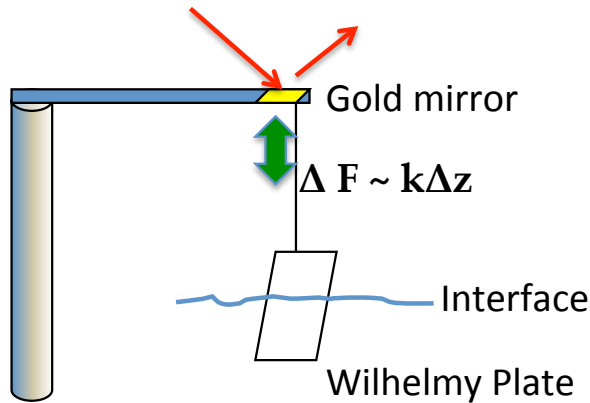
It is easy to see by substituting (3) into (4),

$$k\Delta x = 2w_p\Delta\gamma , \text{ and} \tag{5}$$

$$\Delta\gamma = \Pi = \frac{k\Delta x}{2w_p} , \tag{6}$$

so the surface pressure can be measured directly by measuring the deflection of the leaf spring. If a spring with a small spring constant ( $k \sim 10^{-2}$  N/m) is used, very small changes in surface pressure can be measured.

**Figure 5:** Wilhelmy plate balance: the deflection of a leaf spring, proportional to the force applied by the plate, is measured using a laser (red arrows) reflected off a gold mirror on the end of the spring.

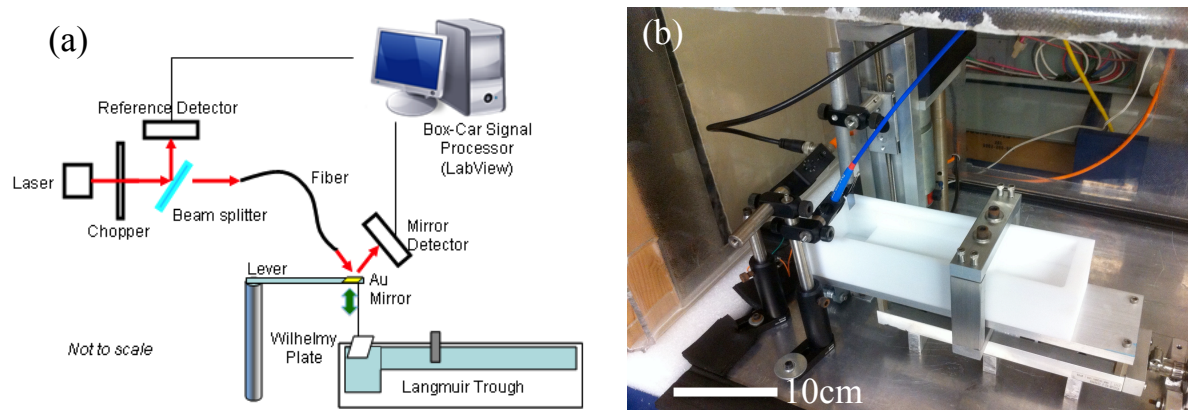


The LB trough used for this research was designed, built, and programmed in-house (Fig. 6). The trough was machined from a single piece of PTFE; it consists of a single barrier that is moved by a precision slide connected to a stepper motor. The slide is connected to a linear position sensor, which allows automation of the compressions. The surface pressure is measured using a thin spring steel leaf spring connected to a Wilhelmy plate. The deflection of the spring is measured by reflecting a frequency-modulated laser off



of a small mirror on the end of the spring; the intensity is recorded by a Si-detector. Within the range of motion of the spring under normal operational use, the detector intensity is linear with  $\Delta x$ . The laser beam is split before the mirror, and another detector records a reference intensity. The reference detector, which compensates for power drift in the laser, is used to normalize the signal from the mirror detector. The signals from both detectors are acquired using a tunable boxcar signal processor, which was written in LabView. The system allows for fast signal acquisition and efficient filtering, as well as a stable, reproducible signal, with a sensitivity of  $\sim 500\mu\text{N/m}$  over several hours.

**Figure 6:** (a) Langmuir-Blodgett trough schematic; the surface pressure,  $\Pi$ , is measured by a Wilhelmy plate connected to a lever spring and a laser system. The data is processed using a boxcar integrator written in LabView. (b) Photograph of the experimental setup in the laboratory. The trough is placed on vibration-isolation foam inside an isolation chamber.



### 3.1.3 Reactive ion etching

Reactive ion etching (RIE) is a microfabrication process used to etch a variety of industrially relevant materials (Si, SiN, SiO<sub>2</sub>, Al, Ge, etc.) [23–31]. The process utilizes a plasma to chemically and physically etch the substrate. With the correct tuning of process parameters, RIE can be used for highly anisotropic etching of silicon, with very high aspect ratios and selectivity [24,29,31]. Silicon is etched with halide anions such as F-, Br-, or Cl-. The most common gases used are SF<sub>6</sub> and CF<sub>4</sub>, which can be paired with a sidewall-passivation gas such as O<sub>2</sub> or C<sub>4</sub>F<sub>8</sub>. The plasma is created by strong oscillating electric and magnetic fields produced by an inductive coil operating at radio-frequency (RF: 13.56 MHz), usually at several hundred watts. The chuck is capacitively biased with a separate RF circuit to independently create highly directional electric fields near the substrate. This dual RF set up allows for very high plasma density, low pressure, and anisotropic etching conditions.

Etching for Si, Ge, and GaAs was done in the UCSB Nanofabrication facility using either a Panasonic E640 inductively coupled plasma (ICP) etching tool or a Plasma-Therm 770 SLR Deep reactive ion etcher (DRIE). The E640 is a standard reactive ion etch (RIE) tool with 1000W ICP power, 500 W RF substrate bias power, and high pumping speed. The 770 SLR is a dedicated Si etch tool that is designed for deep etching using the Bosch technique. This tool can also be used for standard Si and Ge etch recipes. The tools are cleaned/prepped before each etch with an oxygen plasma conditioning step for up to 20 minutes (825W ICP power, O<sub>2</sub>/Ar gas mix). Low aspect ratio structures (<10) are etched in Si and Ge using the 770 SLR via a standard single-step etch utilizing a mixture of SF<sub>6</sub>, C<sub>4</sub>F<sub>8</sub>, and Ar at 825W ICP power, with a substrate bias between 10-20W. GaAs is etched in the

Panasonic E640 using  $\text{Cl}_2$  and  $\text{N}_2$ , at 1000W ICP power and 100W bias. It should be noted that these etch tools are capable of etching other materials, such as  $\text{Al}_2\text{O}_3$ ,  $\text{HfO}_2$ ,  $\text{SiN}$ ,  $\text{SiO}_2$ ,  $\text{AlGaAs}$ ,  $\text{InGaAlAs}$ ,  $\text{InGaAsP}$ ,  $\text{GaN}$ ,  $\text{AlGaN}$ ,  $\text{GaSb}$ ,  $\text{CdZnTe}$  (CZT), and  $\text{SiC}$ , all of which have IR applications.

Higher aspect ratios ( $>10$ ) were achieved in Si by with a Bosch etch process. The Bosch process is a cycled RIE that enables control of sidewall passivation and very high etch rates ( $2\text{-}3\mu\text{m}/\text{min}$ ). Three steps, each lasting several seconds, are repeated until the desired structure is completed. First,  $\text{C}_4\text{F}_8$  is used as a deposition gas that forms a  $\text{C}_x\text{F}_y$  polymer on the sidewalls of the structure. This step is done at low plasma power and no substrate bias. The passivation layer protects the substrate from etching. Next, an  $\text{Ar}/\text{SF}_6$ , high power, high bias step is performed to directionally etch the passivation layer at the base of the substrate. The polymer layer on the sidewalls is not etched because the ions striking the surface do not have enough lateral momentum to sputter off any material. Then, a high flowrate  $\text{SF}_6$  plasma is used to directionally etch the exposed silicon substrate. The result is a nearly vertical, damage-free etch.

### 3.2 Optical characterization

Complete radiometric characterization of samples from  $\lambda=1-50\mu\text{m}$  requires careful measurement of reflection, transmission, and absorption to close the “photon balance”:

$$I_I = I_R + I_T + a, \quad (7)$$

where  $I_I$ ,  $I_R$ , and  $I_T$  represent incident, reflected, and transmitted intensities, respectively, and  $a$  is the absorption in the material. However, quantitative measurements of each term in equation (7) in an absolute (radiometric) sense is very challenging because each term may depend on the incident angle, refracted or reflected angle, sample orientation, and/or polarization. The complete picture is better described by:

$$I_I = I_{SR} + I_{DR} + I_T + I_{FS} + a, \quad (8)$$

where the SR, DR, and FS subscripts designate specular reflection, diffuse reflection, and forward scattering. Each component of equation (8) is a function of incident angle, refracted or reflected angle, sample orientation, and polarization. To fully characterize an optical sample, each component in equation (8) must be measured separately and absolutely in dedicated experimental set-ups, which are discussed in the following section.

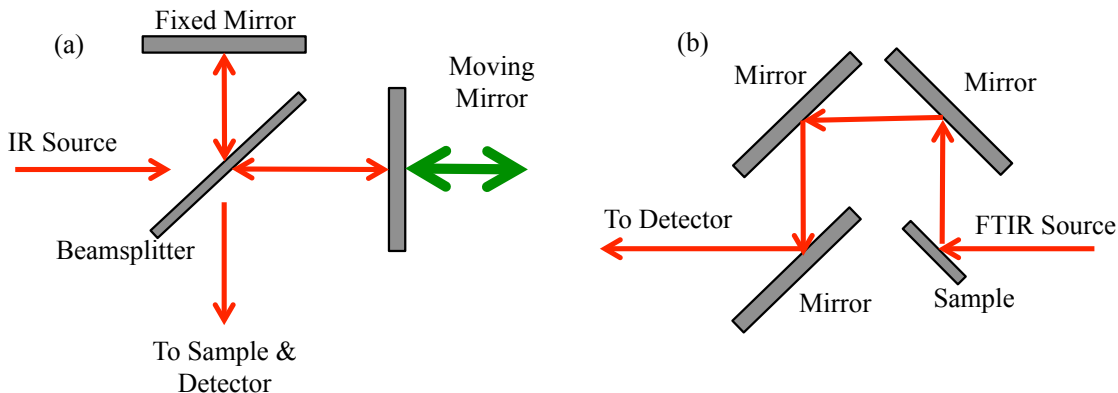
#### 3.2.1 Fourier transform infrared spectroscopy (FTIR)

Fourier transform infrared spectroscopy is a non-dispersive measurement technique to measure the transmission, absorption, or reflection of samples in the IR. It utilizes a blackbody source to generate IR light, which is collimated, and sent through a Michelson interferometer (a moving mirror, a stationary mirror, and a beamsplitter, Fig. 7a). The modulated light is then passed through the sample to a detector. The detector measures the total intensity of the light as a function of retardation (difference of path lengths between the

mirrors). This measurement, called an interferogram ( $I(\Delta d)$ ), can be converted to intensity as a function of inverse wavelength ( $I(1/\lambda)$ ) via a Fourier transform. This allows measurement of all wavelengths at the same time, which increases signal-to-noise (compared to dispersive techniques), speeds up the measurement, and allows for measurements of large bandwidths.

Measurements to  $\lambda=25\mu\text{m}$  were performed in-house with a Bruker Equinox 55 Fourier transform infrared spectrometer (FTIR). For measurements to  $200\mu\text{m}$ , samples are measured in a Nicolet Magna 850 FTIR with solid substrate beam splitter (Ge). The Bruker FTIR is used with a simple sample holder and three mirrors for normal incident transmission and specular ( $45^\circ$ ) reflection measurements (Fig. 7b). For diffuse reflectance and forward scattering measurements, a gold integrating sphere was designed and fabricated in-house. It was machined from two solid pieces of brass (Fig. 8a), sandblasted, and electrochemically coated with gold (Fig. 8b). The geometry allows for measurement of diffuse reflectance, as well as total transmission ( $I_{\text{FS}} + I_{\text{T}}$ , Figs. 8c,d).

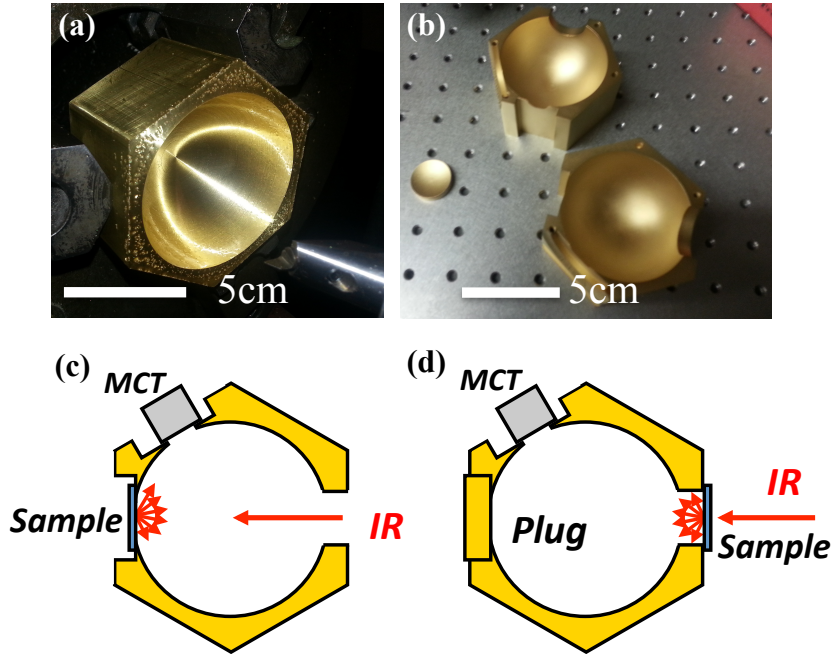
**Figure 7:** (a) Michelson interferometer used in Fourier transform infrared spectrometers for non-dispersive measurements. (b) Attachment to measure specular reflectance at  $45^\circ$ .



The sample and detector ports are machined to have a knife-edge to allow as much light to reach the detector as possible. The detector is a liquid nitrogen-cooled HgCdTe (MCT) that is sensitive from  $\lambda=1-25\mu\text{m}$ . The reference sample is evaporated Au on 600 grit

sandpaper, which has been shown in literature to have diffuse reflectance >99% for  $\lambda=2.2\text{-}23\mu\text{m}$  [32].

**Figure 8:** Integrating sphere machined from solid bronze (a), sandblasted and electrochemically coated with Au (b). (c) Diffuse reflectance and (d) forward scattering measurement geometries.



Diffuse reflectance of a sample is determined by measuring the reference (diffuse Au), no sample (blank), and sample. The diffuse reflectance ( $DR$ ) is then calculated by:

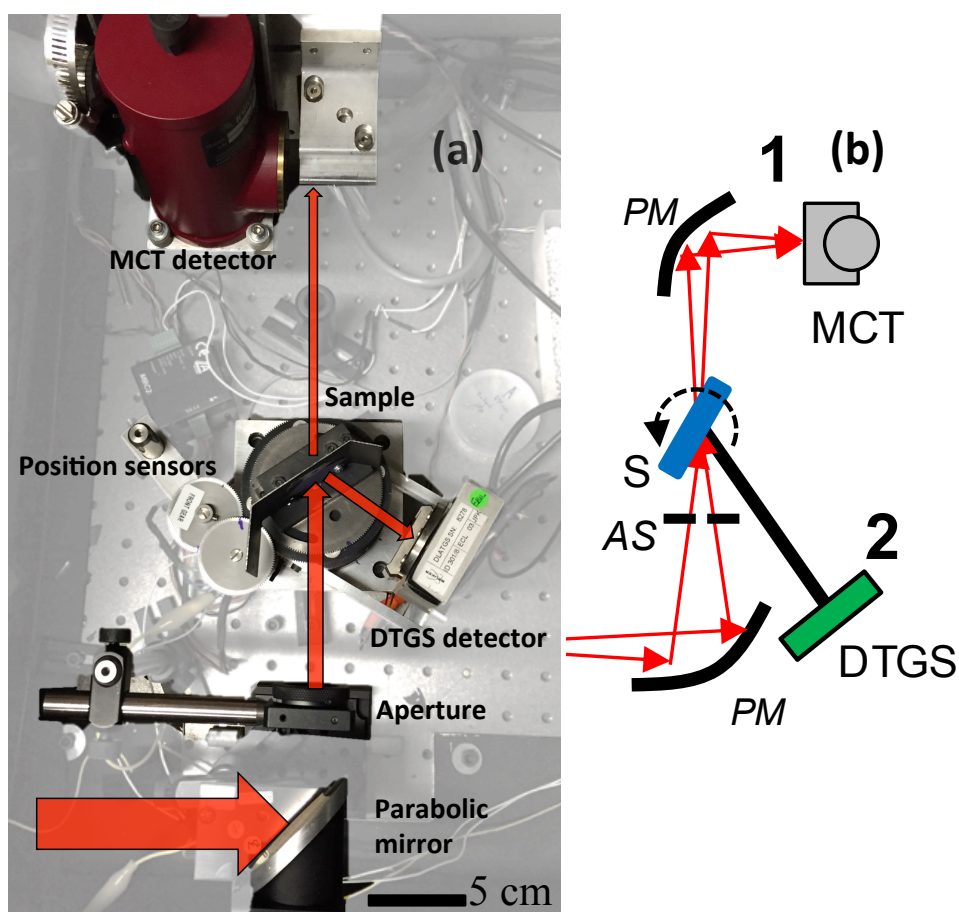
$$DR_{Sample} = \frac{R_{sample} - R_{blank}}{R_{reference} - R_{blank}}, \quad (9)$$

where  $R$  is the measured intensity. Using the integrating sphere made in-house,  $R_{blank} \sim 30\%$ .

Angle-dependent transmission and specular reflection measurements were done using a custom built  $\theta$ - $2\theta$  goniometer built to fit the Bruker FTIR. The system was designed to fit externally of the FTIR, with IR light from the interferometer diverted out of the FTIR by means of a flat mirror. The system consists of a long focal length parabolic mirror which focuses the light onto the sample, an aperture stop which limits the solid angle of the incoming beam (AS, Fig 9b), and two detectors (DTGS and MCT) for reflection and

transmission, respectively. The sample holder and DTGS detector are connected to rotating stepper-motor stages connected to position sensors, which can move independently, allowing for  $\theta$ - $2\theta$  measurements. Control of the calibration, detector and sample movement, and data collection were automated using LabView.

**Figure 9:** (a) Photograph and (b) schematic of the  $\theta$ - $2\theta$  goniometer built for the Bruker FTIR. The light is diverted from the interferometer into the system (large red arrow), passed through an aperture stop (b, AS), and focused on the sample. A DTGS detector collects reflected light, and a MCT detector collects transmitted light. The system can measure light incident on the sample from 0-70° from normal.



### 3.3. References

- [1] U. C. Fischer and H.P. Zingsheim, "Submicroscopic pattern replication with visible light," *J. Vac. Sci. Technol.* **19**, 881 (1981).
- [2] J. Hulteen and R. Van Duyne, "Nanosphere lithography: a materials general fabrication process for periodic particle array surfaces," *J. Vac. Sci. Technol. A* **13**, 1553 (1995).
- [3] H. W. Deckman, "Natural lithography," *Appl. Phys. Lett.* **41**, 377 (1982).
- [4] G. Zhang, D. Wang, and H. Möhwald, "Patterning microsphere surfaces by templating colloidal crystals," *Nano Lett.* **5**, 143 (2005).
- [5] S. Greulich-Weber and H. Marsmann, "From Nanosize Silica Spheres to Three-Dimensional Colloidal Crystals," *Ordered Porous Nanostructures and Applications*, 109–142, (Springer, 2005).
- [6] B. M. Bardosova, M. E. Pemble, I. M. Povey, R. H. Tredgold, and M. Bardosova, "The langmuir-blodgett approach to making colloidal photonic crystals from silica spheres," *Adv. Mater.* **22**, 3104 (2010).
- [7] W. Stöber, A. Fink, and E. Bohn, "Controlled growth of monodisperse silica spheres in the micron size range," *J. Colloid Interface Sci.* **26**, 62 (1968).
- [8] G. Bogush, M. Tracy, and C. Z. Iv, "Preparation of monodisperse silica particles: control of size and mass fraction," *J. Non. Cryst. Solids* **104**, 95 (1988).
- [9] A. van Blaaderen and A. Vrij, "Synthesis and Characterization of Monodisperse colloidal organo-silica spheres," *J. Colloid Interface Sci.* **156**, 1 (1993).
- [10] H. Giesche, "Synthesis of monodispersed silica powders I. Particle properties and reaction kinetics," *J. Eur. Ceram. Soc.* **14**, 189 (1994).



- [11]H. Giesche and K. Osseo-Asare, "Silica," *Fine Particles: Synthesis, Characterization, and Mechanisms of Growth. Surfactant Science* **92**, 126 (Taylor and Francis, 2000).
- [12]K. Nozawa, H. Gailhanou, L. Raison, P. Panizza, H. Ushiki, E. Sellier, J. P. Delville, and M. H. Delville, "Smart control of monodisperse Stöber silica particles: effect of reactant addition rate on growth process," *Langmuir* **21**, 1516 (2005).
- [13]K. S. Chou and C. Chen, "The critical conditions for secondary nucleation of silica colloids in a batch Stöber growth process," *Ceram. Int.* **34**, 1623 (2008).
- [14]K. Do Kim and H. T. Kim, "New Process for the Preparation of Monodispersed , Spherical Silica Particles," *J. Am. Ceram. Soc.* **85**, 1107 (2002).
- [15]W. Cheong and Y. Seo, "Allyltrimethoxysilane as the reagent of double bond introduction to porous silica for preparation of a chiral stationary phase in comparison with allyltriethoxysilane" *Bull. Korean Chem. Soc* **27**, 1059 (2006).
- [16]S. Reculosa, P. Massé, and S. Ravaine, "Three-dimensional colloidal crystals with a well-defined architecture," *J. Colloid Interface Sci.* **279**, 471 (2004).
- [17]F. Lora Gonzalez, M. Gordon, and F. Gonzalez, "Bio-inspired, sub-wavelength surface structures for ultra-broadband, omni-directional anti-reflection in the mid and far IR," *Opt. Express* **22**, 12808 (2014).
- [18]A. Gil and F. Guitián, "Formation of 2D colloidal crystals by the Langmuir-Blodgett technique monitored in situ by Brewster angle microscopy," *J. Colloid Interface Sci.* **307**, 304 (2007).
- [19]S. Reculosa and S. Ravaine, "Synthesis of colloidal crystals of controllable thickness through the Langmuir-Blodgett technique," *Chem. Mater.* **23**, 598 (2003).

- [20] M. Bardosova, P. Hodge, V. Smatko, R.H. Tredgold, and D. Whitehead, "A new method of forming synthetic opals," *Acta Phys. Slovaca* **54**, 409 (2004).
- [21] S. Reculosa, R. Perrier-Cornet, B. Agricole, V. Heroguez, T. Buffeteau, and S. Ravaine, "Langmuir-Blodgett films of micron-sized organic and inorganic colloids," *Phys. Chem. Chem. Phys.* **9**, 6385 (2007).
- [22] A. A. Chabanov, Y. Jun, and D. J. Norris, "Elimination of cracks in self-assembled photonic band gap crystals," *Appl. Phys. Lett.* **84**, 3573 (2004).
- [23] M. K. Connors, L. J. Missaggia, W. S. Spencer, and G. W. Turner, "Inductively coupled plasma reactive ion etching of GaAs wafer pieces with enhanced device yield," *J. Vac. Sci. Technol. B* **32**, 021207 (2014).
- [24] C. Wongwanitwattana, V. A. Shah, M. Myronov, E. H. C. Parker, T. Whall, and D. R. Leadley, "Precision plasma etching of Si, Ge, and Ge:P by SF<sub>6</sub> with added O<sub>2</sub>," *J. Vac. Sci. Technol. A* **32**, 031302 (2014).
- [25] K. Taek Sung, "Comparison of Germanium and Silicon Dry Etching by Using Inductively Coupled BCl<sub>3</sub> Plasma," *J. Korean Phys. Soc.* **56**, 59 (2010).
- [26] K. H. Shim, Y. H. Kil, H. D. Yang, B. K. Park, J. H. Yang, S. Kang, T. S. Jeong, and T. S. Kim, "Characteristics of germanium dry etching using inductively coupled SF<sub>6</sub> plasma," *Mater. Sci. Semicond. Process* **15**, 364 (2012).
- [27] K. Shim, H. Yang, Y. Kil, and H. Yang, "Nanoscale dry etching of germanium by using inductively coupled CF<sub>4</sub> plasma," *J. Korean Phys. Soc.* **54**, 2290 (2009).
- [28] H. Lee, K. Chung, and J. Yu, "Selective Etching of Thick Si<sub>3</sub>N<sub>4</sub>, SiO<sub>2</sub> and Si by Using CF<sub>4</sub>/O<sub>2</sub> and C<sub>2</sub>F<sub>6</sub> Gases with or without O<sub>2</sub> or Ar Addition," *J. Korean Phys. Soc.* **54**, 1816 (2009).

- [29]D. Vrtacnik, D. Resnik, U. Aljancic, M. Mozek, and S. Amon, "Silicon dry etching profile control by RIE at room temperature for MEMS applications," *Proc. of SPIE* **6037**, 603720–1 (2005).
- [30]M.S. Castro, S. Barnola, and B. Glück, "Selective and Anisotropic Dry Etching of Ge over Si," *J. Integr. Circuits and Systems* **8**, 104 (2013).
- [31]G. S. Oehrlein, T. D. Bestwick, and P. L. Jones, "Selective Dry Etching of Germanium with Respect to Silicon and Vice Versa," *J. Electrochem. Soc.* **138**, 1443 (1991).
- [32]D. B. Nash, "Mid-infrared reflectance spectra (2.3-22 $\mu$ m) of sulfur, gold, KBr, MgO, and halon.," *Appl. Opt.* **25**, 2427 (1986).

## Chapter 4

---

### **Importance of diffuse scattering phenomena in moth-eye arrays for broadband IR applications**

---

*Adapted from the Optics Letters article:*

F. Lora Gonzalez, D.E. Morse, and M.J Gordon, *Optics Letters* **39**, 13 (2014).

#### *4.1. Chapter summary*

Moth-eye arrays with varying aspect ratio and profile height were fabricated in Si using a general colloidal lithography and reactive ion etching (RIE) technique. Anti-reflective (AR) properties of the arrays were rigorously assessed from the near to far infrared ( $\lambda = 2\text{-}50\ \mu\text{m}$ ) using transmission and reflection measurements via dispersive and Fourier transform infrared spectroscopy (FTIR), and modeled using an effective medium approximation (EMA). IR transmission of low aspect ratio structures ( $\sim 2$ ) matched the EMA model, indicating that the most important factor for AR at higher wavelengths is structure height. High aspect ratio structures ( $>6$ ) were highly transmissive ( $>90\%$  of theoretical maximum) over a large bandwidth in the mid IR ( $20\text{-}50\ \mu\text{m}$ ). Specular reflectance, total transmission, and diffuse reflectance measurements indicate that moth-eye structures do not reach the theoretical maximum at near infrared (NIR) wavelengths due to diffuse reflectance and forward scattering phenomena. Ultimately, correlating optical performance with feature geometry (pitch, profile, height, etc.) over multiple length scales allows intelligent design of moth-eye structures for broadband applications.

#### *4.2. Introduction*

Infrared (IR) optical components (e.g., windows, lenses, and concentrators) are used in many venues such as thermal imaging [1,2], low temperature astronomy [3,4], and solar cells [5,6]. Materials of interest for these applications typically have high refractive indices in the IR (e.g.,  $n = 2.4$ ,  $3.42$ , and  $4.02$  for ZnSe, Si, and Ge, respectively), which leads to considerable transmission losses due to reflection [7]. For example, a single air-Si interface will reflect  $\sim 30\%$  of IR light at normal incidence in the  $\lambda = 2\text{-}50\text{+}\ \mu\text{m}$  range, leading to  $53\%$

overall transmission when multiple reflections are taken into account for a typical Si window. The reflection problem has traditionally been dealt with using destructive interference-based anti-reflective coatings (ARCs) which rely on multiple thin films with different refractive indices deposited on the surface of interest [8]. These thin film stacks are often expensive and time consuming to deposit, have limited bandwidth and acceptance angles, and need to be very thick for IR wavelengths (i.e., destructive interference occurs at  $\lambda/4$ ) [8,9]. In addition, coatings are susceptible to heating and damage from standing waves in high power applications, and they can delaminate and corrode in harsh environments [8,9].

An alternative approach to ARCs can be found in the eye of the moth [10-14], where sub- $\lambda$  protuberances on the eye surface present a smooth refractive index gradient, i.e., from  $n = 1$  in air to  $n = 1.4$  in the eye tissue, that decreases Fresnel reflection and diffraction. Since protuberances are smaller than the wavelength, the outer layer of the eye behaves as an effective medium with spatially varying refractive index that suppress reflection, making the air-eye interface essentially disappear. The moth-eye (ME) principle can be recreated, in theory, on any surface to achieve anti-reflectance over an arbitrary wavelength range if designed appropriately. In addition, sub- $\lambda$  ME arrays have several benefits over interference-based ARCs: (1) they are part of the substrate inherently, so they are mechanically robust; (2) they are not susceptible to standing wave heating because they are not based on interference; and most importantly, (3) their AR properties span larger wavelength and acceptance angle ranges [15,16]. These benefits have been leveraged heavily at visible wavelengths to create ME-based anti-glare coatings for displays and windows [12,17],

increase light collection in solar cells [5,18], and increase light extraction in light emitting diodes (LED's) [19].

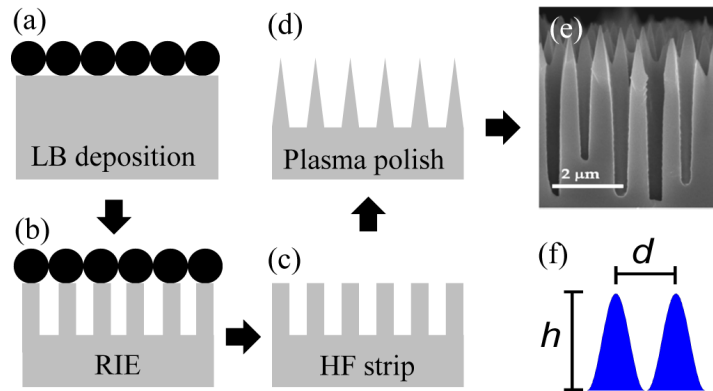
ME arrays are typically characterized with transmission and specular reflectance measurements [8] which give a good idea of optical performance. However, use of ME-ARCs in broadband IR applications faces additional challenges because feature geometry (e.g., pitch, height, aspect ratio, profile, etc.) spans multiple length scales where light-matter interactions transition from the (sub- $\lambda$ ) near field (where local geometry matters) to an effective medium with bulk-like constitutive optical properties. For such applications, theoretical predictions and performance evaluation of ME-ARCs must consider the total light balance, i.e., quantitative data on specular and diffuse transmission, reflection, scattering and absorption, to fully understand the connection between ME geometry and AR behavior. Here, we specifically highlight the importance of diffuse scattering phenomena in different ME-ARC geometries with experiment and theory, and show that seemingly 'good' AR performance in the NIR is in fact largely due to diffuse scattering that depends on ME feature size. We also show that an effective medium model and transfer matrix algorithm can be used to predict the optical performance of different ME geometries in the mid- to far-IR.

#### *4.3. Results and discussion*

ME arrays with different geometries were fabricated on undoped silicon (>3000  $\Omega\cdot\text{cm}$ , University Wafer) using a combination of colloidal lithography and reactive ion etching (RIE) pattern transfer (Fig. 1). The mask used was a closed-packed array of either 690 nm or 1  $\mu\text{m}$   $\text{SiO}_2$  particles (Bangs Lab) deposited on the Si substrate by Langmuir-Blodgett (LB) transfer [20,21]. Particles were functionalized with allyltrimethoxysilane

(ATMS, Sigma-Aldrich), suspended in chloroform/ethanol (1:1) on a water sub-phase, and dip-coated on Si by drawing the substrate vertically from the LB trough at 2 mm/s while maintaining the surface pressure in the highly compressed state (single layer HCP colloid region). Low aspect ratio structures ( $< 2$ ) were fabricated with an in-house inductively coupled plasma (ICP) RIE using an  $\text{SF}_6/\text{O}_2/\text{Ar}$  plasma at 250 W and 25 W chuck bias. High aspect ratio structures were fabricated in two steps: (a) Bosch etch in a Plasma-Therm 770 SLR RIE, achieving aspect ratios  $> 20$ , followed by (2) tapering or ‘polishing’ of the structures using an isotropic  $\text{SF}_6$  ICP etch in-house. Transmittance (normal incidence) and specular reflection ( $8^\circ$  from normal) measurements ( $2\text{-}50\ \mu\text{m}$ ) were performed in a Perkin-Elmer 983G dispersive IR spectrophotometer, and diffuse reflection and forward scattering + direct transmission measurements ( $2\text{-}22\ \mu\text{m}$ ) were done using a custom Au-coated integrating sphere in a Bruker Equinox 55 FTIR with  $\text{LN}_2$ -cooled HgCdTe (MCT) detector.

**Figure 1:** (a-d) Process flow to fabricate moth-eye arrays in Si. Colloidal  $\text{SiO}_2$  is deposited via dip coating and Langmuir-Blodgett transfer. (e) SEM image of moth-eye ARC in Si. (f) Geometrical parameters for effective medium approximation and Bruggeman model; a sinusoidal height profile was assumed.



As stated earlier, a bare Si wafer will transmit  $\sim 53\%$  of the overall incident light for  $\lambda > 2\ \mu\text{m}$  at normal incidence, accounting for multiple reflections at the wafer front and back surfaces, because the transmittance of each air-Si interface is  $\sim 70\%$ . If, however, one side of



the wafer is perfectly transmissive (anti-reflective, due the presence of an ARC on one surface), the maximal transmission will be 70%. In this work, direct transmission data were referenced to this single-side anti-reflection limit (70%) to clearly show how single-side ME-ARCs outperform a single air-Si interface. Additionally, diffuse reflectance data on ME coatings were referenced to 50 nm thick, thermally evaporated Au on 600-grit sandpaper, which has been shown previously to act as a Lambertian surface in the IR [22]. Finally, the overall photon (scattering) balance of each sample was ascertained through quantitative measurements of spectral reflection + transmission (direct + diffuse forward scattering) + diffuse backscatter.

An effective medium approximation (EMA) was used to model the optical behavior of ME arrays. The effective refractive index of the ME surface,  $n_{eff}(h,\lambda)$ , which is a function of feature depth  $h$  and  $\lambda$ , was calculated using the Bruggeman model (eqn. 1) [8-10] assuming a sinusoidal profile, as shown in Fig. 1f:

$$\frac{f}{1-f} \frac{n_{Si}^2 - n_{eff}^2}{n_{Si}^2 + 2n_{eff}^2} = \frac{n_{eff}^2 - 1}{2n_{eff}^2 + 1} \quad (1)$$

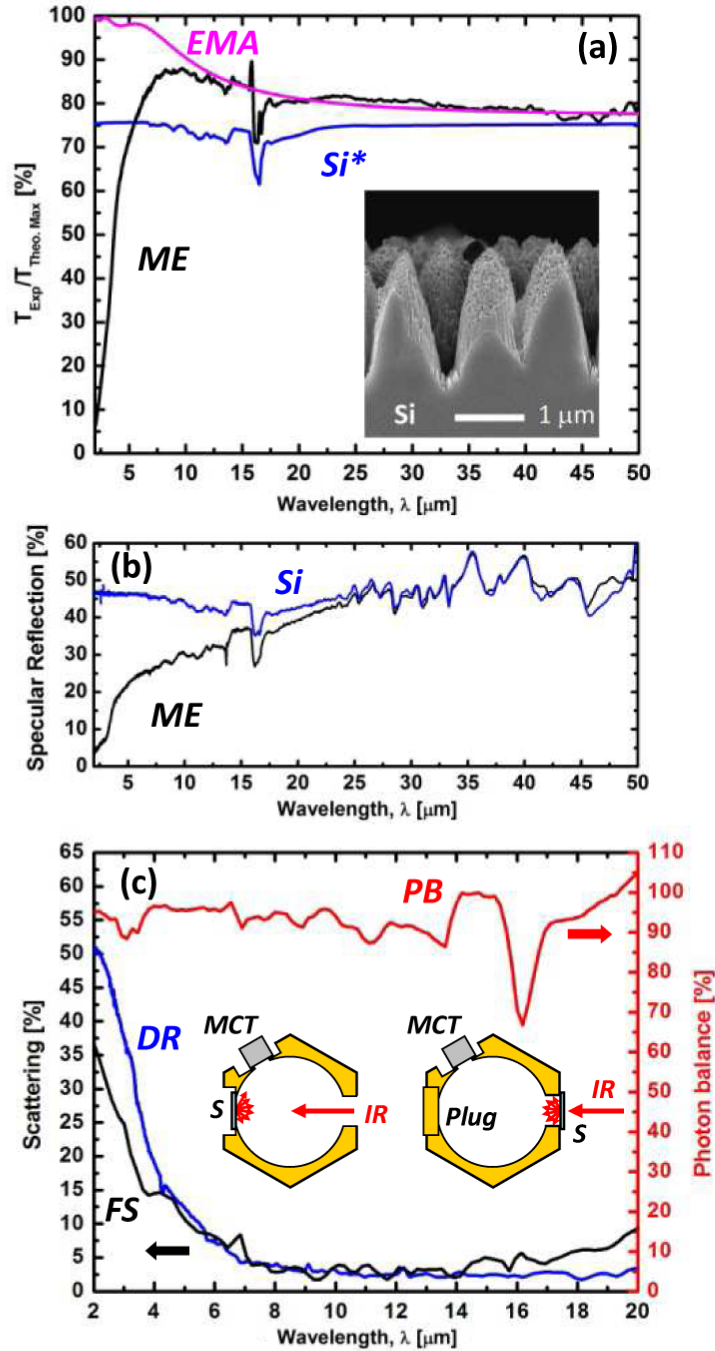
where  $f = 0.907 \left[ \frac{2}{\pi} \arccos(h) \right]^2$ .

The function  $n_{eff}$  was discretized into an equivalent ‘stack’ of 100 homogeneous layers with different refractive indices; optical properties (transmission and reflection at normal incidence) of the resulting stack were calculated using the transfer matrix algorithm for multiple interfaces [23]. Although the EMA does not explicitly depend on the feature pitch ( $d$ ), it only strictly applies to the infinite- $\lambda$  limit where the feature pitch  $d \ll \lambda$ .

Figure 2 shows transmission, specular reflection, and diffuse scattering data for a low aspect ratio ME structure compared to a bare Si wafer, along with the EMA prediction for  $h$

= 2  $\mu\text{m}$ . For  $\lambda = 8\text{-}50$   $\mu\text{m}$ , the ME structure significantly increases wafer transmission (>80% of theoretical maximum) due to overall lower reflection losses at the air-ME interface. This effect is due to the continuous vertical variation in refractive index (1.0 to 3.42) caused by surface protuberances that are ‘small’ ( $d < 2$   $\mu\text{m}$ ) compared to the wavelength - a situation which is well predicted by the EMA model in the infinite- $\lambda$  limit. The sharp dip at  $\sim 16$   $\mu\text{m}$  is due to absorption by phonons [24]. However, optical behavior of the ME is quite different below  $\lambda = 6$   $\mu\text{m}$ , where both the transmission and specular reflection drastically decrease. Panel (c) shows that this concomitant decrease is due to a sharp increase in both [diffuse] forward scattering (FS) and diffuse reflection (DR) losses as  $\lambda$  decreases. At low wavelengths, the diffuse reflectance is as high as 50%; these ‘losses’ are caused by near-field optical interactions at the level of individual protuberances which make the air-ME interface behave as a rough surface. Figure 2c also shows that the photon balance for the system closes (within  $\pm 10\%$ , ignoring absorption), i.e., all the transmitted, reflected and scattered photons can be rigorously accounted for. Moreover, these measurements demonstrate that diffuse scattering phenomena are extremely important for wavelengths  $\leq$  protuberance size, and that an observed decrease in specular reflection, by itself, is not a useful indicator of ‘good’ AR performance.

**Figure 2:** Optical behavior of low aspect ratio ( $ar \sim 2$ ) ME structures. (a) Relative transmission ( $T_{\text{exp}}/T_{\text{theo. max}}$ ) of ME compared to calculated spectra for Si wafer (blue) and the EMA model (purple). (b) Specular reflectance of ME vs. bare Si wafer (blue). (c) Diffuse reflectance (DR, blue) and forward scattering (FS, black) of ME vs. Lambertian Au surface, along with the overall photon balance (PB) of the ME. (insets) SEM image of ME structure and integrating sphere configuration for diffuse scattering measurements; S is the sample. The absorption peak at 16  $\mu\text{m}$  is due to phonons in Si, and noise above 25  $\mu\text{m}$  in panel (b) is from the detector.

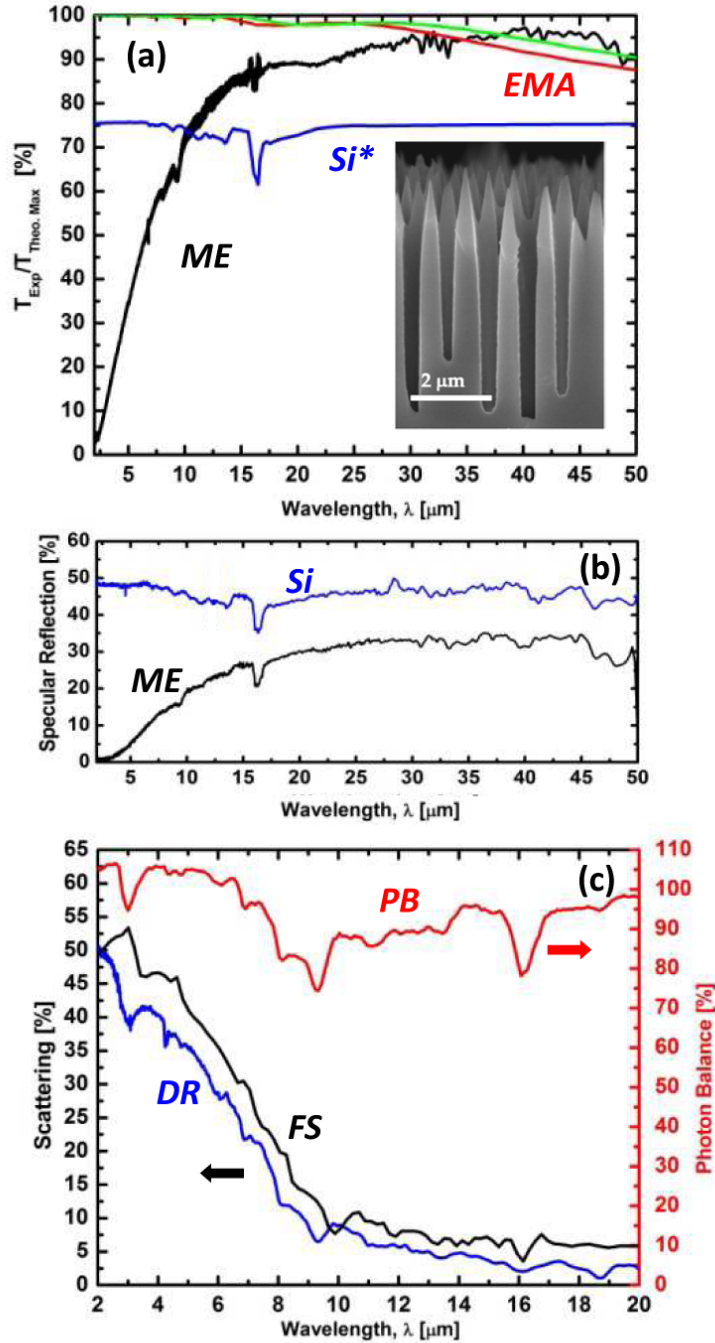


High aspect ratio ME structures (690 nm mask, 5-6  $\mu\text{m}$  Bosch etch +  $\text{SF}_6$  polish) were also investigated to see if direct transmission in the mid- and far-IR could be increased further, i.e., if high aspect ratio ME structures can provide increased specular anti-reflectivity. As seen in Fig. 3, high aspect ratio structures perform significantly better, as predicted by the EMA model for increasing  $h$  in the infinite- $\lambda$  limit. Relative direct transmission was  $> 95\%$  for  $\lambda = 35\text{-}45 \mu\text{m}$ , and  $> 90\%$  for  $\lambda > 22 \mu\text{m}$  (Fig. 3a). Again, as in the low aspect ratio case, the EMA did not match the experimental data in the low wavelength range. Direct transmission for the ME was less than a bare wafer for  $\lambda < 10 \mu\text{m}$ , and decreased drastically with  $\lambda$  in this range.

Specular reflection for the high aspect ratio case was significantly lower than the low aspect ratio sample, flattening out to 30-35% at long wavelengths. This level corresponds to the single-side specular reflectance limit for the backside of the wafer. At low wavelengths, both transmission and specular reflection went to zero, suggesting that scattering losses are again significant. Diffuse reflectance and forward scattering measurements confirm this hypothesis at low wavelengths. In addition, high aspect ratio structures showed more forward scattering and diffuse reflectance in the mid-IR, which depend on both  $d$  and  $h$ .

Typically, moth-eye arrays are regarded as 0<sup>th</sup> order diffraction gratings where the onset of scattering is attributed to 1<sup>st</sup> order diffraction, which can be predicted by the diffraction equation, and only depends on the pitch. In this work, however, we have shown that the onset of scattering at low  $\lambda$  also depends on the height (or aspect ratio), and occurs at significantly longer wavelengths than predicted by the diffraction equation, highlighting the importance of controlling quasi-order and etch variability in making moth-eye structures.

**Figure 3:** Optical behavior of high aspect ratio ( $ar \sim 6$ ) ME structures. (a) Relative transmission ( $T_{\text{exp}}/T_{\text{theo. max}}$ ) of ME compared to calculated spectra for Si wafer (blue) and the EMA model (red:  $h = 6 \mu\text{m}$ , green:  $h = 7 \mu\text{m}$ ). (b) Specular reflectance of ME vs. bare Si wafer (blue). (c) Diffuse reflectance (DR, blue) and forward scattering (FS, black) of ME vs. Lambertian Au surface, along with the overall photon balance (PB) of the ME. (inset) SEM image of ME structure. The absorption peak at  $16 \mu\text{m}$  is due to phonons in Si, and noise above  $25 \mu\text{m}$  in panel (b) is from the detector.



#### 4.4. Conclusion

In this work, we used a scalable, colloid-based lithography (LB transfer + dip coating) and pattern transfer technique to realize moth-eye arrays in Si that exhibit broadband anti-reflective behavior over the 6-50  $\mu\text{m}$  spectral range. For example, transmittance of a single air-Si interface could be increased to  $> 90\%$  of the theoretical limit for a perfect AR coating above 15  $\mu\text{m}$  with high aspect ratio ( $\sim 6$ ) ME protuberances. Quantitative measurements of transmission, specular reflection and diffuse scattering phenomena demonstrated that NIR transmittance was relatively poor (e.g.,  $<$  a bare air-Si interface) because diffuse reflectance and forward scattering were appreciable (i.e., up to 70% of the incident photons) when  $\lambda$  approached the ME feature size. Such NIR losses may be detrimental for stigmatic imaging applications, but may actually be helpful for signature management and enhanced photon recovery (extra path length + multiple reflections) in solar cells. It was also experimentally found that the most important factor for anti-reflectivity at higher wavelengths was the ME protuberance height, which is indeed predicted by the EMA. However, diffuse reflectance (DR) and forward scattering (FS) increase in the NIR and depend on both protuberance height and pitch. Overall, this work shows that performance evaluation of ME arrays, especially for broadband applications, and in the IR, must consider the total photon balance of the system, including diffuse scattering phenomena. Moreover, despite the fact that the colloid-based lithography approach leads to minor geometric variations in protuberance size and pitch, this method provides a simple and scalable way to realize ME arrays for broadband ARCs in the IR that can be extended to a variety of material platforms.

#### 4.5. References

- [1] B. F. Jones and P. Plassmann, "Digital infrared thermal imaging of human skin," *IEEE Eng. Med. Biol.* **21**, 41 (2002).
- [2] G. Muyo, A. Singh, M. Andersson, D. Huckridge, A. Wood, and A. R. Harvey, "Infrared imaging with a wavefront-coded singlet lens," *Opt. Express* **17**, 21118 (2009).
- [3] J. Lau, J. Fowler, T. Marriage, L. Page, J. Leong, E. Wishnow, R. Henry, E. Wollack, M. Halpern, D. Marsden, and G. Marden, "Millimeter-wave antireflection coating for cryogenic silicon lenses," *Appl. Opt.* **45**, 3746 (2006).
- [4] T. Kamizuka, T. Miyata, S. Sako, H. Imada, T. Nakamura, K. Asano, M. Uchiyama, K. Okada, T. Wada, T. Nakagawa, T. Onaka, and I. Sakon, "Development of high-throughput silicon lens and grism with moth-eye antireflection structure for mid-infrared astronomy," *Proc. SPIE* **8450**, 845051 (2012).
- [5] S. Thiyagu, B. Devi, and Z. Pei, "Ultra-low reflection silicon nanowire arrays for efficient solar cell applications," *Nano Res.* **4**, 1136 (2011).
- [6] K. Arpin, A. Mihi, H. Johnson, A. Baca, J. Roger, J. Lews, and P. Braun, "Multidimensional architectures for functional optical devices," *Adv. Mater.* **22**, 1084 (2010).
- [7] B. Frey, D. Leviton, and T. Madison, "Temperature-dependent refractive index of silicon and germanium," *Proc. SPIE* **6273**, 6273J (2006).
- [8] H. Raut, V. Ganesh, A. Nair, and S. Ramakrishna, "Anti-reflective coatings: A critical, in-depth review," *Energy Environ. Sci.* **4**, 3779 (2011).
- [9] S. Chattopadhyay, Y. F. Huang, Y. J. Jen, A. Ganguly, K. H. Chen, and L. C. Chen, "Anti-reflecting and photonic nanostructures," *Mater. Sci. Eng. R.* **69**, 1 (2010).

- [10] M. E. Motamedi, W. H. Southwell, and W. J. Gunning, "Antireflection surfaces in silicon using binary optics technology," *Appl. Opt.* **31**, 4371 (1992).
- [11] D. H. Ko, J. R. Tumbleston, K. J. Henderson, L. E. Euliss, J. M. DeSimone, R. Lopez, and E. T. Samulski, "Biomimetic microlens array with antireflective "moth-eye" surface," *Soft Matter* **7**, 6404 (2011).
- [12] P. I. Stavroulakis, S. A. Boden, T. Johnson, and D. M. Bagnall, "Suppression of backscattered diffraction from sub-wavelength "moth-eye" arrays," *Opt. Express* **21**, 1 (2013).
- [13] G. Xie, G. Zhang, F. Lin, J. Zhang, Z. Liu, and S. Mu, "The fabrication of subwavelength anti-reflective nanostructures using a bio-template," *Nanotechnol.* **19**, 095605 (2008).
- [14] A. R. Parker and H. E. Townley, "Biomimetics of photonic nanostructures," *Nat. Nanotechnol.* **2**, 347 (2007).
- [15] Y. F. Huang and S. Chattopadhyay, "Nanostructure surface design for broadband and angle-independent antireflection," *J. Nanophotonics* **7**, 073594 (2013).
- [16] K. C. Park, H. J. Choi, C. H. Chang, R. E. Cohen, G. H. McKinley, and G. Barbastathis, "Nanotextured silica surfaces with robust superhydrophobicity and omnidirectional broadband supertransmissivity," *ACS Nano* **6**, 3789 (2012).
- [17] A. Gombert, B. Blasi, C. Buhler, P. Nitz, J. Mick, W. Hossfeld, and M. Niggemann, "Replicated microstructures with optical functions in solar and display applications," *Proc. SPIE* **5184**, 60 (2003).
- [18] J. Zhu, Z. Yu, G. F. Burkhard, C. M. Hsu, S. T. Connor, Y. Xu, Q. Wang, M. McGehee, S. Fan, and Yi Cui, "Optical absorption enhancement in amorphous silicon nanowire and nanocone arrays," *Nano Lett.* **9**, 279 (2009).



- [19] K. Naniwae, M. Mori, T. Kondo, A. Suzuki, T. Kitano, S. Kamiyama, M. Iwaya, T. Takeuchi, and I. Akasaki, "Introduction of the moth-eye patterned sapphire substrate technology for cost-effective high-performance LEDs," *Proc. SPIE* **8641**, 86410G (2013).
- [20] M. Bardosova, M. E. Pemble, I. M. Povey, and R. H. Tredgold, "The Langmuir-Blodgett approach to making colloidal photonic crystals from silica spheres," *Adv. Mat.* **22**, 3104 (2010).
- [21] S. Reculosa, P. Masse, and S. Ravaine, "Three-dimensional colloidal crystals with a well-defined architecture," *J. Colloid Interface Sci.* **279**, 3014 (2010).
- [22] D. B. Nash, "Mid-infrared reflectance spectra (2.3-22mm) of sulfur, gold, KBr, MgO, and halon," *App. Opt.* **24**, 2427 (1986).
- [23] C. C. Katsidis and D. I. Siapkas, "Systems with coherent, partially coherent, and incoherent interference," *App. Opt.* **41**, 3978 (2002).
- [24] R. J. Collins and H. Y. Fan, "Infrared lattice absorption bands in germanium, silicon, and diamond," *Phys. Rev.* **93**, 674 (1954).

## Chapter 5

---

### **Bio-inspired, sub-wavelength surface structures for ultra-broadband, omni-directional anti-reflection in the mid and far IR**

---

*Adapted from the Optics Express article:*

F. Lora Gonzalez and M.J Gordon, *Optics Express* **22**, 12808 (2014).

### *5.1. Chapter summary*

Quasi-ordered moth-eye arrays were fabricated in Si using a colloidal lithography method to achieve highly efficient, omni-directional transmission of mid and far infrared (IR) radiation. The effect of structure height and aspect ratio on transmittance and scattering was explored experimentally and modeled quantitatively using effective medium theory. The highest aspect ratio structures (AR = 9.4) achieved peak transmittance of 98%, with >85% transmission for  $\lambda = 7\text{-}30\ \mu\text{m}$ . A detailed photon balance was constructed by measuring transmission, forward scattering, specular reflection and diffuse reflection to quantify optical losses due to near-field effects. In addition, angle-dependent transmission measurements showed that moth-eye structures provide superior anti-reflective properties compared to unstructured interfaces over a wide angular range (0-60° incidence). The colloidal lithography method presented here is scalable and substrate-independent, providing a general approach to realize moth-eye structures and anti-reflection in many IR-compatible material systems.

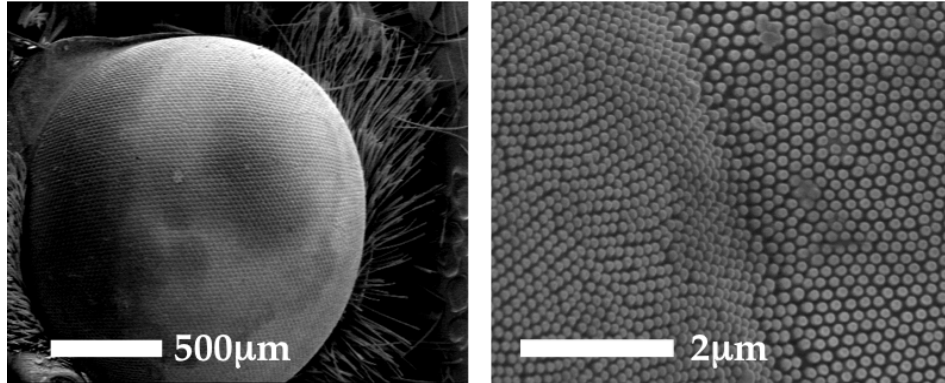
### *5.2. Introduction*

Anti-reflective coatings (ARCs) are technologically important in optical and energy applications involving infrared (IR) radiation such as low temperature astronomy [1,2], thermal imaging [3], night vision, IR sensors/lasers [4,5], and multi-junction solar cells [6]. Unfortunately, many of the materials used in these venues have high refractive indices (e.g., Si = 3.42, Ge = 4.02, and III-V semiconductors = 3.5-6) which lead to large reflection losses. For example, a Si or Ge window will reflect ~47% or 54% of the incident IR light at normal incidence, respectively, as predicted by the Fresnel equations [7]. Traditional ARCs

based on multiple thin dielectric layers deposited on the interface of interest can achieve high transmission (>99%) over limited wavelength ranges. However, interference-based ARCs are often expensive and complex to make, they have relatively narrow bandwidths (e.g., transmission >98% from 3-5  $\mu\text{m}$  with an attenuating effect at higher  $\lambda$ , frequently becoming worse than the native substrate itself), transmission is very angle dependent, and thermal stresses from standing waves within the dielectric film stack can delaminate or destroy the coating in high power situations [8,9].

An alternative method to reduce reflection is to make an interface effectively ‘disappear’ by creating a smooth variation in refractive index between two media (i.e., constructing a graded index interface). When the graded index profile is on the same length scale as the wavelength of light, Fresnel reflection can be suppressed [10]. In the eye of the moth [Fig. 1], this effect is achieved by tissue protuberances with a sinusoidal height profile that reduce reflection in the visible and NIR. In addition, the quasi-ordered nature of the protuberance array suppresses diffraction and camouflages the moth from predators [11]. The moth-eye (ME) principle, in theory, can be used with any material platform to achieve the same effect by scaling the pitch and size of protuberances for the wavelength range of interest. Because the optical response of ME arrays is not based on interference, they avoid the aforementioned issues associated with traditional ARCs; in addition, from a fundamental point of view, they are better suited for both broadband [12–14] and omni-directional (angle-independent) applications [13].

**Figure 1:** SEM images of a moth-eye showing the hexagonally-packed, quasi-ordered sinusoidal protuberances that give the moth eye its anti-reflective behavior.



The optical response of ME structures involves light-matter interactions that span several length scales, from near-field contributions at small wavelengths, to an effective medium with bulk-like constitutive optical properties at larger wavelengths. As such, optical experiments that quantitatively measure contributions from both Fresnel and Lambertian transmission and reflection are crucial to determine and understand the optical behavior of ME structures. We have taken this approach here: all components of the ‘photon balance’ (i.e., direct transmission, direct reflectance, forward diffuse scattering and diffuse backscattering) have been quantitatively measured to understand the importance of different optical phenomena over various wavelength ranges [12].

Specifically, in this work, we demonstrate a facile and scalable method to realize moth eye-based anti-reflective films in Si which have highly efficient, broadband and omnidirectional response in the mid- and far-IR spectral regions. The overall ‘photon balance’ was quantitatively evaluated to understand the importance of various near- and far-field scattering phenomena. The optical response of ME films were also quantitatively modeled using effective medium theory in the infinite wavelength limit. Ultimately, it was experimentally demonstrated that transmission and reflection at short wavelengths was

governed by diffuse scattering phenomena, while long wavelength optical behavior depended critically on ME feature height.

### *5.3. Experimental methods and theoretical calculations*

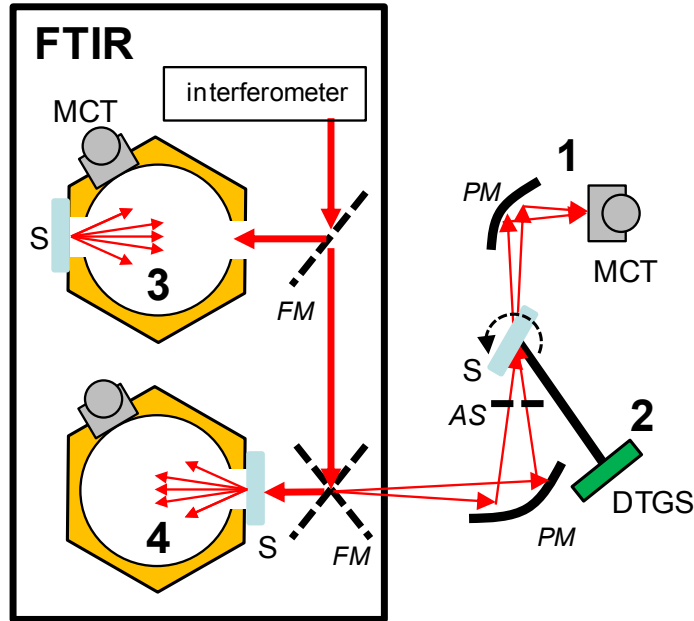
#### *5.3.1. Moth-eye fabrication*

Moth-eye structures in Si were fabricated using a colloidal lithography method outlined elsewhere [12], and briefly summarized below. The method is general and can be easily adapted to other substrates such as Ge, ZnSe, and GaAs. Monodisperse silica colloids (320 nm) were functionalized with allyltrimethoxysilane (ATMS, Sigma-Aldrich, 97%) in the presence of acetic acid and water in ethanol (pH 5.5), washed 3x in ethanol, and re-dispersed in 4:1 ethanol:chloroform. The suspension was deposited on undoped Si (225  $\mu\text{m}$  thick, 3000  $\Omega\cdot\text{m}$ , University Wafer) via dip coating using a Langmuir-Blodgett trough with constant surface pressure of  $\sim 8$  mN/m. Depending on the dip coating speed, surface coverage could be controlled with grain sizes of 10-200 $\mu\text{m}^2$ , which mimic the mosaic patterns on the moth eye seen in Fig. 1. The colloidal pattern was transferred into Si via a two step reactive ion etch (RIE) process: (1) Bosch-RIE (PlasmaTherm 770 DRIE) using  $\text{SF}_6/\text{C}_4\text{F}_8/\text{Ar}$  (825W, 9W bias, 3-cycle etch) for high-aspect ratio anisotropic etching, followed by (2) a polish and tapering step using  $\text{SF}_6/\text{Ar}$  (380W, 30W bias) in a home-built ICP-RIE. The samples were cleaned between etches in HF to remove the silica mask, and finally cleaned in Piranha and HF. Using this two-step approach, the total height and taper of the final ME structures could be controlled.

### 5.3.2. Optical characterization

Mid infrared (MIR: 2-20 $\mu\text{m}$ ) measurements were done using a Bruker Equinox-55 FTIR with LN<sub>2</sub>-cooled HgCdTe (MCT) detector for transmission [Fig. 2, configuration #1] and a La-DTGS (La-doped deuterated triglycine sulfate) detector for reflection [Fig. 2, configuration #2, 8° from normal]. Far IR (FIR: 20-50 $\mu\text{m}$ ) transmission measurements were taken using a Nicolet Magna 850 FTIR with DTGS detector. Diffuse reflectance and forward scattering were measured using a custom-built Au-coated integrating sphere fabricated for the Bruker FTIR [*cf.* Fig. 2, configurations #3 and #4, respectively], as outlined in a previous paper [12]. The specular and diffuse reflectance measurements were referenced to a 100 nm Au-coated Si wafer and 100 nm Au-coated 600 grit sandpaper, respectively [15]. Angular transmission data were collected using a custom-built rotary stage attachment on the Bruker FTIR [*cf.* Fig. 2, configuration #1]; a parabolic mirror with aperture stop focused light on the sample (8° solid angle), and transmitted light was collected with another parabolic mirror attached to an LN<sub>2</sub>-cooled MCT detector.

**Figure 2:** Experimental configuration for transmission, reflection, and diffuse scattering measurements. Configuration 1: direct and angle-dependent transmission, 2: specular reflection at  $8^\circ$  from normal incidence, 3: diffuse reflectance, and 4: forward scattering. S = sample, MCT = HgCdTe detector, DTGS = La-doped deuterated triglycine sulfate detector, FM = flip mirror, PM = parabolic mirror, and AS = aperture stop. Schematic is not to scale.



Reflection and transmission of light at an abrupt interface is described by the Fresnel equations, which predict  $\sim 70\%$  transmission of IR light at normal incidence for a single air-Si interface. Since an actual wafer has two interfaces, multiple (internal) reflections lower the overall transmission to  $\sim 53\%$  at normal incidence. If an ARC or ME array is placed on one side of the wafer, the overall transmission increases, but  $\sim 30\%$  reflection from the (unstructured) back surface of the wafer still occurs; in this ‘single-side limit’, the overall transmission of the two-sided real system will be  $\sim 70\%$  (i.e., one perfect anti-reflective surface and one Si-air interface). In the following sections, transmission data for ME structures are presented on both an absolute and relative basis. For the latter, transmission data were normalized by the theoretical single-side limit of  $\sim 70\%$ , which was calculated using the wavelength-dependent complex refractive index and the substrate thickness



(225 $\mu\text{m}$ ) to account for absorption [7,16]. Given this frame of reference, a double-sided, bare Si wafer will have a normalized transmittance of  $\sim 0.53/0.7 = \sim 76\%$ .

### 5.3.3. Effective medium calculations

A 2D effective medium approximation (EMA) was used to calculate the optical behavior of ME arrays in the infinite wavelength limit ( $d, h \ll \lambda$ , where  $d$  = feature pitch and  $h$  = feature height; see Fig. 3(a) inset), as outlined elsewhere [12]. Briefly, an effective refractive index,  $n_{eff}(\lambda, h)$ , is calculated for a given feature shape using the Bruggeman model [8-10]:

$$\frac{f}{1-f} \frac{n_{Si}^2 - n_{eff}^2}{n_{Si}^2 + 2n_{eff}^2} = \frac{n_{eff}^2 - 1}{2n_{eff}^2 + 1} \quad (1)$$

where  $f = 0.907 \left[ \frac{2}{\pi} \arccos(h) \right]^2$  is the shape factor for a sinusoidal height profile.  $n_{eff}(\lambda, h)$  is then discretized into  $N=100$  homogenous layers with different refractive indices and solved as a stack of dielectrics using the transfer matrix method [16]. In the model, hexagonal close packing of features was assumed (i.e., circular bases covering 90.7% of the surface). Since  $n_{eff}$  for each layer depends only on the overall feature shape (sinusoidal, cone, etc.) and layer height, EMA predictions are not explicitly affected by the pitch  $d$ . The substrate thickness (225  $\mu\text{m}$ ) and its absorption were taken into account in all EMA calculations by way of the wavelength-dependent complex refractive index [7,16].

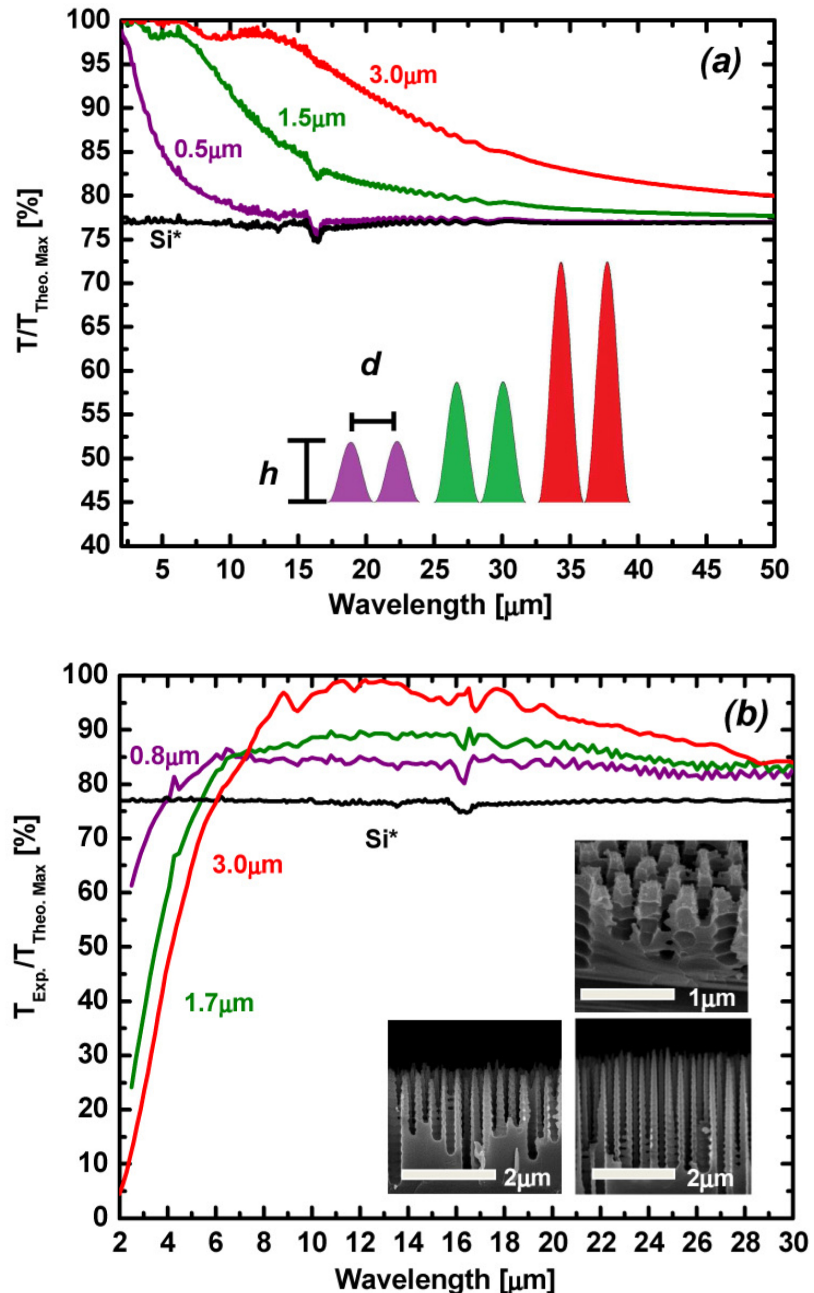
## 5.4. Results and analysis

### 5.4.1. Effect of structure height and aspect ratio

The EMA predicts that film transmission is strongly correlated with protuberance height in the infinite wavelength limit [Fig. 3(a)]. In practice, this situation requires that the colloid mask is small compared to the wavelength and that the aspect ratio of surface features be relatively large ( $AR > 1$ ). Figure 3(b) shows experimental results for three ME structures with increasing aspect ratio (2.8→5.2→9.4), fabricated using a 320 nm colloidal mask.

As predicted by the EMA and seen experimentally, transmission increases with increasing feature height for  $\lambda > 6\mu\text{m}$ . The maximum measured (normalized) transmission was 86% ( $\lambda = 6.2\ \mu\text{m}$ ), 90% ( $\lambda = 12\ \mu\text{m}$ ), and >98% ( $\lambda = 13\mu\text{m}$ ) for feature heights of 800 nm, 1.7  $\mu\text{m}$  and 3  $\mu\text{m}$ , respectively, whereas, the unstructured Si wafer is 76%. At longer wavelengths, the anti-reflective properties of the ME generally decay because the feature height becomes negligible compared to the wavelength. At short wavelengths, the transmission drops drastically because of the opposite effect: feature size is comparable to the wavelength and near-field interactions become important in the form of diffuse reflectance (DR) and forward scattering (FS). The onset of near-field losses is also strongly correlated with feature height, which is not predicted by the diffraction equation (see section 2.2); the three ME structures become more transmissive than bare Si at  $\lambda = 4, 5.4,$  and  $6\ \mu\text{m}$ , respectively, in order of increasing aspect ratio. It has also been previously shown that larger mask sizes significantly increase scattering in the NIR region [12], further suggesting that aspect ratio is the most important control parameter to maximize transmission and simultaneously mitigate scattering losses.

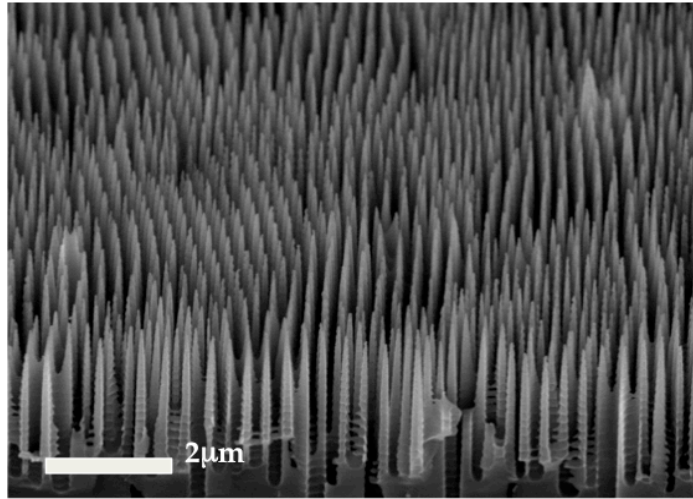
**Figure 3:** (a) Relative transmission spectra of Si moth-eye arrays with different feature heights ( $h = 0.5 \mu\text{m}$  (purple),  $1.5 \mu\text{m}$  (green) and  $3.0 \mu\text{m}$  (red)), calculated with the effective medium approximation (EMA). The transmission increase in the mid- and far-IR is strongly dependent on the feature height. (b) Relative transmission spectra measured for Si moth-eye arrays fabricated with feature heights of  $0.8 \mu\text{m}$  (purple, aspect ratio  $AR=2.8$ ),  $1.7 \mu\text{m}$  (green,  $AR=5.2$ ) and  $3.0 \mu\text{m}$  (red,  $AR=9.4$ ). The increase in transmission in the mid-IR qualitatively follows the trend predicted by the EMA. (insets) SEM images of the moth-eye arrays. Note: the black curve (Si\*) in each panel is for an unstructured Si wafer surface, and data are normalized by the theoretical single-side transmission limit of 70%.



#### 5.4.2. Optical characterization

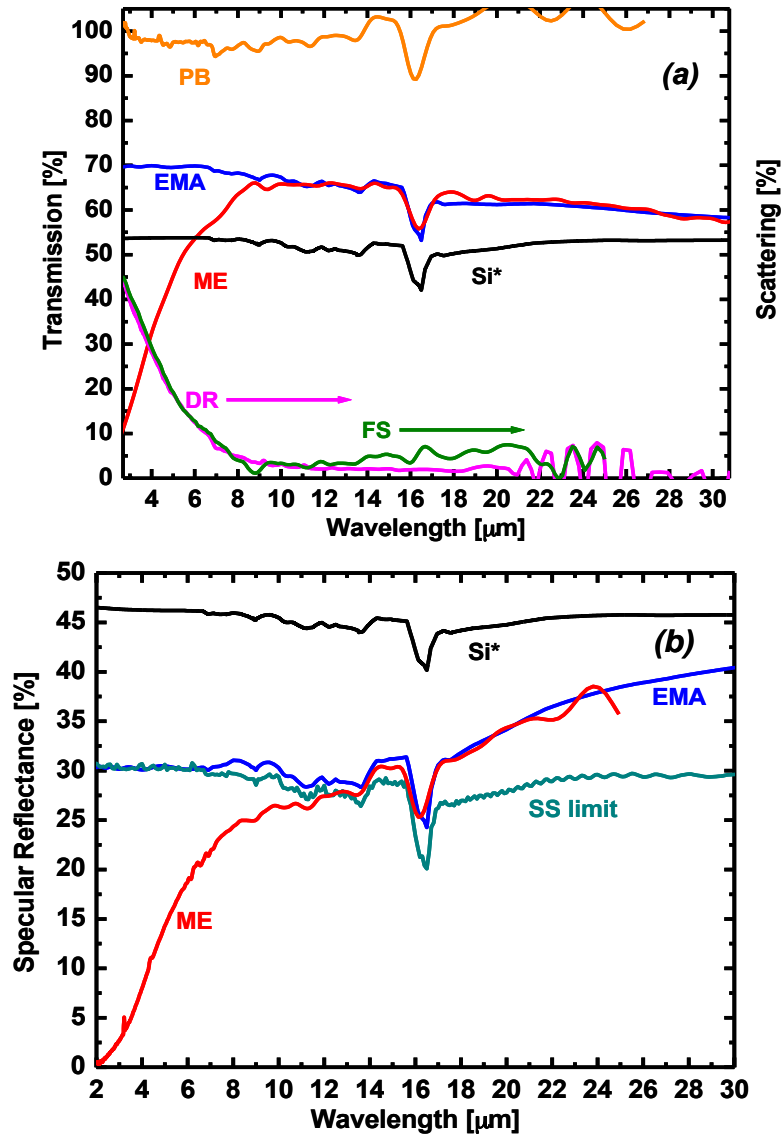
As mentioned earlier, measuring the ‘photon balance’ of ME arrays is necessary to determine the optical efficiency of the anti-reflective treatment and understand the relative contributions of direct transmission, specular reflection, diffuse reflection (DR) and forward scattering (FS) phenomena in different wavelength ranges. These measurements were undertaken for the highest aspect ratio sample [Fig. 4, AR=9.4], as detailed in Fig. 5(a). The transmission of this sample calculated using the EMA is shown in blue, along with the Fresnel prediction for a bare Si wafer (Si\*, black); the peak at  $\sim 16 \mu\text{m}$  is due to absorption by phonons [17]. The EMA model predicts that there should be a transmission increase of 5-17% for the 2-30  $\mu\text{m}$  range due to the moth-eye effect at the front interface. In addition, the EMA quantitatively describes ME transmission for  $\lambda > 10 \mu\text{m}$  where the infinite wavelength assumption holds. In this range, contributions from scattering (DR and FS) are negligible. However, as  $\lambda \rightarrow d$ , diffuse scattering phenomena become more pronounced and transmission eventually drops to 10% at  $\lambda = 2 \mu\text{m}$ .

**Figure 4:** SEM image of aspect ratio 9.4 moth-eye structure in Si fabricated with a 320 nm mask. Feature height is approximately 3 $\mu\text{m}$ . Sidewall scalloping at the bases of the features is due to the Bosch etch process.



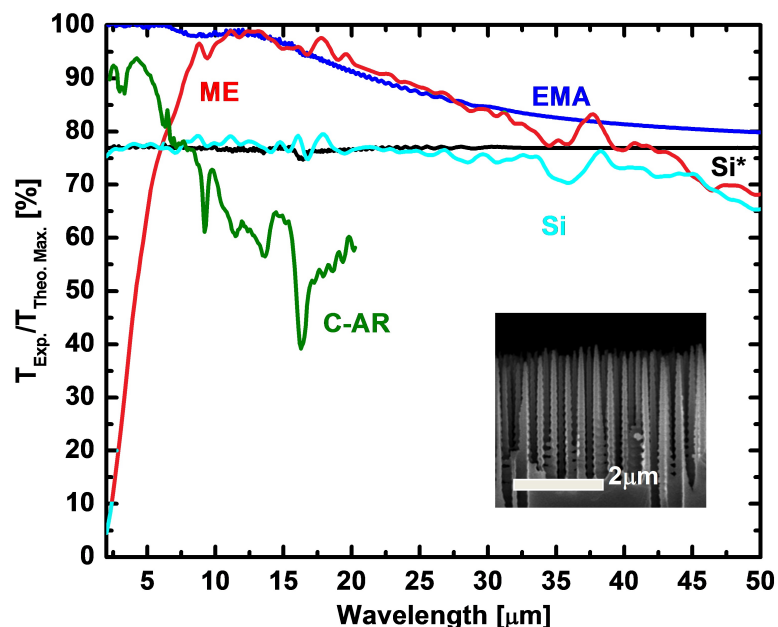
The measured specular reflection from the ME sample, along with the single-side anti-reflectance limit, EMA for the ME, and Fresnel prediction for a bare Si wafer are shown in Fig. 5(b). The SS limit represents a perfect anti-reflective coating ( $T = 100\%$ ) on the front side of the wafer only (i.e., back side reflection still occurs). It is important to point out that the seemingly ‘excellent’ low reflectance behavior of the ME below  $\lambda = 13 \mu\text{m}$  - lower than a perfect single-side coating - is due to diffuse scattering (DR and FS) rather than *inherent* anti-reflectance due to a graded index profile. This data shows that every component of the photon balance must be measured to differentiate the moth-eye effect from other scattering phenomena. As seen earlier, the EMA quantitatively predicts ME behavior in spectral regions where the infinite wavelength assumption is valid ( $\lambda > 10 \mu\text{m}$  for the present case).

**Figure 5:**(a) As-measured transmission (ME, red), diffuse reflectance (DR, purple), forward scattering (FS, green), and photon balance (PB, orange) for the high aspect ratio (AR=9.4) Si moth-eye structures shown in Fig. 4. Calculated transmission of the Si moth-eye structure (EMA, blue) and a bare Si wafer (Si\*, black) are also shown. The EMA quantitatively predicts ME transmittance when the infinite wavelength limit is valid ( $\lambda > 10 \mu\text{m}$ ). (b) As-measured specular reflectance (ME, red) and calculated reflectance (EMA, blue) of the ME structure. The single-side perfect anti-reflective coating (SS limit, teal) and bare Si wafer (Si\*, black) are also shown. The extremely low specular reflectance of the ME is due to DR and FS scattering losses rather than inherent anti-reflectivity due to a graded index profile.



To compare the synthesized ME samples with traditional ARC technology, a commercial Si window with interference-based coating ( $\lambda = 3\text{-}5\mu\text{m}$  design spec., Edmund Optics) on one side was tested in the same experimental setup. Figure 6 shows a comparison between the commercial coating (c-AR) and the aspect ratio 9.4 ME sample. The coated window has a maximum measured transmittance of 95% at  $4.5\mu\text{m}$ , and averages  $\sim 92\%$  from  $2\text{-}5\mu\text{m}$ . For  $\lambda > 8\mu\text{m}$ , the transmission is significantly lower than that of bare Si. This behavior is typical of interference-based coatings because constructive interference can occur at wavelengths far from the design range. In contrast, the ME sample has transmittance higher than bare Si for  $\lambda = 6\text{-}45\mu\text{m}$ ,  $T > 90\%$  for  $7.5\text{-}23\mu\text{m}$ ,  $> 95\%$  for  $9\text{-}18\mu\text{m}$ , and  $> 98\%$  at  $13\mu\text{m}$ . In short, the ME sample has more broadband anti-reflective response and significantly higher peak transmittance compared to typical interference-based ARCs for Si.

**Figure 6:** Relative transmission of high aspect ratio ME structures (red) and a commercial, interference-based anti-reflective coating on Si (C-AR, green) for  $3\text{-}5\mu\text{m}$ . Calculated (Si\*, black) and measured (Si, cyan) spectra for a bare Si wafer is also shown. The commercial ARC achieves a peak transmission of  $\sim 95\%$ , while the ME structure has a peak transmission of  $\sim 98\%$ . (inset) Cross-sectional SEM image of the moth-eye array.

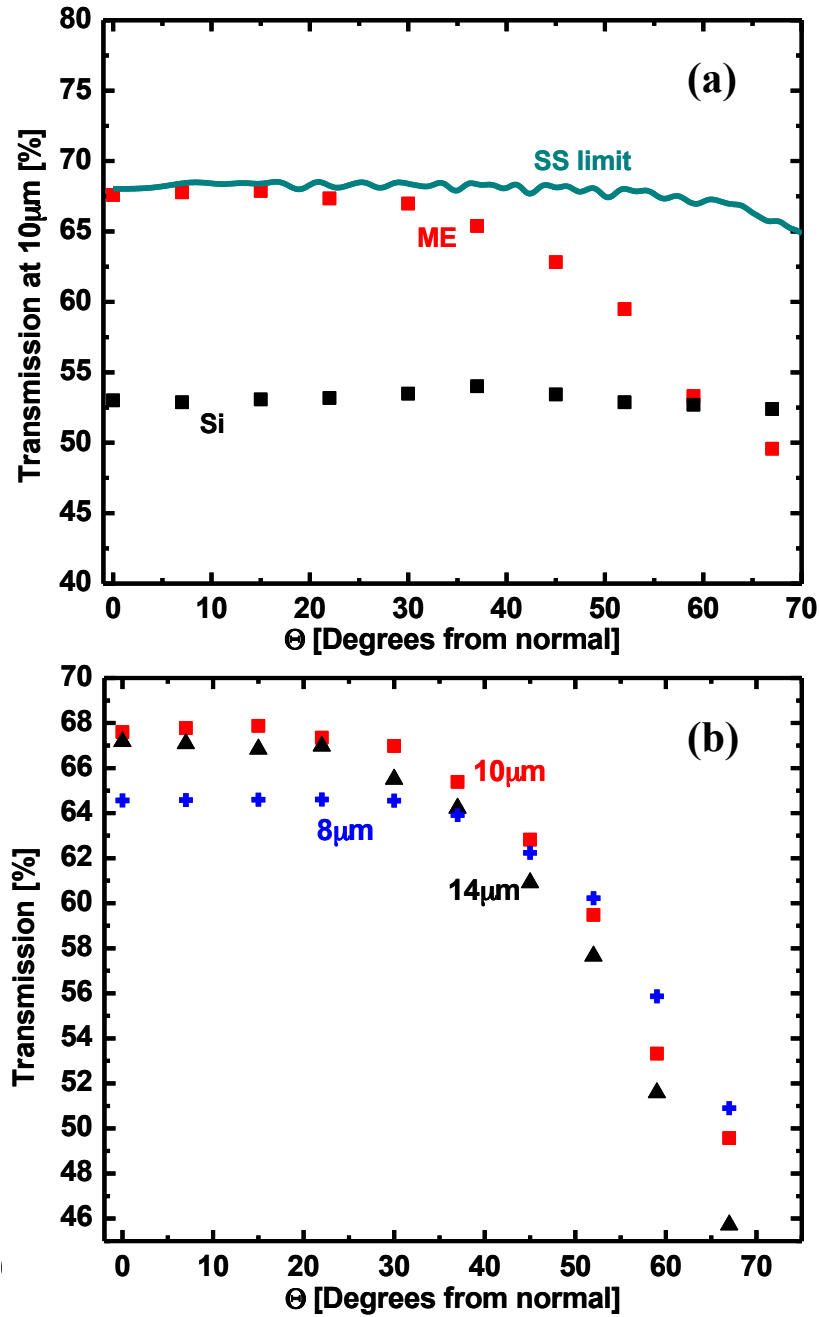


#### 5.4.3. Angular response of moth-eye structures

Different illumination geometries are sometimes encountered in IR detection and imaging applications; as such, surface coatings with omni-directional anti-reflectivity are very desirable. Figure 7(a) shows the as-measured (points) and calculated (lines) angular-dependent transmittance for high aspect ratio (AR=9.4) moth-eye structures on Si at  $\lambda = 10 \mu\text{m}$ , along with experimental data for a bare Si wafer. For incident angles up to  $\theta = 30^\circ$ , the ME structure agrees with the perfect single-side anti-reflection limit to within 2%; moreover, the ME enhances transmission for all incident angles up to  $\theta = 60^\circ$  from normal. In addition, the omni-directional enhancement in transmission with the ME is largely wavelength independent, as demonstrated in Fig. 7(b).



**Figure 7:** (a) Experimental angle-dependent direct transmission of high aspect ratio (AR=9.4) moth-eye structures on Si at  $\lambda=10\ \mu\text{m}$  (ME, red) compared to a bare Si wafer (Si, black). The calculated single-side anti-reflective limit (SS limit, teal) is also shown. (b) Angle-dependent transmission of the moth-eye sample at different IR wavelengths (8, 10, 14  $\mu\text{m}$  = blue pluses, black triangles and red squares, respectively). The incident angle is measured from the surface normal.



### 5.5. Conclusions

We have outlined a process to create efficient broadband, omni-directional anti-reflective moth-eye structures on Si for mid- to far-IR applications, quantitatively measured their optical performance (e.g., sorting out contributions from direct transmittance, specular reflection, diffuse reflection and forward scattering), and modeled their behavior using effective medium theory. High aspect ratio (9.4) ME structures created with a 320 nm colloidal crystal mask achieved high peak transmittance ( $T > 98\%$  of an ideal anti-reflective surface at  $\lambda = 13 \mu\text{m}$ ), broadband anti-reflection ( $T > 90\%$  for  $\lambda = 7.5\text{-}23\mu\text{m}$ ; less reflection compared to a bare surface from  $\lambda = 6\text{-}45\mu\text{m}$ ), larger bandwidth and better performance compared to a typical commercial interference-based ARC, and omni-directional response (e.g., transmittance greater than bare Si for incident angles from  $0\text{-}60^\circ$  from normal). Optical response (transmission and reflection) of ME structures was quantitatively described with effective medium theory in the infinite wavelength limit, which showed that transmission at long wavelengths was governed by moth-eye feature height. The onset of near-field losses was seen to depend on both the mask size and feature height. As such, controlling the aspect ratio of moth-eye features is the key to achieving both high transmittance and low scattering losses.

The colloidal lithography method presented here to fabricate ME arrays in Si is scalable and extendable to other IR-compatible substrates such as Ge, SiGe, ZnSe, and GaAs. In addition, the mask size, aspect ratio and etch parameters can be adjusted to tune the wavelength-dependent response of the resulting structures. In theory, the moth-eye method can be used to create anti-reflective interfaces from the deep-UV to millimeter wave regions. We have also demonstrated that this method can achieve highly efficient ME structures using quasi-ordered colloidal crystal masks that are easy to deposit. Ultimately, the moth-

eye method provides a facile and scalable way to produce ultra-broadband anti-reflective structures that are largely insensitive to the incident angle of light.

## 5.6. References

- [1] T. Kamizuka, T. Miyata, S. Sako, H. Imada, T. Nakamura, K. Asano, M. Uchiyama, K. Okada, T. Wada, T. Nakagawa, T. Onaka, and I. Sakon, “Development of high-throughput silicon lens and grism with moth-eye antireflection structure for mid-infrared astronomy,” *Proc. SPIE* **8450**, 845051 (2012).
- [2] J. Lau, J. Fowler, T. Marriage, L. Page, J. Leong, E. Wishnow, R. Henry, E. Wollack, M. Halpern, D. Marsden, and G. Marden, “Millimeter-wave antireflection coating for cryogenic silicon lenses,” *Appl. Opt.* **45**, 3746 (2006).
- [3] B. F. Jones and P. Plassmann, “Digital infrared thermal imaging of human skin,” *IEEE Eng. Med. Biol.* **21**, 41 (2002).
- [4] K. Arpin, A. Mihi, H. Johnson, A. Baca, J. Roger, J. Lewis, and P. Braun, “Multidimensional architectures for functional optical devices,” *Adv. Mater.* **22**, 1084 (2010).
- [5] T. Glaser, A. Ihring, W. Morgenroth, N. Seifert, S. Schroter, and V. Baier, “High temperature resistant antireflective moth-eye structures for infrared radiation sensors,” *Microsyst. Technol.* **11**, 86 (2005).
- [6] E. E. Perl, C. Lin, W. E. McMahon, D. J. Friedman, and J. E. Bowers, “Ultrabroadband and wide-angle hybrid antireflection coatings with nanostructures,” *IEEE J. Photovolt.* **99**, 2156-3381 (2014).
- [7] B. Frey, D. Leviton, and T. Madison, “Temperature-dependent refractive index of silicon and germanium,” *Proc. SPIE* **6273**, 6273J (2006).
- [8] H. Raut, V. Ganesh, A. Nair, and S. Ramakrishna, “Anti-reflective coatings: A critical, in-depth review,” *Energy Environ. Sci.* **4**, 3779 (2011).

- [9] S. Chattopadhyay, Y. F. Huang, Y. J. Jen, A. Ganguly, K. H. Chen, and L. C. Chen, "Anti-reflective and photonic nanostructures," *Mater. Sci. Eng. R.* **69**, 1 (2010).
- [10] M. E. Motamedi, W. H. Southwell, and W. J. Gunning, "Antireflection surfaces in silicon using binary optics technology," *Appl. Opt.* **31**, 4371 (1992).
- [11] P. I. Stavroulakis, S. A. Boden, T. Johnson, and D. M. Bagnall, "Suppression of backscattered diffraction from sub-wavelength 'moth-eye' arrays," *Opt. Express* **21**, 1 (2013).
- [12] F. Lora Gonzalez, D. E. Morse, and M. J. Gordon, "Importance of diffuse scattering phenomena in moth-eye arrays for broadband infrared applications," *Opt. Lett.* **39**, 13-16 (2014).
- [13] Y. F. Huang and S. Chattopadhyay, "Nanostructure surface design for broadband and angle-independent antireflection," *J. Nanophotonics* **7**, 073594 (2013).
- [14] G. Xie, G. Zhang, F. Lin, J. Zhang, Z. Liu, and S. Mu, "The fabrication of subwavelength anti-reflective nanostructures using a bio-template," *Nanotechnol.* **19**, 095605 (2008).
- [15] D. B. Nash, "Mid-infrared reflectance spectra (2.3-22 $\mu$ m) of sulfur, gold, KBr, MgO, and halon," *App. Opt.* **24**, 2427 (1986).
- [16] E. D. Palik, *Handbook of Optical Constants of Solids*, (Elsevier, 1985)
- [17] C. C. Katsidis and D. I. Siapkas, "General transfer-matrix method for optical multilayer systems with coherent, partially coherent, and incoherent interference," *App. Opt.* **41**, 3978 (2002).
- [18] R. J. Collins and H. Y. Fan, "Infrared lattice absorption bands in germanium, silicon, and diamond," *Phys. Rev.* **93**, 674 (1954).

## Chapter 6

---

### **A simple colloidal lithography method to fabricate large-area moth-eye anti-reflective structures on Si, Ge, and GaAs for IR applications**

---

*Adapted from the Journal of Vacuum Science and Technology B article:*

F. Lora Gonzalez, L. Chan, A. Berry, D. E. Morse, and M.J Gordon, *JVST B* **32**, 051213 (2014).

### *6.1. Chapter summary*

A two-step colloidal lithography process (Langmuir-Blodgett dip coating + reactive ion etching) was developed to fabricate single and double-sided moth-eye structures in Si, Ge, and GaAs for anti-reflection applications in the IR. Large increases in transmittance were obtained in all three material platforms (up to 97% single-side and 91% absolute transmittance) over the  $\lambda = 4\text{-}20\text{+ } \mu\text{m}$  region. Effective medium theory and the transfer matrix method were used to predict IR optical response of moth-eye substrates as well as investigate the effect of protuberance shape on anti-reflectance behavior. Overall, it is demonstrated that colloidal lithography and etching provide an easy and generic way to synthesize moth-eyes in different IR material platforms.

### *6.2. Introduction*

Recent developments in infrared (IR) optics [1-3], multi-junction solar cells [4], thermal imaging [5,6], and high index thermophotovoltaic materials [7] have created a need for broadband anti-reflective coatings (ARCs) in the IR. Traditional ( $\lambda/4$ ) interference-based ARCs can achieve high transmission at specific wavelengths, but bandwidths are frequently narrow and angular response is poor. Multi-layer ARCs overcome some of these issues; however, they are expensive and time consuming to manufacture (i.e., multiple thin films with different refractive indices and precise thicknesses must be deposited on the surface of interest) [8,9]. In addition, interference-based ARCs are substrate specific; coating materials and processes must be re-engineered when the substrate refractive index changes.

Anti-reflection (AR) based on sub-wavelength structuring of a surface to create a graded refractive index - the so-called moth-eye (ME) effect - offers some benefits over

traditional ARCs [8,9]. These ‘bio-inspired’ surface treatments afford larger bandwidths and omni-directional response, and can theoretically be implemented in any material platform. Moreover, the optical response (e.g., wavelength range, peak transmission, scattering, etc.) of MEs can be tuned for specific applications, provided that the aspect ratio, pitch, and shape of surface protuberances can be adjusted. Although moth-eye nanostructures have been used in the visible to increase solar cell efficiency (i.e., by minimizing reflection losses)[10,11] and reduce glare from surfaces [12], fabrication and optical characterization of large-area ME structures for IR wavelengths have not been extensively explored.

Herein, we present a simple, two-step colloidal lithography method to produce large-area, single and double-sided ME structures on Si, Ge, and GaAs. A monolayer SiO<sub>2</sub> colloidal crystal mask is deposited on the substrate of interest via Langmuir-Blodgett, followed by dry etching tailored for each material. Significant increases in IR transmission for all material platforms were achieved using single (up to 15% absolute increase) and double-sided (up to 44% absolute increase) ME structures. The optical response of fabricated structures was modeled using an effective medium approximation (EMA) and the transfer matrix method; the effect of protuberance shape on ME response was also investigated.

### *6.3. Experimental methods*

Silica colloids ( $d = 380$  nm and 540 nm) were synthesized using a modified, semi-batch Stöber process [13], functionalized with allyltrimethoxysilane (ATMS, Sigma-Aldrich, >98%) in acidic ethanol (pH = 5.5, acetic acid, 10% H<sub>2</sub>O, 10-20 mM ATMS), cured overnight in a vacuum oven (443 K, 8 hrs), and then re-dispersed in 1:2



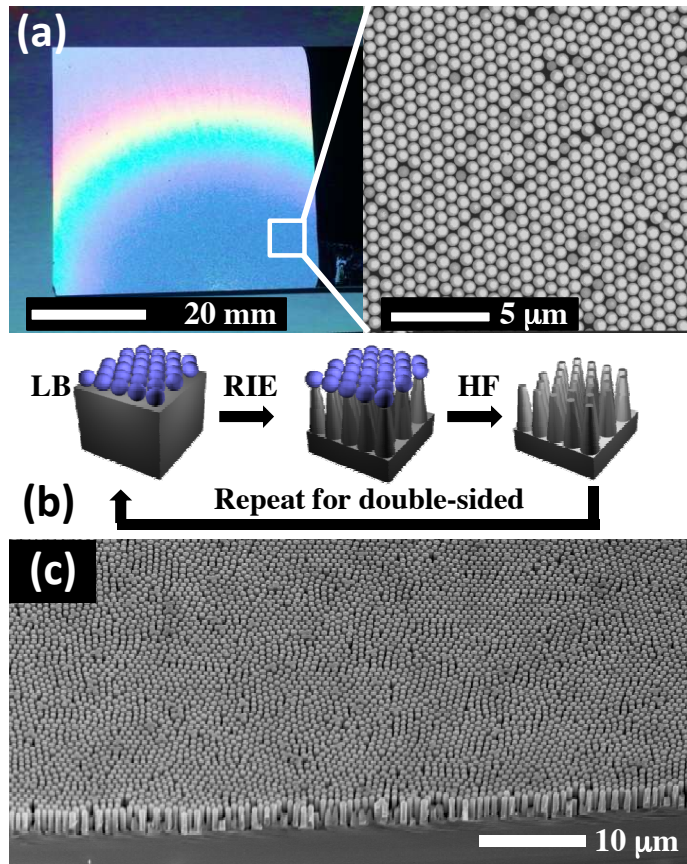
ethanol:chloroform. The colloids were then deposited on undoped Si (University wafer, 225  $\mu\text{m}$  thick,  $>4000\ \Omega\text{-cm}$ ), undoped Ge (MTI Corp., 500  $\mu\text{m}$  thick,  $>50\ \Omega\text{-cm}$ ), or undoped GaAs (MTI Corp., 500  $\mu\text{m}$  thick,  $\sim 1 \times 10^8\ \Omega\text{-cm}$ ) by a Langmuir-Blodgett (LB), dip-coating process (380 nm particles (540 nm) at a constant surface pressure of 8 mN/m (12 mN/m) and dip-coating speed of 2 mm/min) [14].

The LB process allowed rapid deposition of large area colloidal monolayers ( $> 5 \times 5\ \text{cm}^2$ , limited by trough size; Fig. 1(a)) that were free of large defects or gaps for all three material platforms (Si, Ge, GaAs). Colloidal crystal grain sizes were typically  $\sim 10 \times 10\ \mu\text{m}^2$  and there was no discernible difference in mask quality for different substrates or particle sizes. Silica particles can be used directly as etch masks for most group IV and III-V semiconductors with relatively high etch selectivity. In addition, the LB process is simple, tunable and scalable: (1)  $\text{SiO}_2$  colloids can be synthesized with  $d = 50\ \text{nm} - 5\ \mu\text{m}$  with low size dispersion [15], making it easy to adjust ME feature pitch; (2)  $\text{SiO}_2$  is straightforward to functionalize; and (3) large dip-coating troughs can be made. As such, the LB method provides a substrate-independent way of depositing high quality, large-area masks with precise control over pitch without the need for elaborate interference or E-beam based lithography techniques.

Masked samples were plasma etched in a Plasma-Therm 770 SLR-RIE (Si and Ge) or Panasonic-E640 ICP (GaAs) to form ME structures. During etching, the samples were placed on carrier wafers using Santovac-5 diffusion pump oil, which was cleaned off using acetone and ethanol. The mask was then removed with a 10% HF bath. The overall process scheme is shown in Fig. 1(b); for double-sided samples, the process was repeated on the

backside of the substrate. An SEM image of a typical ME structure is shown in Fig. 1(c), and etch conditions for the three materials are summarized in Table I.

**Figure 1:** (a) Large area SiO<sub>2</sub> colloidal crystal deposited on Si using Langmuir–Blodgett. (zoom) SEM image of the colloidal crystal. (b) Process scheme to realize moth-eye structures on various substrates. LB = Langmuir–Blodgett dip coating, RIE = reactive ion etching pattern transfer, and HF = 10% HF bath to remove the colloidal mask. (c) SEM image of large area moth-eye on Si.



Reflection is caused by abrupt changes in refractive index, and can be calculated using the Fresnel equations [9]. For the case of non-absorbing or weakly-absorbing materials (i.e., Si, Ge, and GaAs in the mid-IR), there are two interfaces which contribute to reflection losses. If the front side of a sample is structured with a perfect anti-reflecting surface, the maximum transmission through the sample is limited by the back interface. For Si and GaAs (refractive index  $n_{Si} \sim 3.44$ ,  $n_{GaAs} \sim 3.35$ ), this single-side transmission limit is  $\sim 70\%$ , while

for Ge ( $n_{Ge} \sim 4.02$ ), the single-side limit is  $\sim 65\%$ . In what follows, transmission data for single-sided samples have been normalized by the aforementioned single-sided limit (i.e.,  $T/T_{\max}$ ), calculated using the complex,  $\lambda$ -dependent refractive index for each material (which accounts for absorption) [16-18]. Transmission data for double-sided samples are presented as absolute transmission without normalization. Optical testing of ME structures was done using a Nicolet Magna 850 FTIR Spectrometer with KBr beamsplitter and DTGS detector (2-25  $\mu\text{m}$ ); transmission was measured at  $\sim 5^\circ$  from normal to avoid unwanted reflections between the sample and detector.

#### 6.4. Results and modeling

Single-sided ME samples were synthesized in Si, GaAs, and Ge using mask sizes of  $d = 380 \text{ nm}$ ,  $540 \text{ nm}$ , and  $380/540 \text{ nm}$ , and etch depths of  $800 \text{ nm}$ ,  $1.1 \mu\text{m}$ , and  $1.0/1.4 \mu\text{m}$ , respectively. Transmission spectra are shown in Fig. 2. The Si ME sample (Figs. 2(a),(d)) was etched using an  $\text{SF}_6/\text{C}_4\text{F}_8/\text{Ar}$  plasma to form conical, frustum-like structures; single-side transmission was increased significantly ( $T/T_{\max} = 94\%$  at  $5 \mu\text{m}$ , and  $T/T_{\max} > 90\%$  from  $3.8\text{-}6.5 \mu\text{m}$ ) compared to a bare wafer ( $T/T_{\max} \sim 76\%$ ). The decrease in transmission in the near-IR (NIR) is due to diffuse scattering phenomena (reflection and forward), which has been discussed previously [19]. The present results also demonstrate that diffuse scattering effects can be minimized with higher fidelity pattern transfer using a single-step etch compared to a Bosch process, as has been discussed previously [20].

Similar ME structures were produced in GaAs using a  $\text{Cl}_2/\text{N}_2$  ICP etch at much lower operating pressures ( $1.5 \text{ mT}$ ). Transmission of the GaAs ME structures (Figs. 2(b),(d)) was higher than bare GaAs for  $\lambda > 4 \mu\text{m}$ , with a peak  $T/T_{\max}$  of  $93\%$  at  $\lambda = 6.4 \mu\text{m}$ . The red-

shift in peak transmittance for GaAs compared to Si is due to larger protuberance pitch (540 vs. 380 nm masks) and deeper etch (1.1  $\mu\text{m}$  vs. 800 nm). The peak transmittance for GaAs is somewhat less than Si, likely due to the slightly concave etch profile of the former [8].

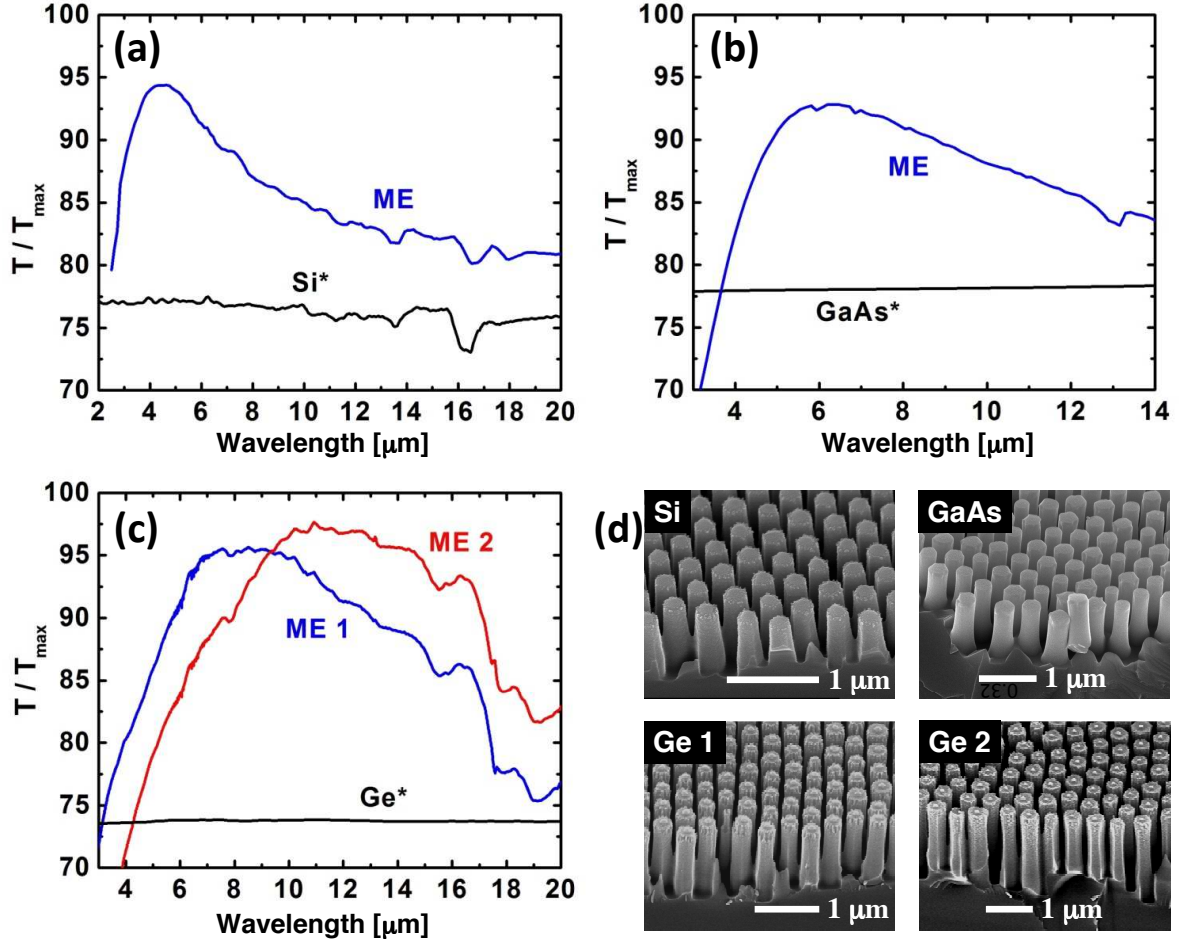
Germanium structures (Figs. 2(c),(d)) were etched with the same chemistry as Si, with slight modification to gas flows and bias power (see Table I) to increase sidewall passivation and sputtering. The result was higher aspect ratio structures that maintained a convex, frustum-like profile. Single-side transmission of Ge MEs was significantly higher than bare Ge in the  $\lambda = 2\text{-}20 \mu\text{m}$  (380 nm mask) and  $4\text{-}20 \mu\text{m}$  (540 nm mask) ranges. The small mask sample (ME 1) had a peak single-side transmission of 96% for  $\lambda = 7.5\text{-}9 \mu\text{m}$ , and  $T/T_{\text{max}} > 90\%$  for  $6 \mu\text{m} < \lambda < 13 \mu\text{m}$ , while the large mask sample (ME 2) had peak transmission of 97% at  $\lambda = 11 \mu\text{m}$ , and  $T/T_{\text{max}} > 90\%$  for  $8 \mu\text{m} < \lambda < 17 \mu\text{m}$ .

An effective medium approximation (EMA) approach was used to calculate the transmission of various ME structures to understand the effect of feature shape on optical behavior. Briefly, the EMA allows one to calculate the effective refractive index profile of the ME structure,  $n_{\text{eff}}(h, \lambda)$ , from a known feature shape, where  $h$  is the height of the feature. In this work, the Bruggeman model was used, which has been shown to be fairly accurate for ME structures [8,21]:

$$\frac{f}{1-f} \frac{n_{\text{Si}}^2 - n_{\text{eff}}^2}{n_{\text{Si}}^2 + 2n_{\text{eff}}^2} = \frac{n_{\text{eff}}^2 - 1}{2n_{\text{eff}}^2 + 1} \quad (1)$$

Here,  $n_{\text{Si}}$  is the  $\lambda$ -dependent refractive index of Si, and  $f$  is the ‘shape’ factor. Optical behavior (transmission, reflection, etc.) of MEs was then calculated using a transfer matrix method for an equivalent stack of layers with refractive indices extracted from the refractive index profile [22]. In this study, 100 layers were found to be sufficient for convergence.

**Figure 2:** Normalized single-side transmittance ( $T/T_{\max}$ ) measured for moth-eye structured Si (a), GaAs (b), and Ge (c) compared to unstructured surfaces (black). ME is the moth-eye data and \* denotes that transmission spectra for bare surfaces were calculated from the  $\lambda$ -dependent, complex refractive index of each material. The large dip in Si spectra near 16  $\mu\text{m}$  is due to phonon absorption. ME 1 and ME 2 in panel (c) were created with different mask sizes: 380 vs 540 nm. (d) SEM images of the moth-eyes shown in panels (a)–(c).



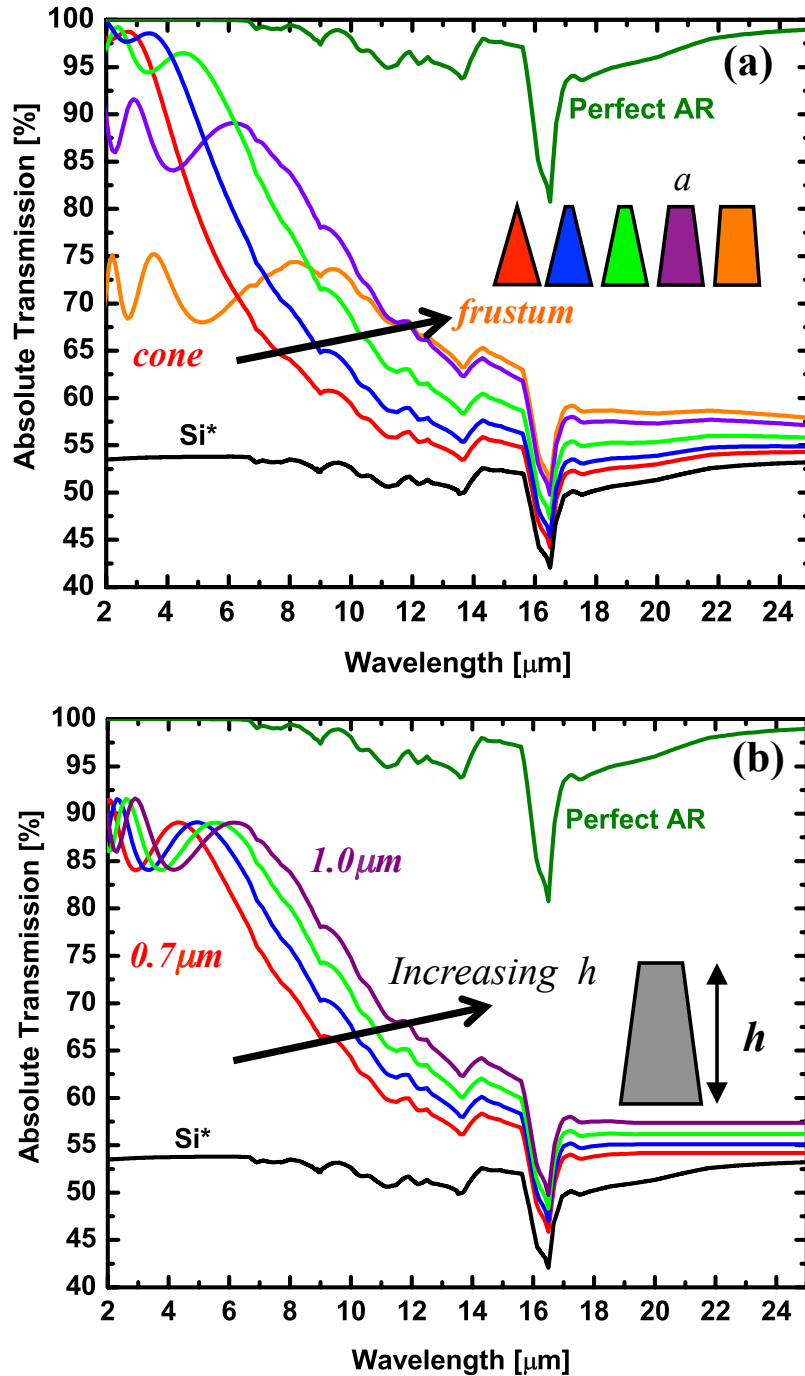
Protuberance shape was taken to be a conical frustum, with top-to-base diameter ratio  $a = 0 \rightarrow 0.8$ , where the  $f$  used to calculate the  $h$ -dependent, effective refractive index  $n_{\text{eff}}(h, \lambda)$  is given by:

$$f(h) = 0.907(1 - (1 - a)h)^2. \quad (2)$$

The 0.907 factor accounts for unmasked areas of the substrate when frusta are hexagonally closed packed on the surface.

Figure 3(a) shows calculated transmission spectra for doubled-sided Si MEs made of frusta ( $h = 1 \mu\text{m}$ ) with increasing top diameter, as compared to a bare Si wafer (black) and perfect ARC (green; absorption is included). For the same frustum height, increasing the top diameter ( $a = 0 \rightarrow 0.8$ ) leads to (1) lower and more red-shifted peak transmittance and (2) higher transmission at longer wavelengths. The first effect is due to an increasing step discontinuity in refractive index at the frustum top; this increases reflection (and lowers transmission), as predicted by the Fresnel equations. The second effect is due to a larger fraction of high index material (Si) in the ME film (i.e., the refractive index variation is more gradual), which biases the moth-eye effect to longer wavelengths. The effect of protuberance height was also investigated (Fig. 3(b)); in this case ( $a = 0.6$ , fixed), peak transmission remains constant and red-shifts, and far-IR transmission goes up as  $h$  increases. Similar trends are seen for Ge and GaAs, with the exception that phonon losses at  $\sim 16 \mu\text{m}$  are not present; in addition, Ge and GaAs have effectively no absorption in the near and mid-IR ranges (unlike Si), making absolute transmission for perfect AR = 100%. Ultimately, aspect ratio is the most important parameter to control to achieve high transmission while maintaining broadband response; however, protuberance shape does affect the peak  $T/T_{\text{max}}$  and width of the transmission curve.

**Figure 3:** Effect of shape (a) and height (b) of double-sided moth-eye protuberances on the absolute transmission of Si, calculated using effective medium theory. Calculated spectra for a perfect, double-sided antireflective coating (Perfect-AR, green, absorption only) and a bare Si wafer (Si\*, black) are also shown. For panel (a), shape (inset) was varied from a perfect cone to a frustum with top-to-bottom diameter ratio of  $a = 0.8$  with height  $h = 1\mu\text{m}$ . For (b), the frustum diameter ratio was set at  $a = 0.6$ , and height was varied from  $0.7$  to  $1.0\mu\text{m}$  in  $100\text{ nm}$  steps. The large dip in Si spectra near  $16\mu\text{m}$  is due to phonon absorption.

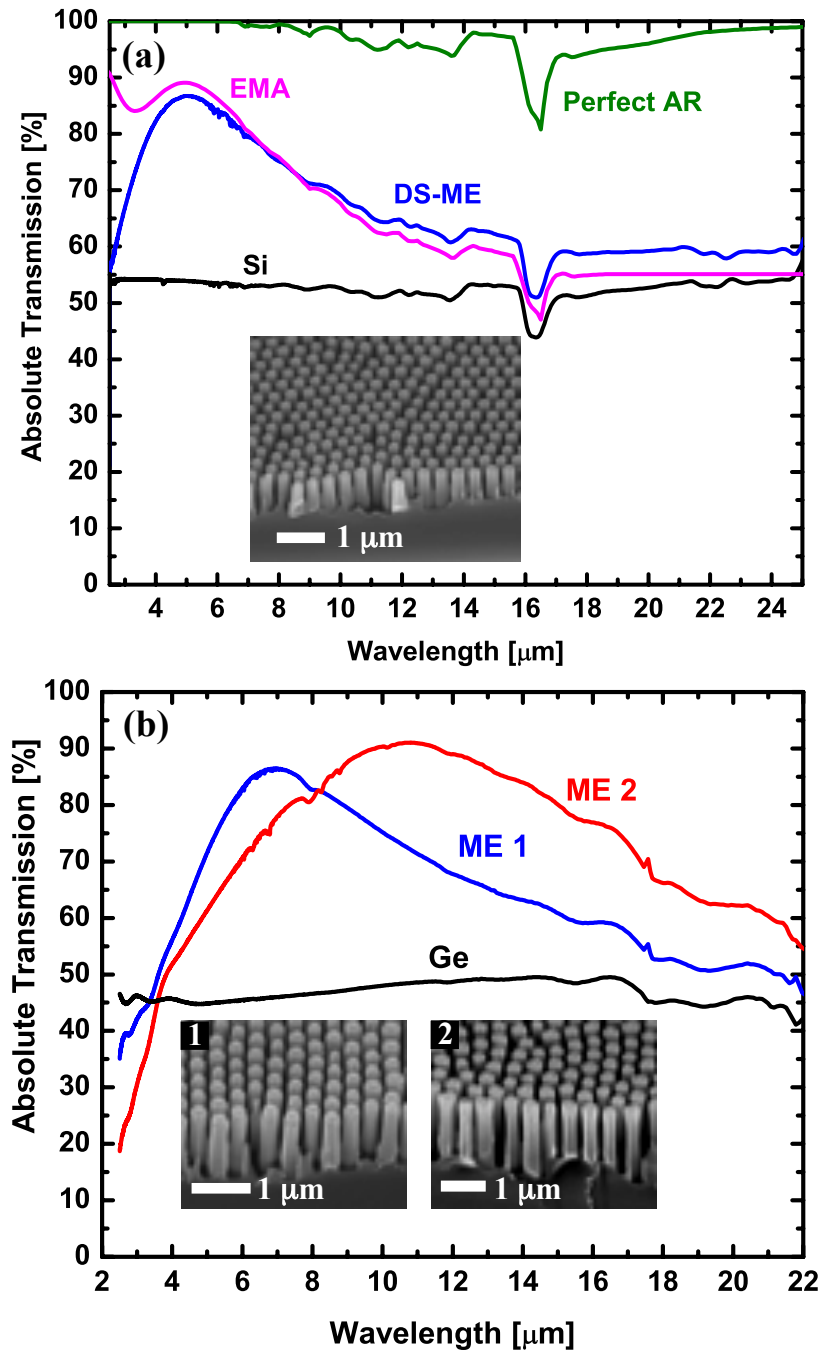


In an effort to increase IR transmission even further, double-sided ME samples were fabricated in Si and Ge by repeating the LB and etching process on the back side of substrates. There was no need to protect the first structured side of the sample during coating and etching steps; SEM confirmed that after cleaning and mask removal, the original ME structures remained intact, even after mounting the samples onto carrier wafers with oil. Absolute transmission spectra of three double-sided samples are shown in Figure 4. The Si ME sample (Fig. 4(a), blue) was modeled using the EMA for a frustum with  $a = 0.6$  and  $h = 800$  nm (Fig. 4(a), magenta). Peak absolute transmission ( $T_{\text{abs}}$ ) for this sample was 86% at approximately  $5.5 \mu\text{m}$ , with  $T_{\text{abs}} > 80\%$  for  $3.8 \mu\text{m} < \lambda < 7 \mu\text{m}$ . The transmission peak appears slightly red-shifted ( $< 0.5 \mu\text{m}$ ) from the single-side case due to additional diffuse scattering from the two ME faces at NIR wavelengths. Despite its simplicity, the EMA model does an excellent job in predicting the  $\lambda$ -location and magnitude (within 5%) of  $T_{\text{abs}}$ . Differences between the predicted and measured values can be attributed to diffuse scattering losses, mask imperfections, and variations in etch depth. Ultimately, the absolute transmission of Si in the IR range was increased by  $\sim 34\%$  using the double-sided ME approach.

Double-sided MEs were also fabricated on Ge (Fig. 4(b)) using the same etch conditions as single-sided samples. ME 1 (380 nm mask,  $1 \mu\text{m}$  etch, blue) and ME 2 (540 nm mask,  $1.4 \mu\text{m}$  etch, red) had peak  $T_{\text{abs}} = 87\%$  at  $\lambda = 7 \mu\text{m}$  and  $T_{\text{abs}} > \text{bare Ge}$  from  $3.5\text{-}22 \mu\text{m}$ , and  $T_{\text{abs}} = 91\%$  at  $\lambda = 10.8 \mu\text{m}$  and  $T_{\text{abs}} > \text{bare Ge}$  from  $3.7\text{-}25 \mu\text{m}$ , respectively. As predicted by EMA calculations and seen experimentally, deeper etching gave higher overall transmission and better AR deeper into the mid-IR. Overall, absolute transmission of Ge was increased by  $\sim 44\%$  in the IR compared to a bare wafer using double-sided ME structuring.



**Figure 4:** Absolute transmittance measured for double-sided moth-eye structured Si (a) (ME, blue, 380 nm mask) and Ge (b) (ME 1, blue, 380 nm mask; ME 2, red, 540 nm mask) compared to unstructured surfaces (Si or Ge, black). The EMA prediction (EMA, magenta and teal) and calculated spectrum for a perfect, double-sided antireflective coating on Si (P-AR, green, absorption only) are also shown. Since Ge has no absorption in the 2–24  $\mu\text{m}$  range, the perfect, double-sided AR transmission limit is 100%; as such, no spectrum is shown for this case in panel (b). The large dip in Si spectra near 16  $\mu\text{m}$  is due to phonon absorption. (Insets) SEM images of the moth-eye substrates.



### *6.5. Summary and conclusions*

In this work, we demonstrated a generic, two-step lithography and pattern transfer method, based on Langmuir-Blodgett deposition and reactive ion etching, to create moth-eye anti-reflective structures in different materials (Si, Ge, GaAs) for the IR. Large increases in transmittance were obtained in all three material platforms (up to 97% single-side and 91% absolute transmittance) over the  $\lambda = 4\text{-}20\text{+ } \mu\text{m}$  region using single- and double-side moth-eye structuring. It was also shown that effective medium theory quantitatively captures ME optical behavior in the long wavelength limit, and provides general rules to understand how feature geometry will affect peak transmission, bandwidth, and far-IR performance. The overall approach presented here can be extended to different material platforms and wavelength ranges to increase the efficiency and performance of various visible and infrared electro-optical (EO) technologies. For example, foreseeable application areas include (i) increasing the efficiency of solar cells and thermophotovoltaics for energy conversion by reducing reflection losses, and (ii) controlling reflection and diffusivity of critical surfaces in EO systems such as optical detectors and imagers.

## 6.6. References

- [1] Z. Liu, J. Yang, A. Flores, and M. Wang, “Diffractive infrared lens with extended depth of focus,” *Opt. Eng.* **46**, 1 (2007).
- [2] G. Muyo, A. Singh, M. Andersson, D. Huckridge, and A. R. Harvey, “Infrared imaging with a wavefront-coded singlet lens,” *Opt. Express* **17**, 21118 (2009).
- [3] J. Yan, K. Maekawa, J. Tamaki, and T. Kuriyagawa, “Micro grooving on single-crystal germanium for infrared Fresnel lenses,” *J. Micromechanics Microengineering* **15**, 1925 (2005).
- [4] D. J. Friedman, “Progress and challenges for next-generation high-efficiency multijunction solar cells,” *Curr. Opin. Solid State Mater. Sci.* **14**, 131 (2010).
- [5] A. Rogalski, “Infrared detectors: an overview,” *Infrared Phys. Technol.* **43**, 187 (2002).
- [6] B. Jones and P. Plassmann, “Digital infrared thermal imaging of human skin,” *IEEE Eng. Med. Biol.* **41**, 0739-5175 (2002).
- [7] C. Ferrari, F. Melino, M. Pinelli, P. R. Spina, and M. Venturini, “Overview and Status of Thermophotovoltaic Systems,” *Energy Procedia* **45**, 160 (2014).
- [8] S. Chattopadhyay, Y. F. Huang, Y. J. Jen, A. Ganguly, K. H. Chen, and L. C. Chen, “Anti-reflecting and photonic nanostructures,” *Mater. Sci. Eng. R* **69**, 1 (2010).
- [9] H. K. Raut, V.A. Ganesh, A.S. Nair, and S. Ramakrishna, “Anti-reflective coatings: A critical, in-depth review,” *Energy Environ. Sci.* **4**, 3779 (2011).
- [10] B. M. Phillips, P. Jiang, and B. Jiang, “Biomimetic broadband antireflection gratings on solar-grade multicrystalline silicon wafers,” *Appl. Phys. Lett.* **99**, 191103 (2011).

- [11] Y. M. Song, Y. Jeong, C. I. Yeo, and Y. T. Lee, "Enhanced power generation in concentrated photovoltaics using broadband antireflective coverglass with moth eye structures," *Opt. Express* **20**, A916 (2012).
- [12] P. I. Stavroulakis, S. A. Boden, T. Johnson, and D. M. Bagnall, "Suppression of backscattered diffraction from sub-wavelength 'moth-eye' arrays," *Opt. Express* **21**, 1 (2013).
- [13] W. Stöber, A. Fink, and E. Bohn, "Controlled growth of monodisperse silica spheres in the micron size range," *J. Colloid Interface Sci.* **26**, 62 (1968).
- [14] A. Gil and F. Guitián, "Formation of 2D colloidal crystals by the Langmuir-Blodgett technique monitored by in situ by Brewster angle microscopy," *J. Colloid Interface Sci.* **307**, 304 (2007).
- [15] S. Mok, M. Lee, W. Kim, and S. M. Chang, "Preparation of large monodispersed spherical silica particles using seed particle growth," *J. Colloid Interface Sci.* **286**, 536 (2005).
- [16] E. D. Palik, *Handbook of Optical Constants of Solids* (Academic Press, Boston, 1997).
- [17] B. J. Frey, D. B. Leviton, and T. J. Madison, "Temperature dependent refractive index of silicon and germanium," *Proc. SPIE* **6273**, 10 (2006).
- [18] V. G. Plotnichenko, V. O. Nazaryants, E. B. Kryukova, and E. M. Dianov, "Spectral dependence of the refractive index of single-crystalline GaAs for optical applications," *J. Phys. D. Appl. Phys.* **43**, 105402 (2010).
- [19] F. Lora Gonzalez, D. E. Morse, and M. J. Gordon, "Importance of diffuse scattering phenomena in moth-eye arrays for broadband infrared applications," *Opt. Lett.* **39**, 13 (2014).

- [20] F. Lora Gonzalez and M. J. Gordon, "Bio-inspired, sub-wavelength surface structures for ultra-broadband, omni-directional anti-reflection in the mid and far IR," *Opt. Express* **22**, 12808 (2014).
- [21] K. Han and C.H. Chang, "Numerical modeling of Sub-wavelength Anti-reflective Structures for Solar Module Applications," *Nanomaterials* **4**, 87 (2014).
- [22] C. Katsidis and D. Siapkas, "General transfer-matrix method for optical multilayer systems with coherent, partially coherent, and incoherent interference," *Appl. Opt.* **41**, 3978 (2002).

## Chapter 7

---

### **Enhancing near-infrared light absorption in PtSi thin films for Schottky barrier IR detectors using moth-eye surface structures**

---

*Adapted from the Optics Letters article:*

F. Lora Gonzalez and M.J. Gordon, *Optics Letters*, submitted (2015).

### *7.1. Chapter summary*

Si-based Schottky barrier infrared detectors typically use thin (1-10nm) PtSi or Pd<sub>2</sub>Si layers grown on Si substrates as an absorption medium. Herein, we demonstrate the use of sub-wavelength moth-eye (ME) structures on the Si substrate of such detectors to enhance absorption of near infrared (NIR) light in the active PtSi layer to increase detector efficiency. Absorbance enhancement of 70-200% in the  $\lambda=1-2.5\mu\text{m}$  range is demonstrated in crystalline PtSi films grown via electron beam evaporation of Pt and subsequent vacuum annealing. Low total reflectance (<10%) was measured for ME films, demonstrating the efficacy of the moth-eye effect. Effective medium approximation calculations show that absorption enhancement at short wavelengths is partly due to forward scattering, which increases the effective optical path length in PtSi. Results also suggest that moth-eye structuring of substrates is a general and low-cost method to enhance absorption in a variety of IR material platforms used for back-illuminated detectors.

### *7.2. Introduction*

Silicon-based internal photoemissive detectors are extensively used for near and mid infrared (1-6 $\mu\text{m}$ ) detection due to their low cost, ease of fabrication, and compatibility with existing Si processing technologies. Many of these devices rely on a thin active layer (e.g., < 10 nm PtSi or Pd<sub>2</sub>Si) where infrared (IR) absorption creates hot carriers, which are eventually separated at the PtSi/Si Schottky junction and emitted into the Si substrate [1-14]. Elastic scattering at interfaces and grain boundaries in the PtSi layer is beneficial because it increases the probability of internal photoemission by increasing the chance that carriers will be re-directed into the Si. However, increasing the active layer thickness leads to inelastic

losses, e.g., scattering with phonons and cold electrons. As such, the emission probability and quantum efficiency (QE) of a device strongly depends on film thickness [2,4,15-17], usually necessitating the use of very thin PtSi active layers. Unfortunately, as the PtSi film thickness is decreased, absorption becomes a real problem [9-11]. To circumvent this, PtSi/Si Schottky junctions are commonly put inside an optical cavity (e.g., SiO<sub>2</sub>/Si/PtSi/SiO<sub>2</sub> + Al or Au back reflector) to create a standing wave in the active PtSi layer [15].

In this work, we use bio-inspired moth-eye surface structures [18,19] to increase absorption in Schottky barrier PtSi thin films, eliminating the need for optical cavities or back-side reflectors. Moth-eye surfaces were structured onto the back-side of the Si substrate, allowing the front side of the PtSi/Si detector to remain unchanged. Absorption enhancements of 70-200% in the PtSi active layer were achieved at normal incidence compared to the front and back-illuminated cases for a typical Schottky barrier device architecture without an optical cavity. The measured absorption enhancement was higher than predicted by transfer matrix method calculations because of forward scattering by moth-eye structures.

### *7.3 Experimental methods*

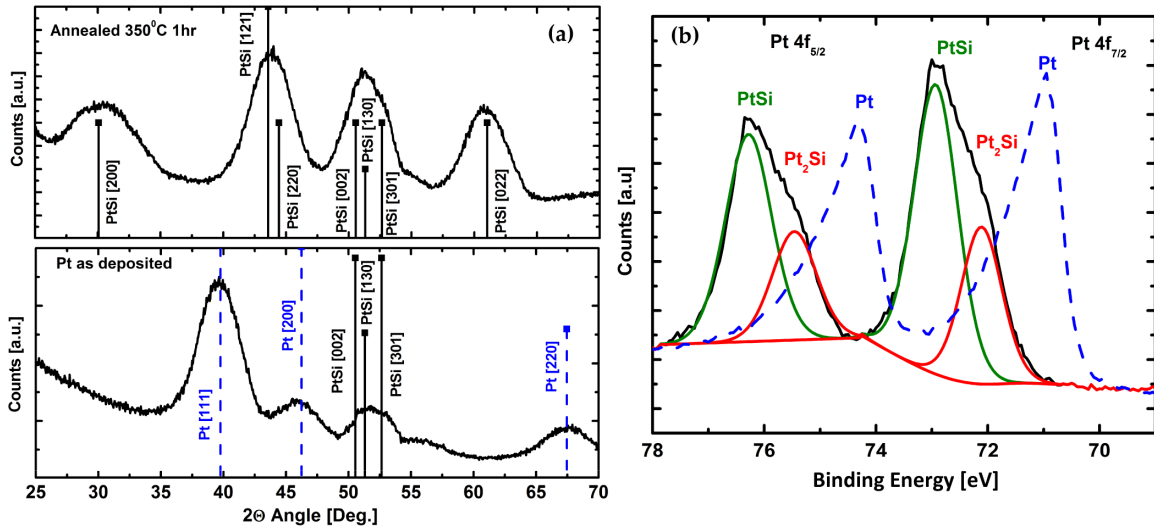
PtSi films were synthesized by electron beam evaporation of ~10nm Pt metal onto Piranha and HF-cleaned p-type Si (10-20 Ω\*cm, University Wafer) at 3.0x10<sup>-8</sup> torr; the deposited films were then annealed in vacuum (<6.0x10<sup>-7</sup> torr) at 350°C for 1 hour. Glancing angle (1°) XRD and XPS spectra (Fig. 1) confirm the formation of crystalline PtSi with some Pt<sub>2</sub>Si and no remaining Pt metal [7,20–24].

Moth-eye samples were fabricated using a colloidal lithography method discussed elsewhere [19,25]. Briefly, close-packed silica colloid (*d*=170 or 380nm) monolayers were



deposited onto Si using Langmuir-Blodgett transfer, subsequently etched in an Ar/C<sub>4</sub>F<sub>8</sub>/SF<sub>6</sub> plasma, and the colloid mask was removed in an HF bath. The aspect ratio of the moth-eye structures was kept constant at ~2, with a conical frustum-like shape, which has been previously shown to give good anti-reflective properties [19].

**Figure 1:** (a) Glancing angle XRD spectra of as-deposited (bottom) and annealed (top) samples showing the formation of crystalline PtSi, and the complete transformation of Pt metal to silicides. (b) Pt 4f XPS spectra of as-deposited (dashed blue) and annealed (black) samples, with the annealed sample peaks deconvoluted into PtSi (green) and Pt<sub>2</sub>Si (red) bonding states.

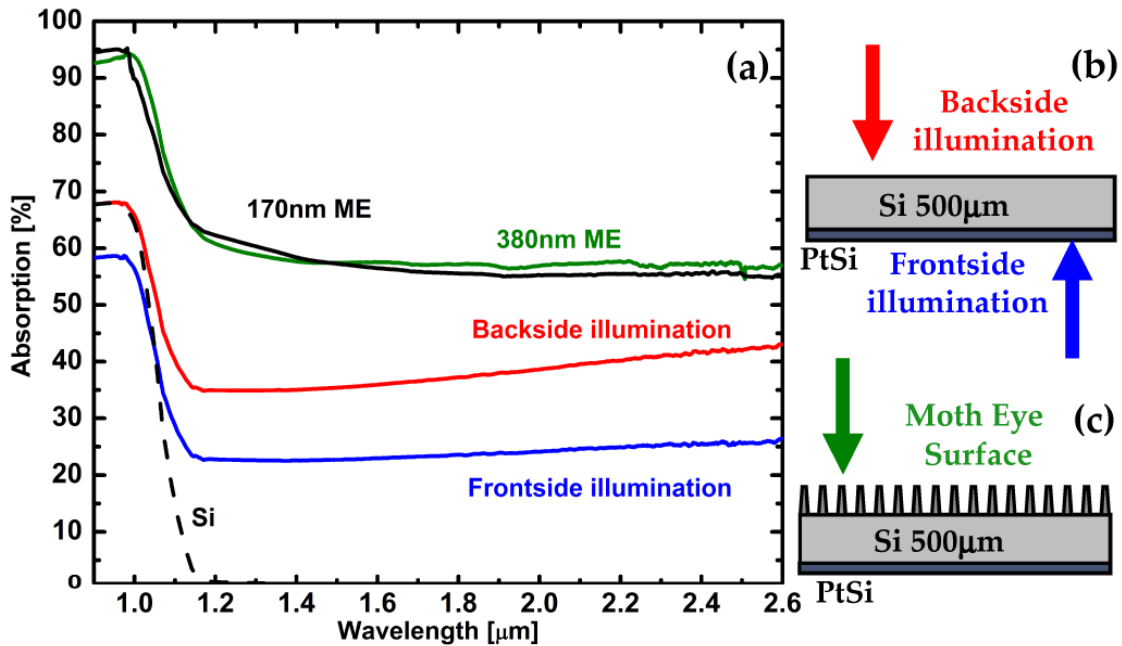


After creating the ME, the PtSi film was formed using the same method described above on the flat side of the sample. All of the PtSi layers were fabricated in parallel (same e-beam and annealing runs) and the e-beam sample stage was rotated during deposition to ensure uniformity between the samples. Optical absorption was measured using a Shimadzu UV-3600 UV-Vis-NIR Spectrophotometer with an integrating sphere attachment. Total hemispherical reflectance ( $R$ ) and transmission ( $T$ ) were measured, with absorbance ( $a$ ) calculated by difference ( $a = 1 - T - R$ ).

#### 7.4 Results and discussion

Figure 2 shows the measured absorbance ( $I-T-R$ ) of a flat PtSi/Si sample in front-side (FI, blue) and back-side side illumination (BI, red) modes, and the two moth-eye modified samples ( $d=170\text{nm}$ , black;  $d=380\text{nm}$ , green). Absorbance of the FI sample was  $\sim 20\text{-}25\%$ , and the BI geometry improved the absorbance to  $35\text{-}42\%$ . This improvement is due to the Si substrate acting as an index-matching layer in the BI mode, lowering the reflection loss from the air/PtSi interface. The moth-eye samples show absorbance of  $\sim 55\text{-}60\%$ , which corresponds to an enhancement factor of  $170\text{-}200\%$  over the FI mode, and  $\sim 70\%$  over the BI mode.

**Figure 2:** (a) Experimentally measured absorption of front-side (blue) and back-side (red) illuminated ( $\sim 12\text{ nm}$ ) PtSi on Si, along with moth-eye (ME) structured Si/PtSi samples ( $d=170\text{nm}$ , black;  $d=380\text{nm}$ , green) in the back-illuminated configuration. (b-c) Optical configurations for absorption measurements. The calculated absorption component of Si below the gap is shown by the dashed black line. The ME enhances the absorption in the PtSi film by  $70\text{-}200\%$  over the front-side and back-side illumination modes.



To understand the effect of moth-eye structures on the absorbance characteristics of PtSi/Si samples, an effective medium approximation (EMA) was developed in conjunction with a transfer matrix method (TMM) to calculate the normal-incidence transmission, reflection, and absorption [26]. Figure 3(inset) shows the geometry of the optical stack; the EMA was formulated by discretizing ME structures into a stack of 100 equivalent layers of refractive index  $n_{eff}(h, \lambda)$ , given by the Bruggeman equation [27–29],

$$\frac{f}{1-f} \frac{n_{Si}^2 - n_{eff}^2}{n_{Si}^2 + 2n_{eff}^2} = \frac{n_{eff}^2 - 1}{2n_{eff}^2 + 1}, \quad (1)$$

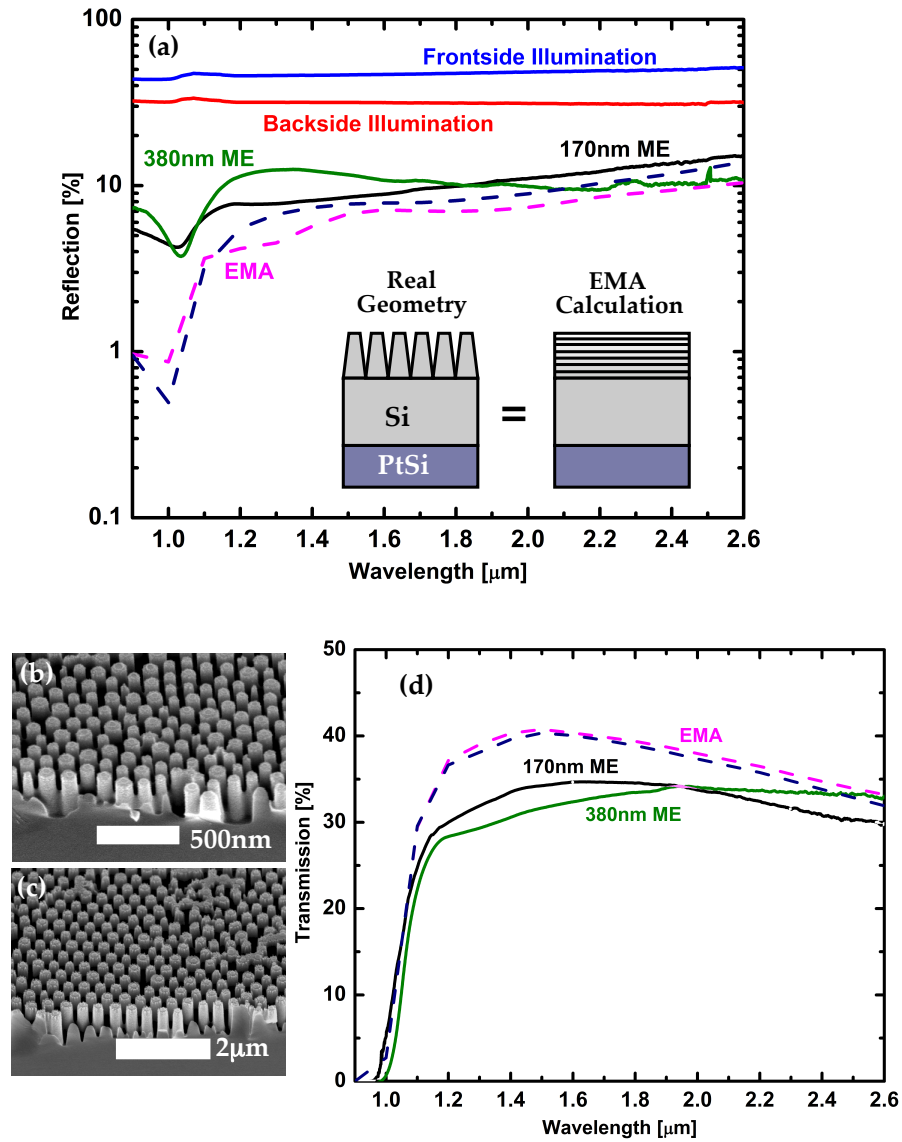
where  $f$  is a shape factor based on feature geometry and  $h$  is the ME structure height. In this case,  $f = 0.907(1-0.4h)^2$ , which corresponds to hexagonally close-packed conical frusta with a top-to-bottom radius ratio of 0.6. The complex,  $\lambda$ -dependent refractive indices for Si and PtSi were obtained from [10,30].

Figure 3(a) shows the calculated and measured reflectance for ME-structured and flat (unstructured) samples in front- and back-side illumination; the two flat samples have significant reflection (~45%, front-side; ~30%, back-side), while the moth-eye samples ( $d=170\text{nm}$ , black;  $d=380\text{nm}$ , green) all have low reflection, <10% for most of the spectral range. The EMA ( $h = 800\text{nm}$ , dashed magenta;  $h = 400\text{nm}$ , dashed navy) is within experimental error of the measured values for the ME samples above  $2\mu\text{m}$ . The measured reflectance, however, deviates from the EMA calculation at shorter wavelengths, particularly for the 380nm ME, because the EMA and TMM calculations are for normal incidence only, and do not account for forward scattering or diffractive effects. As such, the EMA calculation can only be quantitative in the infinite- $\lambda$  limit for ME structures, as has

been shown in previous studies [25,29,31]. The forward scattering and diffractive components of the transmitted light tend to enhance absorption in the PtSi layer.

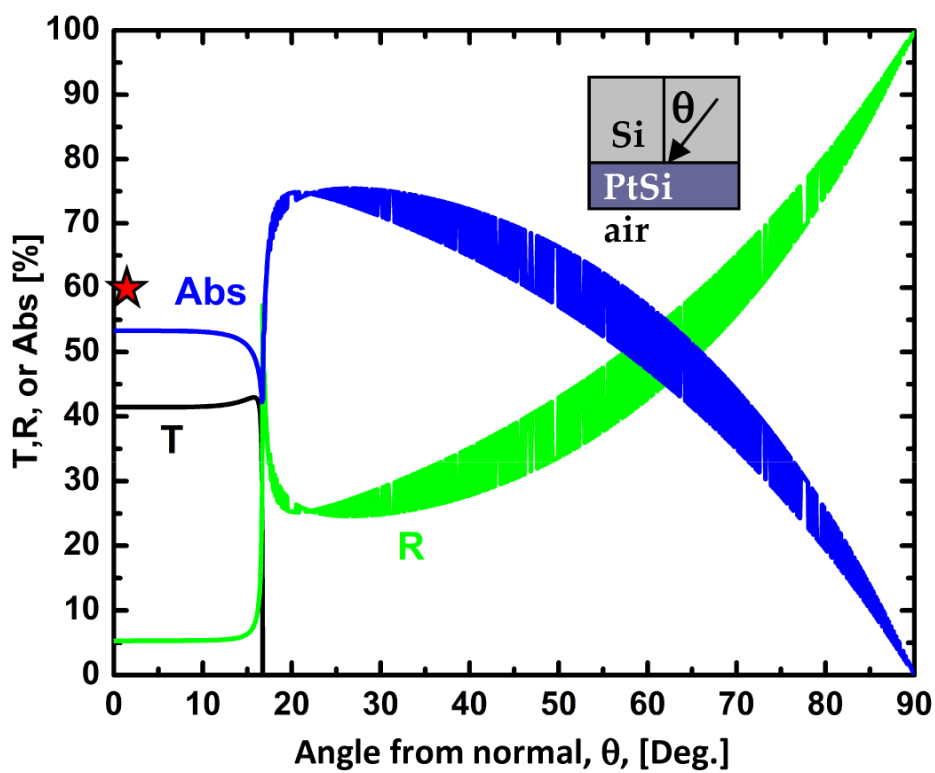
Figure 3(d) shows the measured total transmission through the two moth-eye samples, as compared to the transmission predicted by the EMA model. For both ME samples, the measured transmission is significantly lower than the prediction, supporting the premise that the ME leads to greater forward scattering and diffractive effects which increase the effective path length in PtSi. As such, moth-eye structures are seen to not only provide anti-reflection that reduces losses at the air/Si interface, but they also foster light trapping by redirecting light into angles that increase the effective optical path length in the PtSi layer.

**Figure 3:** (a) Measured total hemispherical reflectance of planar (front-side, blue; back-side, red) and ME samples ( $d = 170\text{nm}$ , black;  $d = 380\text{nm}$ , green), and EMA-calculated reflectance ( $h = 800\text{nm}$ , dashed magenta;  $h = 400\text{nm}$ , dashed navy). (inset) Schematic representation of the effective medium approximation calculation. The real geometry is modeled as a stack of 100 equivalent layers with refractive index  $n_{eff}$ , given by equation 1. (b,c) SEM images of moth eye surfaces (170nm and 380nm masks, respectively). (d) Measured total transmission of ME samples ( $d = 170\text{nm}$ , black;  $d = 380\text{nm}$ , green), and EMA-calculated transmission ( $h = 800\text{nm}$ , dashed magenta;  $h = 400\text{nm}$ , dashed navy). The transmission through the ME sample is lower than predicted by the EMA due to forward scattering and light trapping.



To show the importance of forward scattering in ME systems, absorption, transmission, and reflection were calculated as a function of angle at  $\lambda=1.5\mu\text{m}$  by applying the TMM to the Si/PtSi (12nm)/air stack, ignoring the first air/Si interface (see Fig. 4). The Si/PtSi/air stack can be “de-coupled” from the first air/Si interface because the Si wafer is thick enough ( $500\mu\text{m}$ ) so that there is no interference within the Si, i.e., the coherence length  $\ll$  substrate thickness. At low angles, the transmission is  $\sim 41\%$ , and falls to 0% above the critical angle ( $\sim 17^\circ$ ), which corresponds to total internal reflection within the Si/PtSi/air stack. The absorption, which is approximately 54% at small angles, is significantly increased above the critical angle, with a peak of 75% at  $22^\circ$  from normal. The reflection is also increased, from 5% to 25% at  $22^\circ$ . The absorption and reflection curves have high frequency oscillations due to calculated interference between the Si/PtSi and PtSi/air interfaces. The red star at  $\theta=0^\circ$  (59%) represents the experimentally measured absorbance of ME samples at  $\lambda=1.5\mu\text{m}$ , suggesting that some portion of the incoming light is diverted into angles greater than the critical angle. The model results correlate well with the transmission and reflectance data measured for the ME samples; for example, the 380nm ME sample reflects about 10%, transmits about 30%, and absorbs 59% at  $1.5\mu\text{m}$ . This correlates roughly to 6% more absorption than predicted by the EMA. While the majority of the light is transmitted through the ME layer without scattering, some portion ( $>20\%$ , based on the aforementioned numbers), is scattered into higher angles. The effect of higher reflection and lower transmission is less pronounced with smaller ME (170nm) structures, but the end result (higher absorption) is the same.

**Figure 4:** Absorption (Abs, blue), reflection (R, green), and transmission (T, black) calculated as a function of angle in the Si/PtSi/air stack (inset). Above the critical angle ( $\sim 17^\circ$ ), transmission decreases from 40% to 0%, reflection is increased by  $>20\%$ , but absorption is increased to 75%. The red star represents the experimentally measured absorption (from Fig. 2) of the ME samples, which is approximately 6% higher than predicted by the EMA at normal incidence.



For the ME structures investigated in this study, the diffraction equation cannot be used to quantitatively predict the onset of diffracted orders and forward scattering because the ME structures are quasi-ordered. Although the diffraction equation predicts that the onset of diffraction depends only on pitch, previous studies have shown that scattering behavior also depends on profile shape and height, which provides additional control over optical characteristics [25,31]. In fact, tuning the profile, aspect ratio and height to foster forward scattering can be used to enhance absorption in PtSi layers even further, without the need for conventional AR coatings or optical cavities.

### *7.5 Conclusions*

In this study, we showed that moth-eye (ME) structures can be fabricated on the substrate of Schottky barrier IR detectors to increase absorption of IR light in the PtSi active layer by factors of 70-200% over bare PtSi or Si/PtSi samples, without the use of an optical cavity or conventional thin-film anti-reflective layers. ME structures were also seen to enhance absorption by an additional 7-20% over the predicted (EMA and TMM) absorption due to forward scattering and diffractive effects that led to light trapping in the active PtSi layer. Finally, the ME anti-reflectance and light trapping scheme presented herein will not affect the electronic architecture of PtSi/Si Schottky diode devices, and can potentially be used in other back-illuminated detectors, such as HgCdTe, PtSi doping spike, GeSi/Si, PtSi/SiGe/Si, IrSi-Si, and InGaAs [2,4,15], to increase efficiency.



## 7.6. References

- [1] C. K. Chen, B. Nechay, and B. Tsaur, "Ultraviolet, Visible, and Infrared Response of PtSi Schottky-Barrier Detectors Operated in the Front-Illuminated Mode," *IEEE Transactions on Electronic Devices* **38**, 1094 (1991).
- [2] A. Rogalski, "Infrared detectors: an overview," *Infrared Phys. Technol.* **43**, 187 (2002).
- [3] A. Akiyama, T. Sasaki, T. Seto, A. Mori, R. Ishigaki, S. Itoh, N. Yutani, M. Kimata, and N. Tubouchi, "1040x1040 infrared charge sweep device imager with PtSi Schottky-barrier detectors," *Optical Eng.* **33**, 64 (1994).
- [4] A. Rogalski, "Infrared detectors: status and trends," *Prog. Quantum Electron.* **27**, 59 (2003).
- [5] A. van der Ziel, "Schottky Barrier diode as an infrared low-level detector," *Physica* **81B**, 111 (1976).
- [6] W. Kosonocky, "Infrared image sensors with Schottky-barrier detectors," *SPIE Technologies for Optoelectronics* **869**, 90 (1987).
- [7] L. Shuang, Z. Zhiyong, N. Yonggong, C. Ai, Z. Huaiwu, and Y. Jiade, "Formation of ultra-thin PtSi film by vacuum annealing," *Vacuum* **65**, 133 (2002).
- [8] J. Yin, W. Cai, Y. Zheng, and L. Zhao, "Effect of Pt film thickness on PtSi formation and film surface morphology," *Surf. Coatings Technol.* **198**, 329 (2005).
- [9] J. M. Mooney, "Infrared optical absorption of thin PtSi films between 1 and 6  $\mu\text{m}$ ," *J. Appl. Phys.* **64**, 4664 (1988).
- [10] J. M. Pimbley, "Infrared optical constants of PtSi," *Appl. Phys. Lett.* **42**, 984 (1983).
- [11] H. Koc, E. Deligöz, and A. M. Mamedov, "The elastic, electronic, and optical properties of PtSi and PtGe compounds," *Phil. Mag.* **91**, 3093 (2011).

- [12] M. C. Li, L. C. Zhao, D. G. Liu, and X. K. Chen, "Topographical, compositional, and Schottky characterization of PtSi/Si Schottky diodes," *Mater. Chem. Phys.* **80**, 620 (2003).
- [13] M. Kimata, M. Denda, N. Yutani, S. Iwade, and N. Tsubouchi, "A 512x512-element PtSi Schottky barrier infrared image sensor," *IEEE Journal of Solid-State Circuits* **22**, 1124 (1987).
- [14] J. Mooney, "PtSi internal photoemission; Theory and Experiment," *SPIE Infrared Sensors and Sensor Fusion* **782**, 99 (1987).
- [15] A. Rogalski, *Infrared Detectors*, 2nd ed., (CRC Press, Boca Raton, FL., 2011).
- [16] R. Fowler, "The analysis of photoelectric sensitivity curves for clean metals at various temperatures," *Phys. Rev.* **38**, 45 (1931).
- [17] J. Cohen, J. Vilms, and R. J. Archer, "Investigation of semiconductor Schottky barriers for optical detection and cathodic emission," Air Force Cambridge Res. Labs., Report No. 68-0651 (1969) and No. 69-0287 (1969).
- [18] P. B. Clapham and M. C. Hutley, "Reduction of lens reflection by the 'moth eye' principle," *Nature* **244**, 281 (1973).
- [19] F. Lora Gonzalez, L. Chan, A. Berry, D. E. Morse, and M. J. Gordon, "Simple colloidal lithography method to fabricate large-area moth-eye antireflective structures on Si, Ge, and GaAs for IR applications," *J. Vac. Sci. Technol. B* **32**, 051213 (2014).
- [20] S. Hüfner, G. Wertheim, and J. Wernick, "XPS core line asymmetries in metals," *Solid State Commun.* **17**, 417 (1975).
- [21] T. L. Barr, "An ESCA study of the termination of the passivation of elemental metals," *J. Phys. Chem.* **82**, 1801 (1978).

- [22] D. Briggs and P. Seah, *Practical Surface Analysis, Auger and X-ray Photoelectron Spectroscopy*, (Wiley, New York, 1990).
- [23] A. A. Naem, "Platinum silicide formation using rapid thermal processing," *J. Appl. Phys.* **64**, 4161 (1988).
- [24] G. Larrieu, E. Dubois, X. Wallart, X. Baie, and J. Katcki, "Formation of platinum-based silicide contacts; Kinetics, stoichiometry, and current drive capabilities," *J. Appl. Phys.* **94**, 7801 (2003).
- [25] F. Lora Gonzalez and M. J. Gordon, "Bio-inspired sub-wavelength surface structures for ultra-broadband, omni-directional anti-reflection in the mid and far IR," *Opt. Express* **22**, 12808 (2014).
- [26] C. Katsidis and D. Siapkias, "General transfer matrix method for optical multilayer systems with coherent, partially coherent, and incoherent interference," *Appl. Opt.* **41**, 3978 (2002).
- [27] H. K. Raut, V. A. Ganesh, A. S. Nair, S. Ramakrishna, "Anti-reflective coatings: A critical, in-depth review," *Energy Environ. Sci.* **4**, 3779 (2011).
- [28] S. Chattopadhyay, Y. F. Huang, Y. J. Jen, A. Ganguly, K. H. Chen, L. C. Chen, "Anti-reflective and photonic nanostructures," *Mater. Sci. Eng. R* **69**,1 (2010).
- [29] K. Han and C. H. Chang, "Numerical modeling of sub-wavelength anti-reflecting structures for solar module applications," *Nanomaterials* **4**, 87 (2014).
- [30] E. D. Palik, *Handbook of Optical Constants of Solids*, (Academic Press, Boston, 1997).
- [31] F. Lora Gonzalez, D. E. Morse, and M. J. Gordon, "Importance of diffuse scattering phenomena in moth-eye arrays for broadband infrared applications," *Opt. Lett.* **39**, 13 (2014).

## Chapter 8

---

### **Microplasma-based synthesis of hierarchical semiconducting metal oxides using Si moth-eye arrays**

---

*Adapted from the Applied Physics Letters article:*

K. Mackie, F. Lora Gonzalez, A. Pebley, and M.J. Gordon, *Applied Physics Letters*, in preparation (2015).

### *8.1. Chapter summary*

Microplasma spray deposition is combined with colloidal lithography and reactive ion etching to create hierarchically-structured metal oxide nanostructures (e.g., NiO, Fe<sub>2</sub>O<sub>3</sub>, and CuO) on silicon micro-pillar arrays. A diverse range of nanostructured materials and morphologies were achieved. The effect of microplasma operation, deposition conditions, and pillar geometry on film morphology and surface coverage is highlighted. The combined synthesis approach presented herein provides a general and tunable method to realize a variety of functional and hierarchical metal oxide materials.

### *8.2. Introduction*

The ability to control the morphology of nanoscale materials, as well as integrate them into functional hierarchical structures, are fundamental to the development of next-generation micro- and optoelectronic devices [1-4], sensors [5], and energy harvesting [6-9] and storage technologies [10-11]. Realization of these multi-material and multi-scale hierarchical systems often requires complicated processing steps which may involve a combination of wet chemistry, physical/chemical vapor deposition, direct growth (VLS, MBE), self- and directed assembly, lithography, and etching. In addition, both wet and dry conditions, high temperatures, vacuum processing, and templates or catalysts can be required. As such, we continually seek to develop general and tunable methods that can easily create structured, functional, and hierarchical systems in different and hybrid material platforms.

In this work, we present a general approach, which combines microplasma spray deposition, colloidal lithography and reactive ion etching (RIE), to create hierarchically

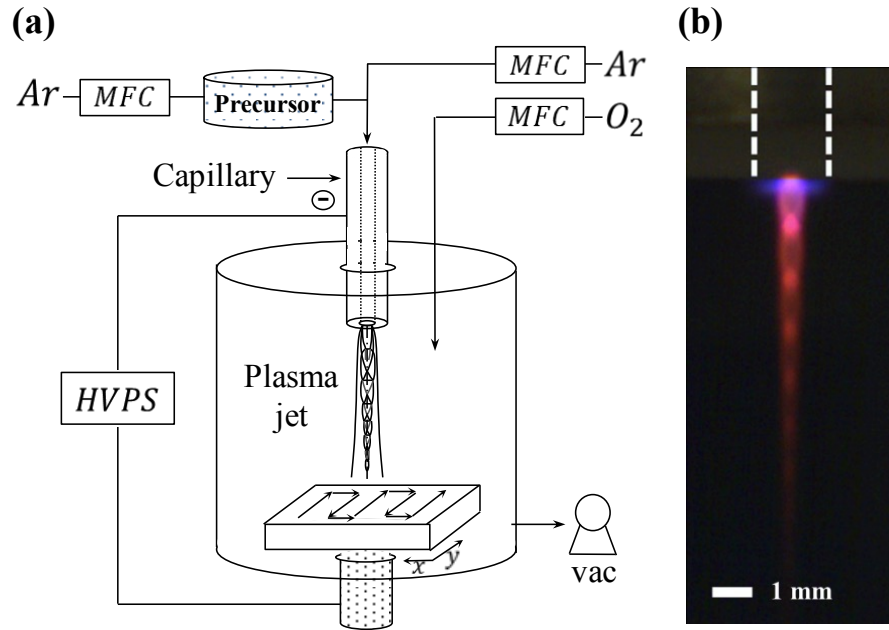
structured metal oxides (e.g., NiO, Fe<sub>2</sub>O<sub>3</sub>, and CuO) and hybrid structures on patterned substrates of any kind. The aforementioned oxides were chosen due to their promise as inexpensive materials for photocatalysis and water splitting applications [12-14], sensing devices [15-18], and energy storage technologies [19-23]. In the present case, a microplasma jet functions as a tunable and highly directed source of both reactive and unreactive species (e.g., atoms, ions, clusters, and/or nanoparticles) for direct growth of crystalline nanomaterials; a wide range of substrates can be accommodated with growth occurring at low temperatures under both reducing and oxidizing, high pressure conditions. Herein, we show a diverse range of materials and hierarchical structures that can be achieved using the combined colloidal-lithography and microplasma approach, as well as highlight how microplasma operation, deposition conditions, and substrate patterning affect metal oxide film morphology and surface coverage.

### *8.3. Experimental methods*

Metal oxide nanostructures were deposited on micro-patterned silicon substrates (discussed below) using the microplasma deposition system depicted in Fig. 1 (see [24-29] for details). A flow-stabilized, DC hollow cathode discharge was used to crack sublimed organometallic precursors into active growth species (e.g., atoms, ions, and clusters) which were directed towards a substrate under supersonic flow conditions [26, 27]. Nickelocene (Ni(Cp)<sub>2</sub>), ferrocene (Fe(Cp)<sub>2</sub>), and copper(II) hexafluoroacetylacetonate hydrate (Cu(hfac)<sub>2</sub>·H<sub>2</sub>O) were sublimed and fed with 100-300 sccm Ar to the plasma jet anode (stainless steel capillary tube, ID=500 μm) which was biased with current regulated negative high voltage (~10 mA, 300-800 V). O<sub>2</sub> (50–100 sccm) was introduced into the anode gas

feed or chamber background, the latter being maintained at 10-50 Torr. The substrate stage, ~1 cm downstream of the capillary exit, was raster scanned in a serpentine pattern during deposition at rates from 0.5-2.0 mm/s.

**Figure 1:** (a) Schematic of the microplasma deposition system. (b) Photo of the supersonic flow profile and shock diamonds for an Ar microplasma jet at 15 Torr. MFC = mass flow controller and HVPS = high voltage power supply. Need to modify this some.



Close-packed nano and micro-pillars were fabricated in Si (B-doped, 0-100  $\Omega\text{cm}$ ) using a two-step colloidal lithography method discussed elsewhere [30, 31]. Colloidal silica spheres ( $d=500$  nm) were synthesized using a Stober-like process [32], functionalized with allytrimethoxysilane (ATMS) in ethanolic medium (pH 5.5, acetic acid, 1% water by volume), washed in ethanol, and dried in a vacuum oven overnight (100°C). The colloids were then dispersed in (2:1) ethanol:chloroform at 0.25%v/v, supported on a water sub-

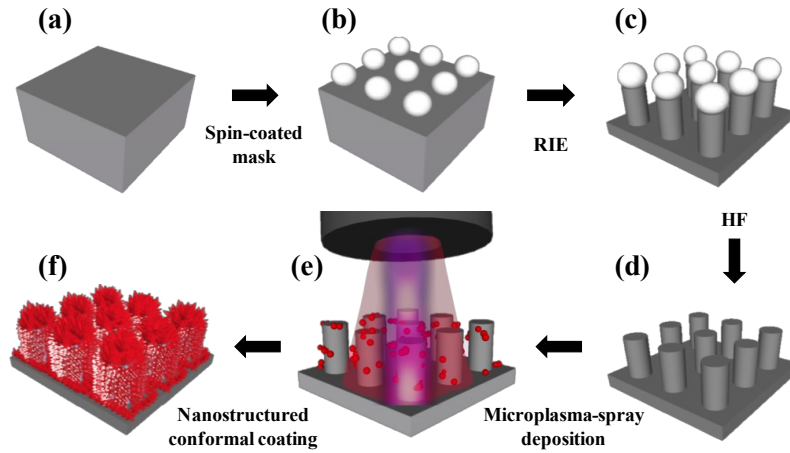
phase, and deposited on Si wafers using Langmuir-Blodgetty and dip-coating at a constant surface pressure of  $\sim 8$  mN/m and 1.5 mm/min withdrawal rate. Non-close-packed (random) pillars were formed by spin-coating dilute solutions of colloidal particles (0.1%v/v in ethanol) directly onto Si wafers at 3000 rpm for 1 minute. The colloid layer was then used directly as an etch mask.

Si substrates with SiO<sub>2</sub> colloidal masks were etched in a Plasma-Therm 770 SLR-RIE using 26:54:20 sccm SF<sub>6</sub>:C<sub>4</sub>F<sub>8</sub>:Ar at 19 mTorr with 825 W ICP power and 25 W chuck bias. Etch rates were 150-300 nm/min depending on the spacing of the colloids, i.e., due to the aspect ratio-dependent etching effect [33]. After etching, samples were cleaned in ethanol/acetone, and any remaining SiO<sub>2</sub> mask was removed in a 10% HF bath. Hybrid metal oxide-silicon microstructures were then synthesized by plasma spraying the respective film precursor under oxidizing conditions onto patterned Si substrates. The overall process schematic is shown in Fig. 2.

The crystallinity and phase of the deposited oxide coatings were analyzed via glancing-angle (1°) x-ray diffraction (GA-XRD) using Cu K $\alpha$  radiation on a Rigaku Smartlab. High resolution micrographs of the bare and metal oxide-coated silicon



**Figure 2:** Schematic of the process to produce hierarchical micro-arrays. (a) A colloidal mask is spin-coated or formed by Langmuir-Blodgetty; the mask pattern is then transferred to the substrate by RIE (c). (d) The mask is removed with HF. (e) Using the microplasma, (f) a nanostructured coating is formed on the arrays (f).



#### 8.4. Preliminary results

Figure 3 shows top down and side-view images of NiO, CuO, and Fe<sub>2</sub>O<sub>3</sub> grown on sparse arrays of Si micro-pillars ( $h = 2.5\mu\text{m}$ ). The three nanostructured oxides were deposited at 20 Torr. XRD data confirm the material phases to be NiO (bunsenite, rock salt,  $Fm\bar{3}m$ ), CuO (tenorite, monoclinic,  $C2/c$ ), and Fe<sub>2</sub>O<sub>3</sub> (hematite, rhombohedral,  $R\bar{3}c$ ). The growth of the nanostructured films is conformal in these sparse arrays due to large spacing between Si pillars. The tops of the pillars are favored in the growth, suggesting highly directed arrival of growth species and shadowing as the growth proceeds. The microplasma technique can be used to create conformal coatings on three-dimensional substrates using a diverse range of crystalline metal oxides at room temperature.

**Figure 3:** Plasma-spray deposited conformal coatings of (a) NiO, (b) CuO, and (c) Fe<sub>2</sub>O<sub>3</sub> on sparse Si micro-pillars with corresponding GA-XRD patterns. Scale bars are 1  $\mu$ m.

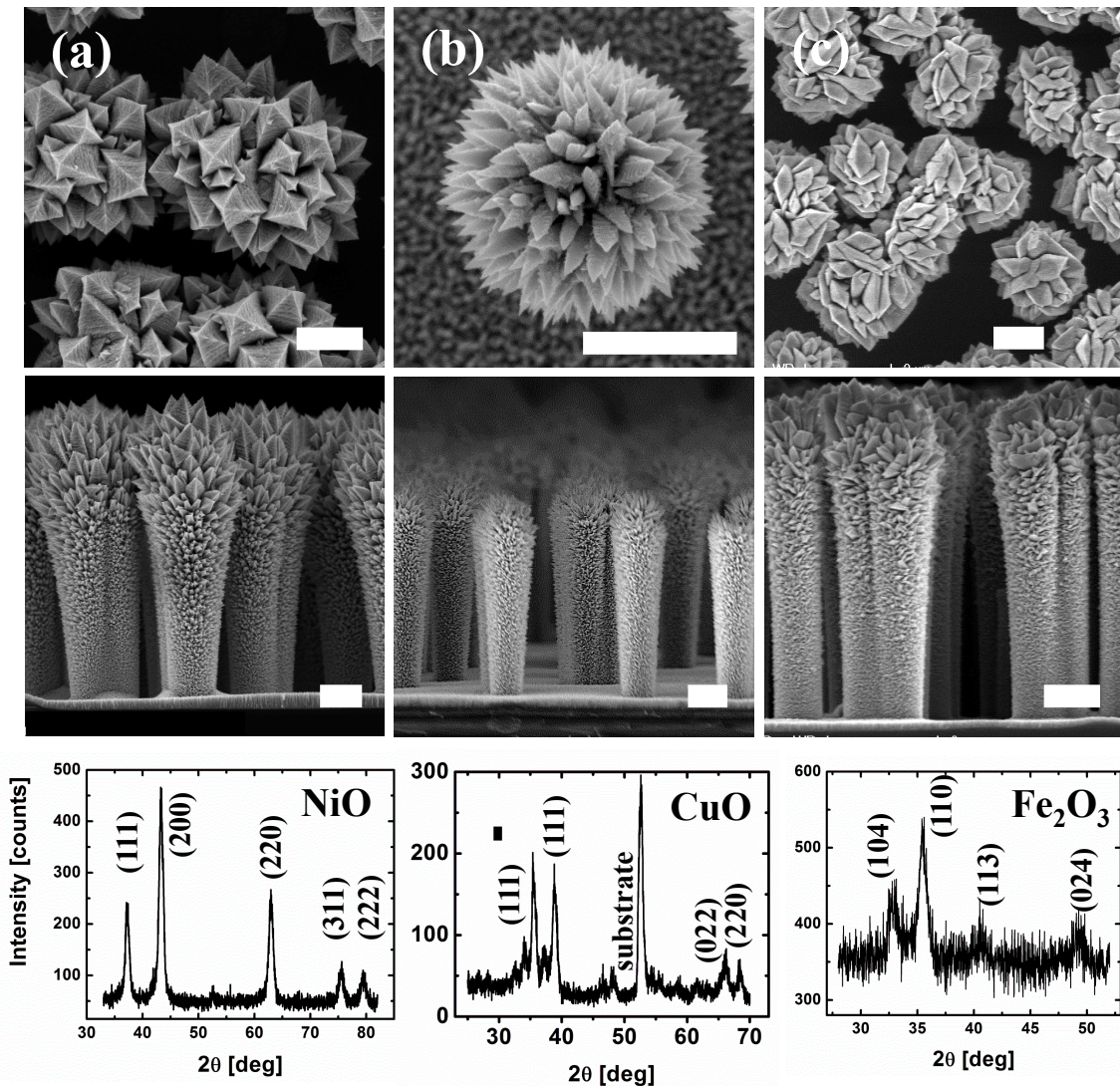
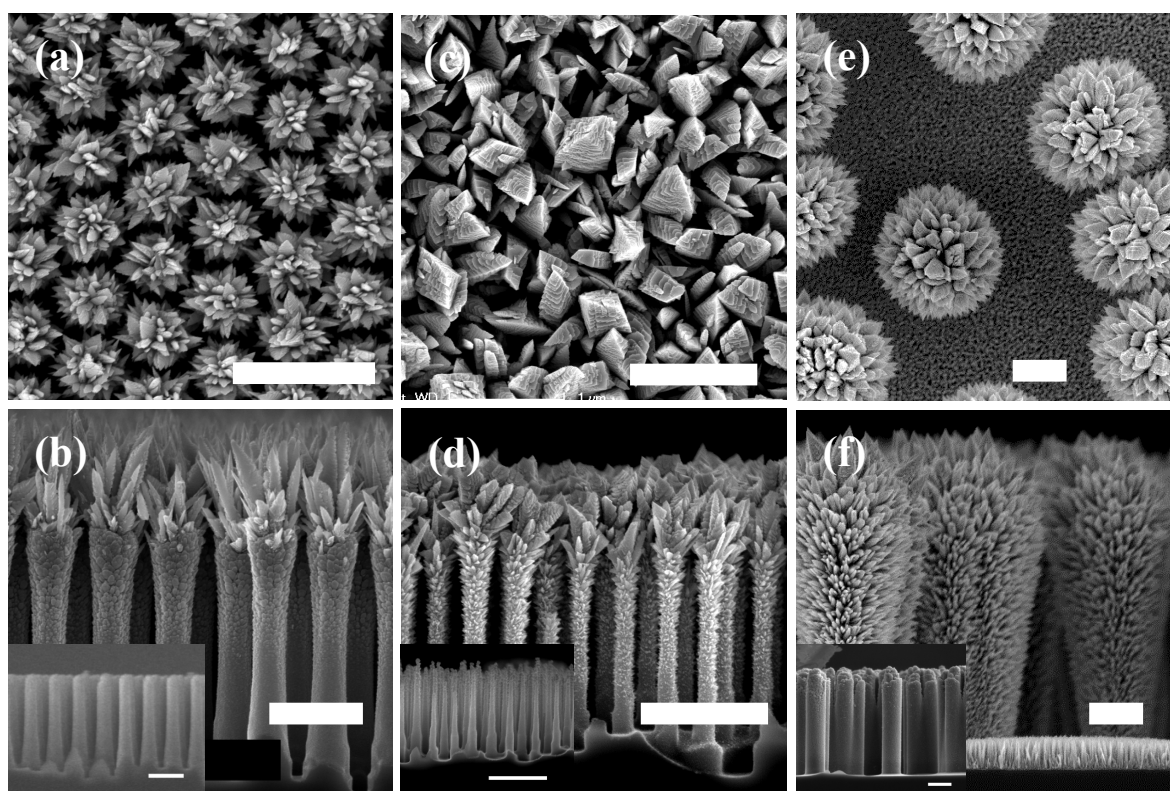


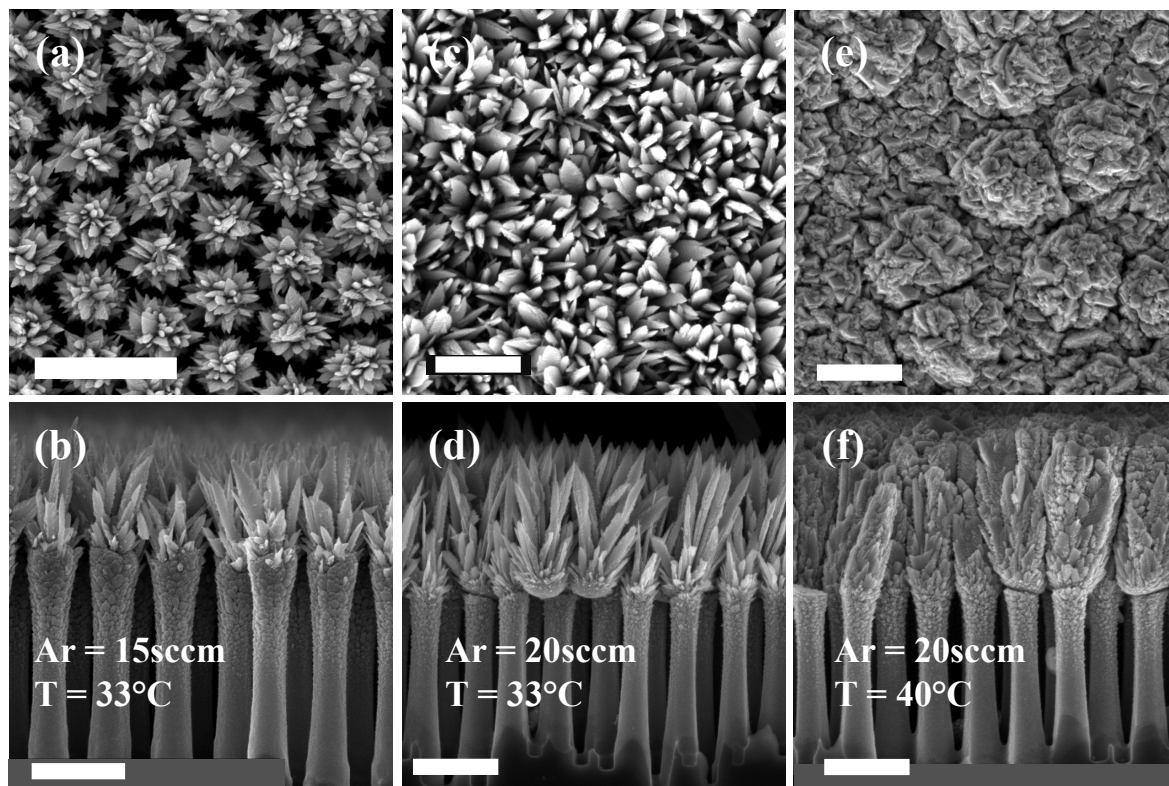
Figure 4 shows the effect of moth-eye on the growth of nanostructured films. Three CuO films were grown on Si frusta, needles, and a sparse array of pillars under identical plasma operating parameters. The structures grown on frusta are limited to the tops of the structures (Figs. 4 a,b), with increasing conformal coverage as spacing between the Si structures increases (Figs. 4 c-f). This is due to shadowing effects, because the microplasma provides a highly-directional flux of growth species. Controlling the packing density and

shape of the Si pillars gives (indirect) control of the metal oxide coverage, which can be useful in designing devices where asymmetrical architectures are desired (e.g., multiple light absorbers for optimal solar absorption) [7]. Figure 5 shows the effect of precursor flux on the film morphology. Three CuO films were grown on close-packed frusta: Under increasing Cu precursor flux, the nanostructure morphology changes along with thickening of the films. Specifically, the films become denser with higher flux, because the arrival rate of growth species is higher.

**Figure 4:** CuO grown on (a-b) close-packed frusta array, (c-d) close-packed array of needles, and (e-f) sparse micro-pillars. Insets show the Si structures prior to deposition of the CuO. Scale bars are 1  $\mu\text{m}$ .



**Figure 5:** CuO grown on close-packed frusta array with increasing precursor flux: (a-b) low, (c-d) medium, and (e-f) high. The argon flow through the sublimation cell and cell temperature were used to control the flux. Scale bars 1  $\mu\text{m}$ .



### 8.5 Future work

We have demonstrated the use of microplasma spray deposition combined with colloidal lithography and reactive ion etching to create hierarchically-structured metal oxide nanostructures on silicon micro-pillar arrays. A diverse range of nanostructured materials and morphologies were achieved. This method can be used to realize a variety of functional and hierarchical metal oxide materials, which could be used in applications such as battery electrodes, capacitors, gas sensors, and photoelectrochemical cells. Experiments will be

designed to understand the electronic and chemical characteristics of these structures; for example, electrochemical cyclic voltammetry measurements. In addition, simple PEC cells, capacitors or gas sensors will be designed, built, and tested to demonstrate potential uses of this growth technique.

## 8.6 References

- [1] D. Whang, S. Jin, Y. Wu, C. M. Lieber, "Large-scale hierarchical organization of nanowire arrays for integrated nanosystems," *Nano Letters* **3**, 1255 (2003).
- [2] H. J. Xu, L. Su, Y. F. Chan, and X. M. Sun, "Structural and multiband photoluminescent properties of a hierarchical ZnO/Si nanoheterostructure," *J. Mater. Res.* **26**, 1174 (2011).
- [3] S. Ke, Y. Jing, N. Park, C. Li, Y. Bando, and D. Wang, "Solution synthesis of large-scale, high-sensitivity ZnO/Si hierarchical nanoheterostructure photodetectors," *J. Am. Chem. Soc.* **132**, 15464 (2010).
- [4] C. Cheng, B. Liu, H. Yang, W. Zhou, L. Sun, R. Chen, S. F. Yu, J. Zhang, H. Gong, H. Sun, and H. J. Fan "Hierarchical assembly of ZnO nanostructures on SnO<sub>2</sub> backbone nanowires: Low-temperature hydrothermal preparation and optical properties," *ACS Nano* **3**, 3069 (2009).
- [5] J. H. Lee, "Gas sensors using hierarchical and hollow oxide nanostructures: Overview," *Sensors and Actuators B* **140**, 319 (2009).
- [6] J. Shi, Y. Hara, C. Sun, M. A. Anderson, and X. Wang, "Three-dimensional high-density hierarchical nanowire architecture for high-performance photoelectrochemical electrodes," *Nano Lett.* **11**, 3413 (2011).
- [7] C. Liu, J. Tang, H. M. Chen, B. Liu, and P. Yang, "A fully integrated nanosystem of semiconductor nanowires for direct solar water splitting," *Nano Lett.* **13**, 2989 (2013).
- [8] K. Sun, Y. Jing, C. Li, X. Zhang, R. Aguinaldo, A. Kargar, K. Madsen, K. Banu, Y. Zhou, Y. Bando, Z. Liu, and D. Wang, "3D branched nanowire heterojunction

- photoelectrodes for high-efficiency solar water splitting and H<sub>2</sub> generation," *Nanoscale* **4**, 1515 (2012).
- [9] Z. Han, L. Wei, Z. Zhang, X. Zhang, H. Pan, and J. Chen, "Visible-light photocatalytic application of hierarchical Au-ZnO flower-rod heterostructures via surface plasmon resonance," *Plasmonics* **8**, 1193 (2013).
- [10] J. Jiang, Y. Li, J. Liu, X. Huang, C. Yuan, and X. W. Lou, "Recent Advances in Metal Oxide-based Electrode Architecture Design for Electrochemical Energy Storage," *Adv. Mater.* **24**, 5166 (2012).
- [11] B. Liu, J. Zhang, X. Wang, G. Chen, D. Chen, C. Zhou, and G. Shen, "Hierarchical three-dimensional ZnCo<sub>2</sub>O<sub>4</sub> nanowire arrays/carbon cloth anodes for a novel class of high-performance flexible lithium-ion batteries," *Nano Lett.* **12**, 3005 (2012).
- [12] Z. Jin, X. Zhang, Y. Li, S. Li, and G. Lu, "5.1% Apparent quantum efficiency for stable hydrogen generation over eosin-sensitized CuO/TiO<sub>2</sub> photocatalyst under visible light irradiation," *Catalysis Comm.* **8**, 1267 (2007).
- [13] K. Sivula, F. Le Formal, and M. Grätzel, "Solar water splitting: Progress using hematite ( $\alpha$ -Fe<sub>2</sub>O<sub>3</sub>) photoelectrodes," *ChemSusChem* **4**, 432 (2011).
- [14] Kay, I. Cesar, and M. Grätzel, "New benchmark for water photooxidation by nanostructured  $\alpha$ -Fe<sub>2</sub>O<sub>3</sub> films." *J. Am. Chem. Soc.* **128**, 15714 (2006).
- [15] N. Yamazoe, G. Sakai, and K. Shimano, "Oxide semiconductor gas sensors," *Catalysis Surveys from Asia* **7**, 63 (2003).
- [16] J. Chen, K. Wang, L. Hartman, and W. Zhou, "H<sub>2</sub>S detection by vertically aligned CuO nanowire array sensors," *J. Phys. Chem. C* **112**, 16017 (2008).

- [17] J. A. Dirksen, K. Duval, and T. A. Ring, "NiO thin-film formaldehyde gas sensor," *Sensors and Actuators B* **80**, 106 (2001).
- [18] D. H. Kim, Y. S. Shim, J. M. Jeon, H. Y. Jeong, S. S. Park, Y. W. Kim, J. S. Kim, J. H. Lee, and H. W. Jang, "Vertically ordered hematite nanotube array as an ultrasensitive and rapid response acetone sensor," *ACS Appl. Mater. Interfaces* **6**, 14779 (2014).
- [19] J. Chen, L. Wu, W. Li, and X. Gou, " $\alpha$ -Fe<sub>2</sub>O<sub>3</sub> nanotubes in gas sensor and lithium-ion battery applications." *Adv. Mater.* **17**, 582 (2005).
- [20] B. Varghese, M. V. Reddy, Z. Yanwu, C. S. Lit, T. C. Hoong, G. V. Subba Rao, B. V. R. Chowdari, A. T. Shen Wee, C. T. Lim, and C. H. Sow, "Fabrication of NiO nanowall electrodes for high performance lithium ion battery," *Chem. Mater.* **20**, 3360 (2008).
- [21] C. Yuan, X. Zhang, L. Su, B. Gao, and L. Shen, "Facile synthesis and self-assembly of hierarchical porous NiO nano/micro spherical superstructures for high performance supercapacitors," *J. Mater. Chem.* **19**, 5772 (2009).
- [22] C. Wu, P. Yin, X. Zhu, C. OuYang, and Y. Xie, "Synthesis of hematite ( $\alpha$ -Fe<sub>2</sub>O<sub>3</sub>) nanorods: diameter-size and shape effects on their applications in magnetism, lithium ion battery, and gas sensors." *J. Phys. Chem. B* **110**, 17806 (2006).
- [23] S. Gao, S. Yang, J. Shu, S. Zhang, Z. Li, and K. Jiang, "Green fabrication of hierarchical CuO hollow micro/nanostructures and enhanced performance as electrode materials for lithium-ion batteries." *J. Phys. Chem. C* **112**, 19324 (2008).
- [24] Pebley, A. Peek, T. M. Pollock, and M. J. Gordon, "Microplasma-based growth of biphasic NiFe<sub>2</sub>O<sub>4</sub>/NiO nanogranular films for exchange bias applications," *Chem. Mater.* **26**, 6026 (2014).



- [25] T. Koh, E. O'Hara, and M. J. Gordon, "Growth of nanostructured CuO thin films via microplasma-assisted, reactive chemical vapor deposition at high pressures," *J. Crystal Growth* **363**, 69 (2013).
- [26] T. Koh and M. J. Gordon. "Spray deposition of nanostructured metal films using hydrodynamically stabilized, high pressure microplasmas," *J. Vac. Sci. Technol. A* **31**, 061312 (2013).
- [27] T. Koh, I. Chiles, and M. J. Gordon. "Slit-based supersonic microplasma jets: Scalable sources for nanostructured thin film deposition," *Appl. Phys. Lett.* **103**, 163115 (2013).
- [28] T. Koh, E. O'Hara, and M. J. Gordon, "Microplasma-based synthesis of vertically aligned metal oxide nanostructures," *Nanotechnol.* **23**, 425603 (2012).
- [29] D. Mariotti, R. M. Sankaran, "Microplasmas for nanomaterials synthesis," *J. Phys. D* **43**, 323001 (2010).
- [30] F. Lora Gonzalez, L. Chan, A. Berry, D. E. Morse, and M. J. Gordon, "A simple colloidal lithography method to fabricate large-area moth-eye anti-reflective structures on Si, Ge, and GaAs for IR applications," *J. Vac. Sci. Technol. B* **32**, 051213 (2014).
- [31] F. Lora Gonzalez and M. J. Gordon, "Bio-inspired, sub-wavelength surface structures for ultra-broadband, omni-directional anti-reflection in the mid and far IR," *Opt. Express* **22**, 12808 (2014).
- [32] W. Stöber, A. Fink, and E. Bohn, "Controlled growth of monodisperse silica spheres in the micron size range," *J. Colloid Interface Sci.* **26**, 62 (1968).
- [33] D. Vrtacnik, D. Resnik, U. Aljancic, M. Mozek, and S. Amon, "Silicon dry etching profile control by RIE at room temperature for MEMS applications," *Proc. of SPIE* **6037**, 603720 (2005).